

**STATISTICAL MECHANICAL AND QUANTUM  
MECHANICAL MODELING OF CONDENSED  
PHASE SYSTEMS**

by

**Matthew R. LaBrosse**

Bachelor of Chemical Engineering,

University of Minnesota, 2004

Submitted to the Graduate Faculty of  
the Swanson School of Engineering in partial fulfillment  
of the requirements for the degree of

**Doctor of Philosophy**

University of Pittsburgh

2009

UNIVERSITY OF PITTSBURGH  
SWANSON SCHOOL OF ENGINEERING

This dissertation was presented

by

Matthew R. LaBrosse

It was defended on

19 November 2009

and approved by

J. Karl Johnson, PhD, W.K. Whiteford Professor, Department of Chemical and Petroleum  
Engineering

Joseph J. McCarthy, PhD, Associate Professor and W.K. Whiteford Faculty Fellow,  
Department of Chemical and Petroleum Engineering

Dan C. Sorescu, PhD, Physical Scientist, National Energy Technology Laboratory, and  
Adjunct Professor, Department of Chemical and Petroleum Engineering

Anthony J. DeArdo, PhD, W.K. Whiteford Professor, Department of Mechanical  
Engineering and Materials Science

Dissertation Director: J. Karl Johnson, PhD, W.K. Whiteford Professor, Department of  
Chemical and Petroleum Engineering

# STATISTICAL MECHANICAL AND QUANTUM MECHANICAL MODELING OF CONDENSED PHASE SYSTEMS

Matthew R. LaBrosse, PhD

University of Pittsburgh, 2009

Understanding adsorption in nanoporous media is vital to improving their use in industrial applications such as fluid storage and separations processes. One major objective of this research is to shed light on an on-going controversy in literature over where gases adsorb on single walled carbon nanotube bundles. Grand-canonical Monte Carlo simulations have been performed using models of carbon nanotube bundles composed of tubes of all the same diameter (homogeneous) and tubes of different diameters (heterogeneous). We used three metrics with which we compared our simulation results to those found in experiments on carbon nanotubes: the specific surface area, the isosteric heat of adsorption, and the adsorption capacity. Simulations of classically behaved fluids Ar, CH<sub>4</sub>, and Xe indicate that nanotubes prepared by the HiPco process are best described by a heterogeneous bundle model with  $\sim 11\%$  of the nanotubes opened. Ne gas requires additional considerations to describe the quantum effects at the temperatures of interest, which have been implemented by the Feynman-Hibbs approximation. Overall, calculated results from Ne simulations are consistent with those from classical fluids. However, Ne simulations strongly indicate that the small interstitial channels formed by exactly three nanotubes are closed. Combined with previous studies on classically behaved fluids Ar, CH<sub>4</sub>, and Xe, experimental data including Ne are best matched by heterogeneous bundles with  $\sim 11\%$  open-ended nanotubes.

The development of a heterogeneous Co/C/O reactive force field (ReaxFF) potential has also been a major objective of this research. ReaxFF provides a method to describe bond-breaking and bond-forming events that can be applied to large-scale molecular dynamics

(MD) simulations. This many-bodied semi-empirical potential has been trained from *ab initio* density functional theory (DFT) calculations. The training set originally included descriptions of bulk and surface condensed phase cobalt systems. This was later expanded to include binary (Co/C, Co/O) and tertiary (Co/C/O) heterogeneous interactions. We have tested these parameters against additional DFT calculations not included in the training set. The parameter optimization has produced a force field capable of describing additional configurations with the same accuracy as those used in the fitting procedure. The optimized parameters have been used to predict the melting point and diffusion coefficients of condensed phase cobalt. Large-scale simulations of a Co<sub>2</sub>C phase nanoparticle show segregation on short time scales (less than 300 ps), with all C atoms forming chains and small graphene structures on the surface of a solid Co nanoparticle core. ReaxFF has also been used to show that diffusion of Co is more energetically favorable than oxygen through the interstitial sites of a cobalt oxide crystal. This is consistent with experimental observations that oxidized cobalt nanoparticle form hollow cobalt oxide nanospheres due to a faster Co diffusion rate through the oxide layer. These two binary applications demonstrate that ReaxFF is transferable to heterogeneous systems and is a computationally inexpensive means by which transition metal surface reactions can be explored.

## TABLE OF CONTENTS

<b>PREFACE</b> . . . . .	xii
<b>1.0 INTRODUCTION</b> . . . . .	1
1.1 Carbon nanotube bundles . . . . .	2
1.2 Transition metals . . . . .	2
<b>2.0 CLASSICAL FLUID ADSORPTION ON SINGLE WALLED CARBON NANOTUBE BUNDLES</b> . . . . .	4
2.1 Introduction . . . . .	4
2.2 Method and theory . . . . .	7
2.2.1 Construction of bundles . . . . .	7
2.2.2 Adsorbate-bundle interactions . . . . .	11
2.2.3 Simulations . . . . .	11
2.3 Results . . . . .	13
2.3.1 Bundle production . . . . .	13
2.3.2 Adsorption results on closed bundles . . . . .	16
2.3.3 Adsorption results on opened and partially opened bundles . . . . .	25
2.3.4 Specific surface area . . . . .	30
2.4 Conclusion . . . . .	34
<b>3.0 ADSORPTION OF NEON IN SINGLE WALLED CARBON NANOTUBE BUNDLES</b> . . . . .	37
3.1 Introduction . . . . .	37
3.2 Methodology . . . . .	38
3.2.1 Bundle construction . . . . .	38

3.2.2	Interaction potentials for classical fluids . . . . .	39
3.2.3	Interaction potentials for quantum fluids . . . . .	40
3.2.3.1	Path-integral formalism . . . . .	40
3.2.3.2	Feynman-Hibbs method . . . . .	41
3.2.4	Specific surface area . . . . .	42
3.2.5	Simulation details . . . . .	43
3.3	Results and Discussion . . . . .	43
3.3.1	Bundle production . . . . .	43
3.3.2	Comparison of quantum methods . . . . .	44
3.3.3	Solid-fluid interactions . . . . .	44
3.3.4	Adsorption on graphite . . . . .	47
3.3.5	Defect interstitial adsorption . . . . .	49
3.3.6	Ideal interstitial adsorption . . . . .	53
3.3.7	Effect of Ne-graphene binding . . . . .	58
3.4	Conclusion . . . . .	59
<b>4.0</b>	<b>TUNGSTEN AND VACANCY DIFFUSION IN FCC COBALT . . . . .</b>	<b>61</b>
4.1	Introduction . . . . .	61
4.2	Computational methods . . . . .	62
4.3	Results . . . . .	64
4.4	Conclusion . . . . .	74
<b>5.0</b>	<b>REACTIVE FORCE FIELD DEVELOPMENT FOR COBALT . . . . .</b>	<b>76</b>
5.1	Introduction . . . . .	76
5.2	Methodology . . . . .	77
5.2.1	QM calculations . . . . .	77
5.2.2	ReaxFF . . . . .	77
5.3	Results and discussion . . . . .	78
5.3.1	QM training of force field . . . . .	78
5.3.2	Parameterization and validation of ReaxFF . . . . .	81
5.3.3	Thermophysical property predictions from ReaxFF . . . . .	82
5.4	Conclusion . . . . .	85

<b>6.0</b>	<b>REACTIVE FORCE FIELD FOR HETEROGENEOUS SYSTEMS</b>	97
6.1	Introduction	97
6.2	Methodology	98
6.2.1	QM Calculations	98
6.2.2	ReaxFF	99
6.3	Results	99
6.3.1	Force field parameterization	99
6.3.2	Validation of force field	101
6.3.3	Limitations of Co/C/O description	102
6.3.4	Cobalt-carbide segregation in nanoparticles	104
6.3.5	Oxidation of nanoclusters	104
6.4	Conclusion	106
<b>7.0</b>	<b>FUTURE WORK</b>	120
7.1	Grain boundaries and twinning	120
7.2	Surface reconstruction	122
7.3	CO dissociation on Co nanoparticles	122
	<b>BIBLIOGRAPHY</b>	124

## LIST OF TABLES

2.1	Specific surface areas for classical fluids . . . . .	12
3.1	Potential parameters used in simulations . . . . .	46
3.2	Specific surfaces areas for classical fluids and Ne . . . . .	52
3.3	Specific surface areas on nanotubes with blocked ideal interstitials . . . . .	53
4.1	Least squares results for internal surface area determination . . . . .	66
4.2	Surface intrinsic error corrections to vacancy formation energies . . . . .	67
5.1	Comparison of bulk Co properties from DFT and experiments . . . . .	87
5.2	Elastic moduli of Co phases from DFT . . . . .	88
5.3	ReaxFF fit to elastic moduli . . . . .	90
5.4	ReaxFF fit to surface formation energies . . . . .	91
5.5	Comparison of ReaxFF predictions to DFT surface formation energies . . . . .	92
5.6	Comparison of ReaxFF to DFT vacancy formation energies . . . . .	93
5.7	Predicted melting points from temperature hysteresis . . . . .	94
5.8	Diffusion coefficients of liquid Co . . . . .	95
5.9	Solid Co diffusion coefficients from ReaxFF . . . . .	96
6.1	Adatom and adlayer adsorption energies . . . . .	107
6.2	CO adsorption energies . . . . .	108
6.3	C and O surface substitutions . . . . .	109
6.4	C substitutions in fcc and bcc cobalt . . . . .	110
6.5	Predicted ReaxFF energies for C systems . . . . .	111
6.6	Predicted ReaxFF energies for O systems . . . . .	112
6.7	Predicted C and O adsorption energies on substituted surfaces . . . . .	113

6.8	Predicted ReaxFF energies for CO systems . . . . .	114
6.9	Limitations of heterogeneous ReaxFF potential . . . . .	115
6.10	Overall performance of optimized ReaxFF parameters . . . . .	116
6.11	Diffusion energy barriers in bulk CoO . . . . .	119

## LIST OF FIGURES

2.1	Comparison of isosteric heats from different experiments . . . . .	5
2.2	Potential energy curves for nanotube-nanotube interactions . . . . .	9
2.3	Heterogeneous nanotube bundles . . . . .	15
2.4	Methane adsorption on closed nanotube bundles . . . . .	17
2.5	Xe adsorption on closed nanotube bundles . . . . .	19
2.6	Temperature effects on methane isosteric heats . . . . .	20
2.7	Isosteric heat for Xe on closed nanotube bundles . . . . .	22
2.8	Isosteric heats for methane on closed nanotube bundles . . . . .	24
2.9	Effect of heterogeneity on methane isosteric heats . . . . .	26
2.10	Effect of heterogeneity on methane adsorption . . . . .	27
2.11	Xe isosteric heat as a function of nanotube radius . . . . .	28
2.12	Isosteric heats for Xe on partially opened nanotube bundles . . . . .	29
2.13	Example adsorption isotherm to demonstrate the point-B method . . . . .	31
3.1	Quantum correction methods to Ne isotherms . . . . .	45
3.2	Adsorption of Ne on graphite using Bruch et al. parameters . . . . .	47
3.3	Two-dimensional $g(r)$ plots . . . . .	49
3.4	Isosteric heats for Ne on partially opened nanotubes . . . . .	51
3.5	Ne isosteric heats on nanotubes with blocked interstitials . . . . .	55
3.6	Ne adsorption isotherms . . . . .	57
3.7	Solid-fluid potential curves for fluid adsorbates . . . . .	58
4.1	Vacancy formation energies for 1 to 6 vacancies . . . . .	68
4.2	Energy pathways for di-vacancy diffusion in fcc Co . . . . .	70

4.3	Diagrams of a triangle and quadrangle diffusion mechanism in fcc Co . . . . .	72
4.4	Energy barriers for two diffusion mechanisms . . . . .	75
5.1	Murnaghan equations of state from DFT . . . . .	88
5.2	Co clusters used in force field development . . . . .	89
5.3	ReaxFF fit to equations of state . . . . .	90
5.4	Comparison of ReaxFF to DFT clusters energies . . . . .	93
5.5	Temperature hysteresis loop . . . . .	94
5.6	Arrhenius plot for liquid Co . . . . .	95
5.7	Correlating solid diffusion coefficients to defect concentration . . . . .	96
6.1	Equations of state for binary Co systems . . . . .	110
6.2	Cobalt-carbide phase segregation in a nanoparticle . . . . .	117
6.3	Vacancy coalescence in bulk fcc Co . . . . .	118
6.4	Oxidized Co nanoparticle . . . . .	119
7.1	Interfacial twinning of fcc Co grains . . . . .	121
7.2	Chiral surface reconstruction . . . . .	122

## **PREFACE**

I would like to thank my research advisor, Dr. J. Karl Johnson, for his guidance, insight, and motivation. He has truly led by example throughout my career as a graduate student. I am grateful to my committee members, Dr. Joseph McCarthy, Dr. Dan Sorescu, and Dr. Anthony DeArdo, for setting aside time in their schedules to participate in my thesis defense. I would also like to thank the National Energy and Technology Laboratory for supporting my career as graduate student.

## 1.0 INTRODUCTION

Molecular modeling is a useful and versatile tool in the field of materials research. Modeling methods are used to describe physical properties of materials and guide experimental studies. In particular, nanoporous materials and condensed phase metals can be tailored to meet desired properties based on insight gained through modeling.

Computational methods are typically rooted in the fundamentals of two broad classes: statistical mechanics and quantum mechanics. The underlying goal of statistical mechanical simulations is to determine measurable macroscopic properties from nanoscale configurations, related through the partition function of the system. The physical interactions between atoms are typically based on approximations to empirical observations. As such, this class of computational methods is only as accurate as the potential on which they are based. However, the overall simplicity of empirical potentials allows for simulations of thousands of atoms, an infeasible task using quantum mechanical methods.

Atomic interactions in quantum mechanical methods are generally more accurate than empirical potentials because they are fundamentally based on approximate solutions to the Schrödinger equation. One such method is density functional theory, which states that a many-bodied system of atoms can be approximated by functionals of its electron density at any position. Because density functional theory is based on first-principles, there is often good agreement with experimental results. This makes density functional theory an attractive choice for describing the energetics of a system. However, these methods are computationally expensive and scale poorly with increasing the system size. System sizes in density functional theory calculations are typically limited to hundreds of atoms. As such, it is clear to see the competing factors in the two classes of modeling: computational performance versus correct description of physics.

## 1.1 CARBON NANOTUBE BUNDLES

Carbon nanotubes are nanostructures made of graphite cylinders with diameters on the order of 10-12 Å. Nanotubes typically pack together in bundles forming two-dimensional hexagonal arrays. Modeling of nanoporous materials such as carbon nanotubes is critical to gaining a mechanistic understanding of adsorption related processes. Today, nanoporous media are used in a multitude of applications, including separations and gas sequestration. In the natural gas industry, CH<sub>4</sub> reserves can contain incredible amounts of CO<sub>2</sub> and H<sub>2</sub>S. Separations are used to remove these impurities from the product stream. In addition to natural gas, recent increase in demand of carbon-free technologies have sparked interest in hydrogen-based fuels. Hydrogen producing reactions, such as the water-gas shift and steam-reforming reactions, employ nanoporous membranes to extract the hydrogen from the product gas stream.[1, 2] Models can be used to identify materials with high selectivity to hydrogen.

Beyond separations, there are numerous applications for carbon nanotubes in gas storage. Nanoporous sorbents can be designed to separate and adsorb a specific gas species (e.g. hydrogen) in a stream of gas for energy storage. Nanoporous storage media have also been looked to for CO<sub>2</sub> sequestration (carbon capture), a pure by-product in petroleum refining.[3] In addition to selectivity, modeling is used to identify sorbents with high storage capacity for a desired gas species.

## 1.2 TRANSITION METALS

Calculations of condensed phase transition metals can be used to explore the science in a variety of real-world applications. *Ab initio* methods are used to describe the ground state geometries and diffusion energy barriers. Large-scale simulations are important for tuning material properties based on structure and composition at the atomic level. For example, large-scale molecular dynamics can be used to investigate the progression of grain boundary twinning and recrystallization. The ability to tailor physical and mechanical properties

allows for improvements in many industrial settings. This includes stronger drilling equipment, better high temperature alloys for steam turbines, metal coatings with higher thermal barriers, and corrosion resistant materials for fuel cells.

In addition to bulk applications, molecular modeling is used to explore surface chemistry of heterogeneous condensed phase transition metals, critical in understanding catalysis. Rational design of catalysts requires detailed knowledge of reactions on simple and complex surfaces. Simulations of catalytic material surface reconstruction provides useful information to experimentalists studying surface chemistry. Large-scale molecular simulations can also aid the development of catalytic materials by identifying surfaces with high surface activities that may have an increased resistance to surface poisoning (e.g. sulfur chemisorption). This is particularly attractive in Fisher-Tropsch synthesis and other coal to liquid technologies.

The work in this dissertation is divided into three parts employing both empirical potentials and density functional theory. The first part involves a look at fluid adsorption in carbon nanotube bundles using grand-canonical Monte Carlo simulations. The main objective is to gain a mechanistic understanding of how fluids adsorb in these structures. The second part involves density functional theory calculations exploring various diffusion mechanisms in condensed phase cobalt. The final part shows the use of density functional theory to develop a semi-empirical reactive force field for describing condensed phase cobalt and heterogeneous Co/C/O systems.

## 2.0 CLASSICAL FLUID ADSORPTION ON SINGLE WALLED CARBON NANOTUBE BUNDLES

The content of this chapter is taken from M. R. LaBrosse, W. Shi, and J. K. Johnson, “Adsorption of Gases in Carbon Nanotubes: Are Defect Interstitial Sites Important?”, *Langmuir*, **24**, 9430-9439 (2008).

### 2.1 INTRODUCTION

Gas adsorption on single walled carbon nanotubes (SWNTs) has been the focus of many experimental[4, 5, 6, 7, 8, 9, 10, 11, 12, 13, 14, 15, 16, 17, 18, 19, 20, 21, 22, 23, 24, 25, 26, 27, 28, 29, 30, 31, 32, 33, 34, 35] and theoretical studies.[31, 36, 37, 38, 39, 40, 41, 42, 43, 44, 45, 46, 47, 48] Experimentally produced SWNTs are known to form bundles containing 10s to 100s of individual tubes.[49, 50, 51, 52, 53] The bundles contain tubes with a distribution of diameters, depending on the methods used to produce the SWNTs. The tubes are observed to pack into hexagonal lattices when they form bundles, with gaps between the tubes of about 3.2 Å,[54] slightly smaller than the gap between layers of graphite.

There are many different ways to produce nanotube bundles, e.g., electric arc, laser ablation, and HiPco.[55, 56] It has been shown that nanotubes grown by the electric arc method tend to have capped ends,[57] while as-produced HiPco nanotubes have been shown to have a percentage of open nanotubes present.[58, 59, 48, 60, 61] It is therefore reasonable to expect that nanotubes produced by different methods might exhibit different sorption properties. An example of this may be seen from the experimentally measured low coverage isosteric heats of adsorption ( $q_{st}$ ) for Xe on nanotube bundles prepared from the arc and

the HiPco methods, as plotted in Figure 2.1. We see from the data in Figure 2.1 that  $q_{st}$  for Xe on the nanotubes produced by the electric arc method have considerably higher values than those for Xe on the HiPco nanotubes. In contrast,  $q_{st}$  values for Ar on electric arc nanotubes measured from different groups[20, 24] are in good agreement. Hence, it appears that variations in sorption properties measured on nanotubes prepared by the same method (e.g., electric arc) are small compared with variations in those properties prepared by different methods. This implies that when comparing simulations and experiments, different atomic-scale models may be needed to accurately describe nanotube bundles that come from electric arc and HiPco processes.

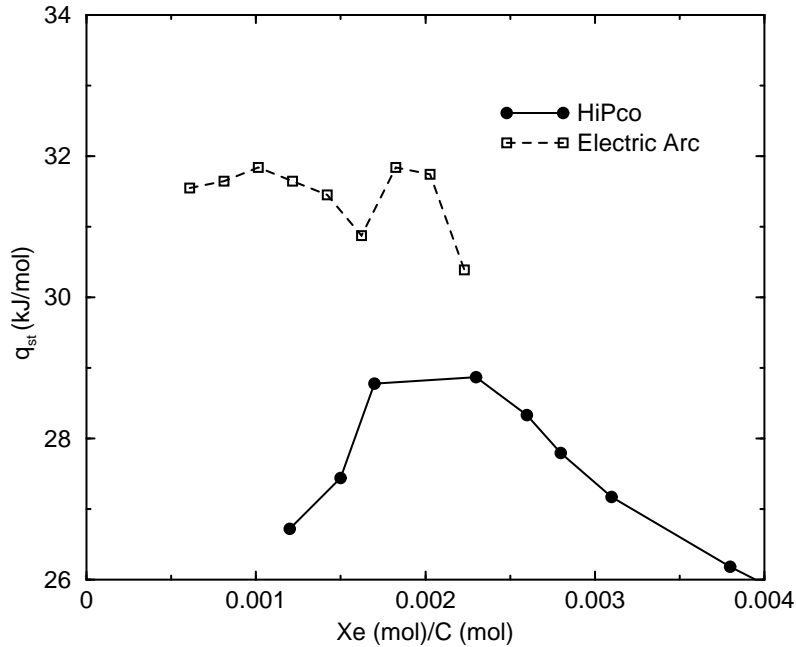


Figure 2.1: Experimental isosteric heat results for Xe adsorbed on nanotubes prepared using the arc method[22] and those prepared using the HiPco method.[62]

Controversy over where gases adsorb on single walled carbon nanotube bundles has been fueled by various experimental and molecular simulation studies.[17, 45, 35, 48, 46, 63, 12, 21] There is broad agreement that gases may adsorb in internal sites, groove sites, and external surface sites.[64, 65, 41, 66, 21, 34] These adsorption sites represent the highest to lowest

energy binding sites, respectively. However, there is disagreement over whether gases can adsorb in the interstitial channels (IC), formed where three or more tubes meet on the interior of nanotube bundles. Talapatra et al.[17] measured adsorption isotherms and  $q_{st}$  values for  $\text{CH}_4$ , Xe, and Ne on two different samples of nanotubes, both prepared from the electric arc method. They computed the monolayer coverage for Xe and Ne from their isotherms and obtained specific surface areas of 38 and 41  $\text{m}^2/\text{g}$ , respectively. They concluded that similar results for the  $q_{st}$  and specific surface areas indicated that the same types of adsorption sites must be available for all gas species. Therefore, because Xe is too large to adsorb in interstitially, they inferred that none of the gases were adsorbing within interstitial channels.

Recently, Krungleviciute and coworkers[35] have used four different gases, Ne, Ar,  $\text{CH}_4$  and Xe, to measure the specific surface areas on HiPco nanotubes with the point-B method.[67] They observed that the measured specific surface areas for all the adsorbates are very close to one another, with values between about 320 to 340  $\text{m}^2/\text{g}$ . This is consistent with their earlier finding for electric arc nanotubes that the same types of sites are available for adsorption for all sorbates. Xenon is too large to adsorb in interstitial sites,[41] therefore, they concluded that the similar point-B surface areas indicate that gases do not adsorb in the interstitial channels.[35]

Shi and Johnson computed isotherms and isosteric heats for Ar,  $\text{CH}_4$ , and Xe adsorbing on two different models of nanotube bundles.[45] Their “homogeneous” model of nanotube bundles consisted of nanotubes of identical diameters perfectly packed on a hexagonal lattice. Their “heterogeneous” model consisted of nanotubes having various diameters that were imperfectly packed so that large interstitial defect sites were present. Many of these interstitial defect sites were large enough to allow adsorption of Xe. In contrast, the interstitial sites in the homogeneous bundle model did not accommodate adsorption of any of the gases they simulated. They found that the heterogeneous bundle model gave results that were consistent with experimental isosteric heat data[16, 19, 22, 24, 20] for electric arc nanotube samples. In contrast, simulations with homogeneous bundles were not in qualitative agreement with experiments, indicating that that adsorption of gases in defect interstitial sites is important at low coverages. Johnson *et al.*[46] have reached a similar conclusion. They found that the computed diffraction patterns with partially occupied interstitial sites

are in best agreement with experimental data for nanotubes produced by the electric arc method.

Recent efforts to resolve differences between experimental and computer simulation results for adsorption on SWNTs have found that as-produced HiPco nanotubes are best modeled as containing a fraction of nanotubes that are open.[58, 48, 60, 61] It is not clear from these experiments if models need to account for adsorption in interstitial channels in order to accurately describe the experimental data for HiPco SWNTs because the comparison between experimental and simulation methods are limited to adsorption capacities.

It is clear that no single model of nanotubes is capable of capturing the complexity due to differences in the nanotube samples resulting from different synthesis techniques. This has exacerbated the controversy over where gases adsorb on carbon nanotube bundles. Our aim in this chapter is to help resolve this controversy by comparing simulations utilizing different models of nanotube bundles with three key types of experimental data: specific surface areas, isosteric heats, and adsorption isotherms at low coverage. We examine different models for describing experimental data from bundles prepared by the electric arc and HiPco methods. The models we consider in this chapter include fully closed, fully opened, and partially opened bundles consisting of either homogeneous or heterogeneous distributions of nanotube diameters. The heterogeneous bundles include effects due to interstitial defects.

## 2.2 METHOD AND THEORY

### 2.2.1 Construction of bundles

A fully detailed model of carbon nanotube bundles would account for such things as the complex non-crystalline topology of the nanotubes in a sample, the curvature of the nanotubes, thermal vibrations, [68] chemical heterogeneity and functional groups on the side-walls and ends of the nanotubes, impurities (amorphous carbon, residual catalyst particles, etc.), and dilation of the nanotubes due to gas adsorption.[69, 70] Simulations have shown that thermal vibrations (flexibility) can safely be ignored for transport properties of gases in SWNTs

at high loadings.[71] It is reasonable to assume that flexibility issues are less important for equilibrium properties. Adsorption is typically affected by framework flexibility only in exceptional cases.[72, 73]

In this work we use models of nanotube bundles containing up to 100 individual nanotubes. The nanotubes are assumed to be rigid, straight, parallel, and without structural defects. We ignore the possibility of bundle dilation, in accord with the experimental work of Bienfait *et al.*, indicating bundles exposed to Ar do not dilate.[32] The bundles we examined in this work contained either homogeneous nanotubes (all the same diameter) or heterogeneous nanotubes, with diameters of individual tubes drawn from a distribution designed to mimic that observed experimentally. The characteristic feature of the heterogeneous nanotube bundles is that they all contain defect interstitial sites, large enough to accommodate Xe, the largest adsorbate studied in this work. The positions of the nanotubes in both homogeneous and heterogeneous bundles were optimized using the basin-hopping method.[74, 75, 76]

We have constructed smoothed functions to represent the potential due to nanotube-nanotube interactions in order to make the optimization computationally feasible. We have chosen to use  $(n, n)$  nanotubes to take advantage of symmetry in the unit cells in the direction of the nanotube axes. The smoothed potential between a  $(n_1, n_1)$  and  $(n_2, n_2)$  nanotube is given by

$$\begin{aligned} \langle u(r) \rangle &= \frac{\int_0^{\theta_{1\max}} d\theta_1 \int_0^{\theta_{2\max}} d\theta_2 \int_0^{Z_{\text{uc}}} dz_1 \int_0^{Z_{\text{uc}}} dz_2 u(r, \theta_1, \theta_2, z_1, z_2)}{\theta_{1\max} \theta_{2\max} Z_{\text{uc}} Z_{\text{uc}}} \\ &= \frac{\int_0^{\theta_{1\max}} d\theta_1 \int_0^{\theta_{2\max}} d\theta_2 \int_0^{Z_{\text{uc}}} dz_2 u(r, \theta_1, \theta_2, z_2)}{\theta_{1\max} \theta_{2\max} Z_{\text{uc}}}, \end{aligned} \quad (2.1)$$

where  $r$  is the distance between the centers of the two tubes,  $\theta_1$  and  $\theta_2$  are the rotational angles of tube 1 and tube 2 around their respective  $z$  axes, and  $z_1$  and  $z_2$  are the displacements in  $z$  direction of tubes 1 and 2, respectively. The unit cell height is represented by  $Z_{\text{uc}}$ , which is the same for all  $(n, n)$  tubes.  $u(r, \theta_1, \theta_2, z_2)$  is the position dependent potential between the two tubes when  $z_1$  is held fixed during the integration. The value of  $u(r, \theta_1, \theta_2, z_2)$  also depends on the heights of the two tubes. Tube 1 is set to have a height of one unit cell and tube 2 contains enough unit cells to mimic a nanotube of infinite length.

A pair-wise summation over all carbon-carbon interactions on different nanotubes is required to compute  $u(r, \theta_1, \theta_2, z_2)$ . We have used the Lennard-Jones (LJ) potential to compute the required carbon-carbon interactions. The effective LJ parameters of  $\sigma$  and  $\epsilon/k$  for carbon were set to be  $3.47 \text{ \AA}$  and  $28 \text{ K}$ , respectively, where  $k$  is the Boltzmann constant. The height of tube 2 was set to be 20 unit cells high because the van der Waals contribution beyond 20 unit cells was found to be negligible. The minimum image convention was used in the  $z$  direction to calculate the carbon-carbon interaction. We have applied Gaussian quadrature[77] to perform the integration in Eq. 2.1. The values of  $\langle u(r) \rangle$  versus  $r$  were fitted to a polynomial with 15 terms.[37, 31] Three polynomials are plotted as an illustrative example in Figure 2.2.

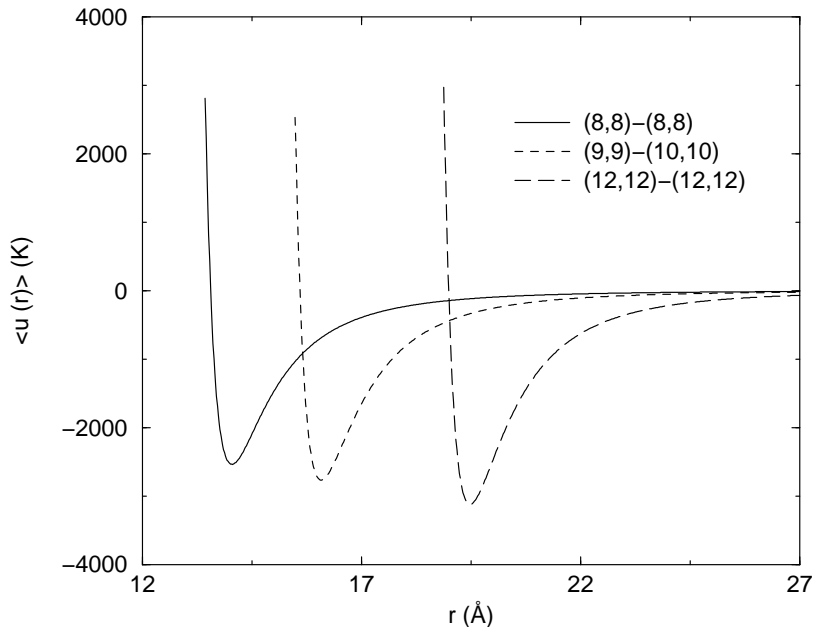


Figure 2.2: Potential energy between two tubes per unit cell of the reference tube. For clarity, only three sets of  $\langle u(r) \rangle$  are shown: the solid curve is (8,8)-(8,8), the short-dashed curve is (9,9)-(10,10), and the long-dashed curve is (12,12)-(12,12).

The equilibrium gap distance between two tubes is given by  $d_{\text{eq}} = r_{\text{eq}} - R(1) - R(2)$ , where  $r_{\text{eq}}$  corresponds to the well depth of  $\langle u(r) \rangle$  between the two tubes and  $R(1)$  and  $R(2)$

are the radii for the two tubes. The values of  $d_{\text{eq}}$  have been computed for different sets of tubes. There are 15 possible two-tube combinations considering  $(n, n)$  nanotubes ranging from (8,8) to (12,12). The  $\sigma$  value of 3.47 Å for carbon was found by trial-and-error such that all 15 values for  $d_{\text{eq}}$  lie between 3.199 and 3.205 Å, which is very close to the experimentally observed van der Waals gap of 3.2 Å.[54] Note that the value of  $\sigma_{\text{C-C}} = 3.47$  Å used for tube-tube potentials is somewhat larger than the value of  $\sigma_{\text{C-C}} = 3.40$  Å that is used extensively to compute graphite-adsorbate interactions.[78] Since there is no physical meaning to the value used to obtain the correct van der Waals gap, we have used the standard parameters when computing nanotube-adsorbate interactions.

The average smoothed potential between two tubes should be independent of which tube is considered as the reference. However, the  $\langle u(r) \rangle$  in Eq. (2.1) is the potential energy per unit cell of the reference nanotube and therefore the tube-tube potential is not exactly independent of the choice of reference. We have computed  $\langle u(r) \rangle$  by interchanging the subscripts and have found that the differences in the potentials due to the change of reference are negligibly small.

Our implementation of the basin-hopping method[74, 75, 76] applied to optimizing nanotube bundles is outlined here:

1. The initial positions for all the tube centers were generated by randomly placing tubes in a box while avoiding overlaps. Only the  $(x, y)$  coordinates of the tubes need to be generated, since the nanotube axes were aligned with the  $z$ -axis. The nanotubes were placed so that no two tubes had a van der Waals gap smaller than 4 Å. A square simulation box was used with a length of between 150 and 300 Å, depending on the number of tubes in the bundle.
2. The Broyden-Fletcher-Goldfarb-Shanno (BFGS) line minimization method[79] was then used to generate a local minimum energy configuration.
3. All tube centers were randomly moved in both  $x$  and  $y$  directions. Periodic boundary conditions were applied to keep the tubes in the box.
4. A new local minimum energy structure was obtained from the configuration obtained in step 3 using the BFGS method as in step 2.

5. The new minimum energy structure in step 4 was accepted with a probability of  $\min[1, \exp(-\delta U/kT)]$ , where  $\delta U$  is the energy difference between the new structure from step 4 and the previous structure, and  $T$  is the temperature of the simulation.
6. Steps 3 to 5 were repeated until a preset number of loops was reached.

The efficiency of the optimization procedure is dependent on temperature; if the temperature is too low, then moving out of a local minimum will be a rare event. The details of how temperature affects convergence is beyond the scope of this work. Instead, we take the pragmatic approach of setting the temperature to a high enough value that significant movement of the nanotubes takes place. The value we used was 1600 K, which is approximately 50 to 80% of the potential energy well depth between two nanotubes.

The maximum displacement of the Monte Carlo moves was adjusted so that approximately 50% of the trial translations were accepted. The maximum displacement parameter was adjusted during the entire optimization procedure, since detailed balance is not a requirement for optimization. We used a maximum of  $4 \times 10^5$  loops over the basin-hopping algorithm to optimize nanotube bundles.

### 2.2.2 Adsorbate-bundle interactions

The method used to generate the solid-fluid potential was very similar to the approach for determining the potential between two nanotubes. The adsorbate was positioned at a distance  $r$  from a nanotube and the angle and unit cell averaged potential was computed from the atom explicit potential. An eighth order polynomial was fitted to produce a description of the potential energy as a function of  $r$ . The Lennard-Jones parameters for Xe, Ar, and CH<sub>4</sub> are shown in Table 2.1. The solid-fluid potential was generated from these potentials along with the Lorentz-Berthelot combining rules using the standard graphene parameters from Steele of  $\epsilon_{C-C}/k = 28$  K and  $\sigma_{C-C} = 3.4$  Å.[78]

### 2.2.3 Simulations

Adsorption isotherms and isosteric heats of adsorption were computed from grand canonical Monte Carlo (GCMC) simulations[81] on both heterogeneous and homogeneous bundles.

Table 2.1: Lennard-Jones parameters[80] and specific surface areas (SSA) for Ar, CH<sub>4</sub>, and Xe adsorption on closed and partially opened bundles. Het1 and Het2 denote the values for the bundles shown in Fig 2.3. The values marked by Hom are taken from simulations performed on a 37 tube homogeneous bundle containing (9,9) type nanotubes. ‘%Open’ refers to the roughly 11% opened bundle simulations. The Lennard-Jones parameters for the adsorbates in simulations are also included in the table. The isotherm temperatures used in experiments and simulations are listed in the fourth column. Exp denotes the specific surface areas from experiments. [35] The last row lists the relative spread in the specific surface areas, defined as (max-min)/max. Ar and CH<sub>4</sub> isotherms were run at a temperature of 77 K and Xe at 145 K.

Gas	$\sigma_g$ (Å)	$\epsilon_g/k$ (K)	SSA (m <sup>2</sup> /g)						Exp
			Closed Hom	Closed Het1	Closed Het2	%Open Hom	%Open Het1	%Open Het2	
Ar	3.42	124.07	220	265	314	263	299	357	324
CH <sub>4</sub>	3.73	147.90	238	285	330	296	318	361	337
Xe	4.10	221.00	187	251	294	234	300	343	328
Spread			0.21	0.12	0.11	0.21	0.06	0.05	0.04

The calculation details have been described elsewhere.[31, 45] The height of the simulation box was typically set to at least  $10 \sigma_g$ , where  $\sigma_g$  is the Lennard-Jones  $\sigma$  parameter for the adsorbates. The height of the simulation box was increased to values between 100 and  $5000 \sigma_g$  for simulations at low pressure in order to improve statistics. The  $x$  and  $y$  dimensions of the simulation box were set to be the same, typically between 150 and  $250 \text{ \AA}$ . This was found to be large enough to make interactions with nanotubes in image boxes negligible. The total number of simulation steps was typically set to  $10^7$  and  $10^8$  for equilibration and production, respectively.

## 2.3 RESULTS

### 2.3.1 Bundle production

We have constructed homogeneous bundles consisting of 25, 45, 70, and 100 (10,10) nanotubes, five homogeneous bundles containing 37 nanotubes with index (8,8), (9,9), (10,10), (11,11), or (12,12), and heterogeneous bundles containing 45 and 100 nanotubes. Diameter distributions in the heterogeneous bundles were chosen to mimic those found experimentally for nanotubes produced by laser ablation.[52] The heterogeneous bundle containing 45 tubes is composed of 10 (8,8), 25 (9,9), 5 (10,10), and 5 (11,11) tubes. The average diameter and standard deviation for this bundle are  $12.36 \text{ \AA}$  and  $1.18 \text{ \AA}$ , respectively. The heterogeneous bundle consisting of 100 nanotubes contains 6 (8,8), 29 (9,9), 35 (10,10), 28 (11,11), and 2 (12,12) nanotubes. The average diameter and standard deviation for the bundle are  $13.44 \text{ \AA}$  and  $1.28 \text{ \AA}$ , respectively. These average diameters are very close to the mean observed experimentally,[52] but the diameter standard deviations are less than the experimental value of  $2 \text{ \AA}$ .[49] We expect our models to exhibit fewer interstitial channel defects than real samples of nanotubes because a smaller standard deviation in the diameter distribution results in a more ordered hexagonal configuration and smaller interstitial channel defects.

We have minimized the total energy of each bundle starting from ten different initial configurations. For the homogeneous bundle containing 25 nanotubes, the same lowest energy structure was produced from two of the ten runs. It is possible that the true global minimum energy structure has been found for this homogeneous bundle. For other homogeneous bundles containing 45, 70, and 100 nanotubes, no two runs yielded the same lowest energy structure, indicating that it is unlikely that the global minimum energy structure has been identified. Note that it is not our goal to identify the global minimum energy structure for the nanotube bundles. The experimentally produced bundles are “quenched” structures and are therefore not likely to be in their lowest energy states and hence we believe that a partially optimized structure is a more appropriate model for experimentally produced nanotube bundles than a globally optimized bundle. For homogeneous bundles containing 70 or fewer tubes, minimization always resulted in packing of the tubes into perfect 2-d hexagonal lattices. For the largest bundle containing 100 tubes, perfect 2-d packing was observed in four runs. The other six runs resulted in 2-dimensional hexagonal packing with defect interstitial channels inside the bundle about the size of one nanotube. For the heterogeneous bundles consisting of 45 and 100 tubes, we always obtained imperfect packing with interstitial defects occurring inside the bundles. Some IC defects are large enough to accommodate gas adsorption. Two minimum energy heterogeneous structures are shown in Figure 2.3. The two structures consist of the same number of tubes and have the same diameter distribution. The bundle on the left, denoted Het1, was obtained from 1000 loops of the basin-hopping algorithm while the bundle on the right, Het2, was obtained from only one basin-hopping step. Het1 exhibits more ordered packing than Het2, leading to fewer and smaller IC defects in Het1. The potential energy summed over all pairs of tubes for Het1 is about 8% lower than that for Het2.

The van der Waals gaps between neighboring tubes in many minimum energy structures have been computed. The gap values in perfectly packed homogeneous bundles are between 3.202 and 3.203 Å. These values are close to both the equilibrium gap between two tubes and the observed experimental van der Waals gap. In contrast, some gaps in imperfectly packed heterogeneous bundles are less than 3.2 Å. The Het2 bundle in Figure 2.3 contains 90 gaps total, 52 of which exhibit values less than 3.2 Å. The Het1 bundle in Figure 2.3

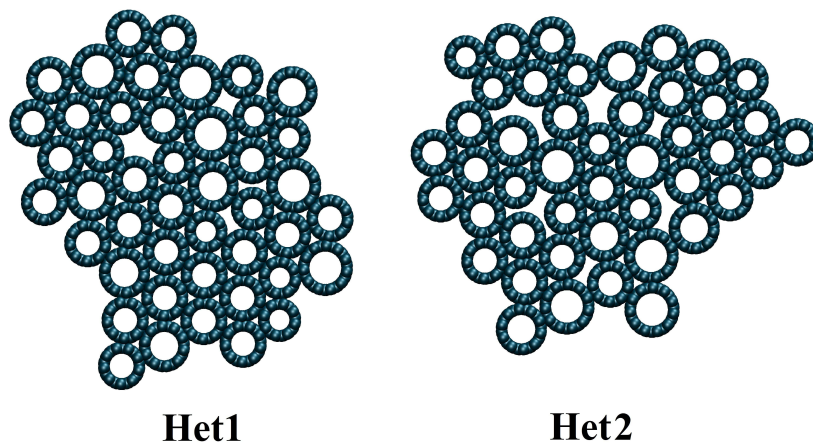


Figure 2.3: Two minimum energy structures obtained using the basin-hopping method. Both heterogeneous bundles contain 45 tubes with the same diameter distribution. The bundle on the left, Het1, was optimized for 1000 basin-hopping steps, while the bundle on the right, Het2, was optimized for a single basin-hopping step.

contains 102 nearest neighbor gaps, 49 of which are less than 3.2 Å. Most of the smaller gaps are between 3.15 Å and 3.20 Å with the smallest gap being 3.055 Å. The smaller gaps observed in heterogeneous bundles are a result of packing nanotubes having a distribution of diameters that preclude perfect packing.

### 2.3.2 Adsorption results on closed bundles

Low pressure isotherms for CH<sub>4</sub> at 159.8 K from simulation and experiment[16] are shown in Figure 2.4. Nanotubes generated by the electric arc method were used in the experiments.[16] A purity of 60% by weight was assumed in simulations because this is the reported purity of carbon nanotubes prepared by the electric arc method.[19, 22, 82] In the region of low pressure (below about 0.2 torr), simulation snapshots for heterogeneous bundles indicate that most gases adsorb inside IC defects. We note that snapshots are not a quantitative tool, but are useful for qualitative analysis. Very few molecules are observed to adsorb in the groove sites at low pressure.

For the homogeneous bundle simulations, gas molecules do not adsorb in the interstitial channels at the temperatures and pressures of interest. However, heterogeneous bundles contain large interstitial channels created by imperfect packing and these have higher energy binding sites than groove sites on the outer surface.

As seen in Figure 2.4, the amount adsorbed in heterogeneous bundles can be as much as two orders of magnitude higher than in homogeneous bundles at low pressures due to adsorption in the interstitial defect channels present in heterogeneous bundles. Comparing with experiments, we note that simulations on heterogeneous bundles underpredict the amount measured by experiments[16] by about a factor 2 to 6, whereas the simulations on homogeneous bundles underpredict the amount adsorbed by a factor of about 10<sup>2</sup>. Although neither of the simulated isotherms are in quantitative agreement with experiments in Figure 2.4, the simulations on the heterogeneous bundles are in much better qualitative agreement with the experimental data than the simulations on the homogeneous bundles.

Isotherms for Xe adsorption on closed bundles at 250 K are shown in Figure 2.5. This represents the low coverage region used by Migone and coworkers to measure the binding

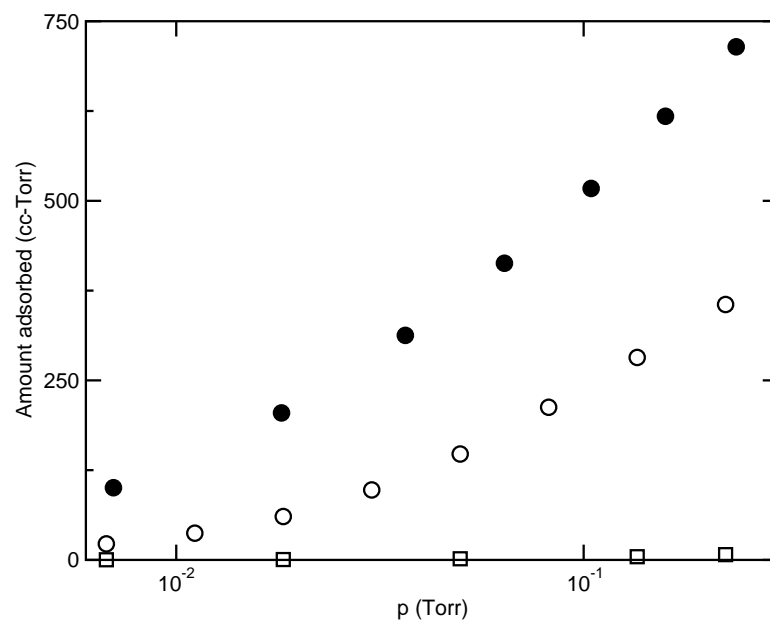


Figure 2.4: Isotherms from experiment and simulations for  $\text{CH}_4$  adsorption on closed bundles at 159.8 K. Open circles correspond to the Het2 45 nanotube bundle shown in Figure 2.3. The open squares are for a homogeneous bundle containing 45 (10,10) tubes. Also shown are the experimental data (filled circles) for nanotubes generated by the electric arc method.[16]

energy and isosteric heat on nanotubes prepared by the electric arc method.[22] As before, we have assumed a purity of 60% for carbon nanotubes in the experimental sample in order to compare our calculated isotherms with experimental data. For the heterogeneous bundle, simulation snapshots show that most gas molecules adsorb inside IC defects and only a few adsorb in the groove sites at low coverage. In contrast, the homogeneous bundle IC sites are not occupied because Xe is too large to adsorb in these channels. The groove sites accommodate a small number of gas molecules, but most of the groove sites are unoccupied. The isotherm for the heterogeneous bundle is very close to the experimental data while the amount adsorbed on the homogeneous bundle is about 30 times less than experiment. Isotherms at temperatures of 210 and 295 K (not shown here) also exhibit similar characteristics to the 250 K results. Isotherms at these three temperatures indicate that heterogeneous bundles produce isotherms in much better agreement with the experiments at low coverage (low pressure) than homogeneous bundles.

Migone and coworkers have derived isosteric heats of adsorption from experimentally measured isotherms of CH<sub>4</sub> on electric arc nanotubes in the low, intermediate, and high coverage regions.[16, 19] The experimental isotherms were measured in the range of 69 to 195 K. It is often assumed that  $q_{st}$  is independent of temperature.[83] We have used three temperatures used in the experiments to study the effect of temperature on the isosteric heat. Isotherms were simulated at 110, 159.8, and 194.7 K. The three sets of isotherm simulations were performed on the same heterogeneous bundle, Het1 in Figure 2.3. The  $q_{st}$  values are plotted in Figure 2.6.

As might be expected, the values of  $q_{st}$  at each of the three temperatures are very similar in the low and high coverage regions. The differences are less than 10% over most of the coverage range. However, the  $q_{st}$  curves in the intermediate coverage region display qualitative differences. The isosteric heat data for the 110 K isotherm (circles) clearly exhibits a plateau in the region near point ‘a’. The 159.8 K isotherm (diamonds) lacks this feature, giving a steady decrease in  $q_{st}$  (compare point ‘b’ with point ‘a’). The difference in isosteric heats between points ‘a’ and ‘b’ can be explained in terms of accessibility of sites at each of the temperatures. Simulation snapshots indicate that virtually all molecules adsorb into IC defects and groove sites at point ‘a’. Almost no adsorption was observed on the

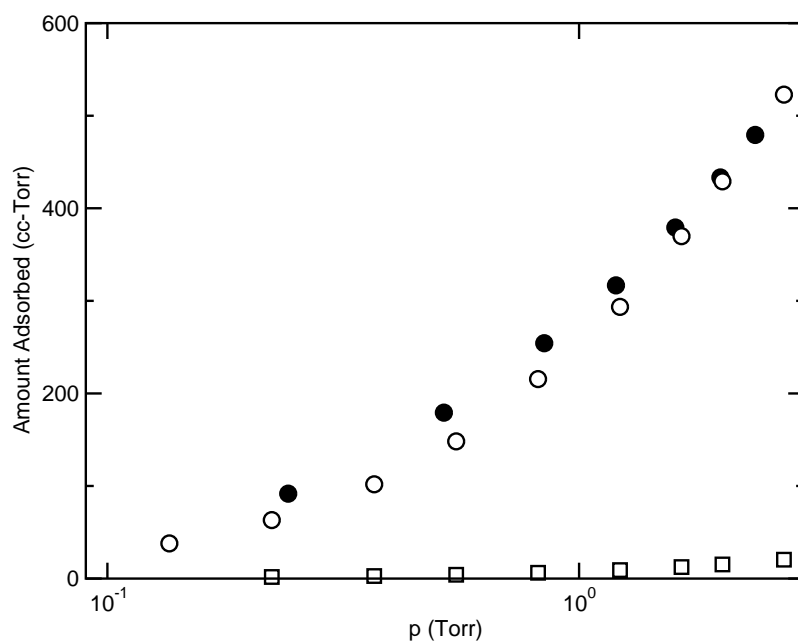


Figure 2.5: Isotherms for Xe adsorption on closed bundles at 250 K. Open circles and squares are for 45 tube heterogeneous and homogeneous bundles, respectively. The simulations shown are for the Het2 bundle from Figure 2.3 and a homogeneous bundle consisting of (10,10) SWNTs. Experimental data on electric arc generated nanotubes are plotted as filled circles.[22]

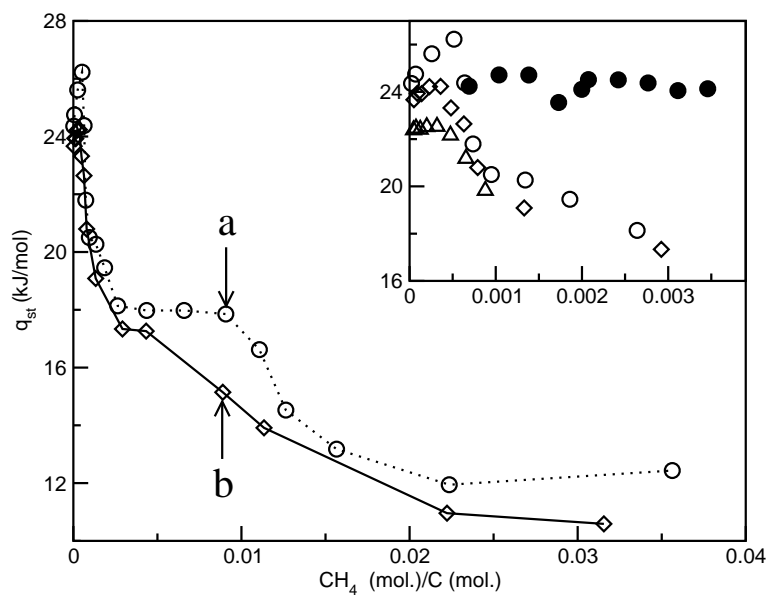


Figure 2.6: Temperature effects on isosteric heat for CH<sub>4</sub> adsorption on closed bundles. All the simulations were performed on the same heterogeneous 45 tube structure (Het1 in Figure 2.3). The diamonds and the open circles are for 159.8 and 110 K, respectively. Also shown in the inset are the experimental data on nanotubes generated by the electric arc method (filled circles) [19] and simulation results at 194.7 K (triangles) at low coverages. The lines are drawn as a guide to the eye.

external surfaces of the nanotube bundle. However, for the higher temperature isotherm, point ‘b’, about 9% of the total number of gas molecules adsorb on the outer surface, which exhibits lower binding energy than IC defects and groove sites.[45] The high temperature allows adsorbates to sample sites having a wider range of binding energies, according to the Boltzmann distribution. This leads to a higher isosteric heat at point ‘a’ than at point ‘b’.

The inset in Figure 2.6 shows the isosteric heats at very low coverage. Simulation snapshots for the 110 K isotherm show that gases only adsorb inside two of IC defects at coverages less than  $5 \times 10^{-4}$  mol(CH<sub>4</sub>)/mol(C). The isosteric heat is increased due to enhanced adsorbate-adsorbate interactions present within the narrow interstitial defect channels. When the pressure is increased beyond the value at which the amount adsorbed exceeds  $5 \times 10^{-4}$  mol(CH<sub>4</sub>)/mol(C), gases begin adsorbing into IC defects having lower binding energies. This leads to a decrease in  $q_{st}$  observed in the inset. The isosteric heat data for the 194.7 K isotherm (triangles) shows qualitatively different behavior compared with the 110 K isosteric heat. The higher temperature allows gases to populate IC defect channels having lower binding energies, again according to the Boltzmann distribution. The effect of temperature on isosteric heat has also been studied for a homogeneous bundle at low coverages (not shown). The results are similar to those shown in Figure 2.6 for points ‘a’ and ‘b’, i.e., there is a plateau in the low temperature isosteric heat due to gases being effectively confined to the groove sites, but no plateau in the higher temperature isosteric heats. Note that the simulation results are in reasonable agreement with experimental values of  $q_{st}$  shown in the inset (filled circles). It has been previously shown that  $q_{st}$  values calculated on homogeneous bundles are not in good agreement with experiments, due to a large plateau region.[45]

We have investigated the effect of temperature on the isosteric heat for Xe adsorption on closed homogeneous and heterogeneous bundles. Simulations were performed at temperatures of 110.6 and 150 K and are shown in Figure 2.7. This spans the temperature range used by Migone *et al.*[18] to measure the isosteric heat on the external surface of a nanotube bundle prepared by the electric arc method. There is good agreement between the  $q_{st}$  values calculated on the same bundle (both homogeneous and heterogeneous) at the two different temperatures over the entire range of coverage. In other words, the isosteric heat is apparently independent of temperature.

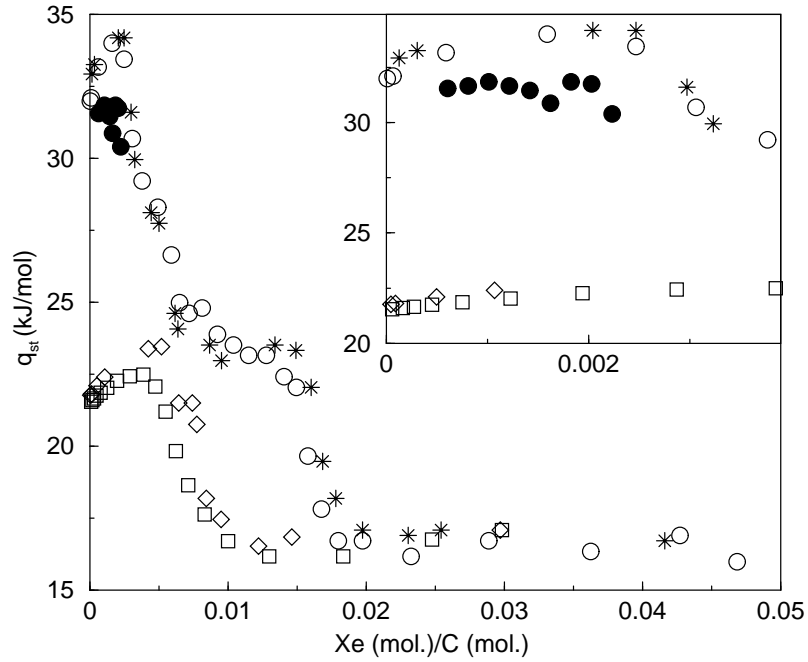


Figure 2.7: Temperature effects on isosteric heat for Xe adsorption on closed heterogeneous and homogeneous bundles. All bundles contain 45 tubes. Squares and diamonds are results on the same 45 (10,10) homogeneous bundle using temperatures of 150 and 110.6 K, respectively. Open circles and stars are results for the same 45 tube heterogeneous bundle (Het2 in Figure 2.3) using temperatures of 150 and 110.6 K, respectively. Also shown are experimental isosteric heat values on electric arc generated nanotubes at low coverage (filled circles). [22] The inset shows the same data at low coverage.

The effect of temperature on  $q_{\text{st}}$  for  $\text{CH}_4$  in Figure 2.6 is fundamentally different than the effect of temperature for Xe in Figure 2.7. This can be explained in terms of differences in the solid-fluid interaction parameters,  $\epsilon_{\text{sf}}/k$ , for  $\text{CH}_4$  and Xe, which are 64.4 and 78.7 K, respectively. We can define a reduced temperature  $T^* = kT/\epsilon_{\text{sf}}$  that characterizes the ratio of the kinetic energy to the potential energy in the system (for a fixed bundle). Ignoring adsorbate size effects on the potential energy, we can say that the Boltzmann factor for the difference in energy between gases adsorbed on the groove site and on the external surface of the nanotube is proportional to  $\Gamma(T) = \exp(-1/T^*)$  for both  $\text{CH}_4$  and Xe. The values of  $\Gamma$  for  $\text{CH}_4$  are 0.67 (159.8 K) and 0.56 (110 K). For Xe,  $\Gamma(T) = 0.59$  (150 K) and 0.49 (110 K). Comparing these values, we see that Xe at 150 K is at approximately the same reduced condition as  $\text{CH}_4$  at 110 K. In other words, the sites populated by  $\text{CH}_4$  at 110 K would be the same ones populated by Xe at 150 K. Hence, the isosteric heats for Xe appears to be independent of temperature in Figure 2.7 because for Xe at both 110 and 150 K the higher energy surface sites are not significantly populated in the plateau region (between about 0.01 and 0.015 Xe/C).

The experimental  $q_{\text{st}}$  values at low coverage[22] are also plotted in Figure 2.7. As noted previously,[45] the simulations on heterogeneous bundles are in good agreement with the experiments, while the homogeneous results are not.

We have studied the effects due to the number of tubes in the bundle and the degree of optimization of the bundle on  $q_{\text{st}}$ . Values of  $q_{\text{st}}$  for  $\text{CH}_4$  on the Het1 and Het2 nanotube bundles from Figure 2.3 and a heterogeneous bundle containing 100 nanotubes are plotted in Figure 2.8. The bundle containing 100 nanotubes (open circles) and the less optimized 45 tube Het2 bundle (stars) give results in good agreement with experiments (filled circles) at low coverages, shown as the inset in Figure 2.8. These bundles show wider plateau regions at low coverage than the more highly optimized Het1 bundle structure (diamonds). This is due to the larger number of IC defects in these bundles as compared to the Het1 structure. The experimental data from Migone and coworkers[16, 19] are for nanotubes prepared by the electric arc method. We have carried out similar calculations for Ar and found the same trends as for  $\text{CH}_4$ , namely, that the larger nanotube bundles and those with more IC defect sites are in better agreement with experimental data.

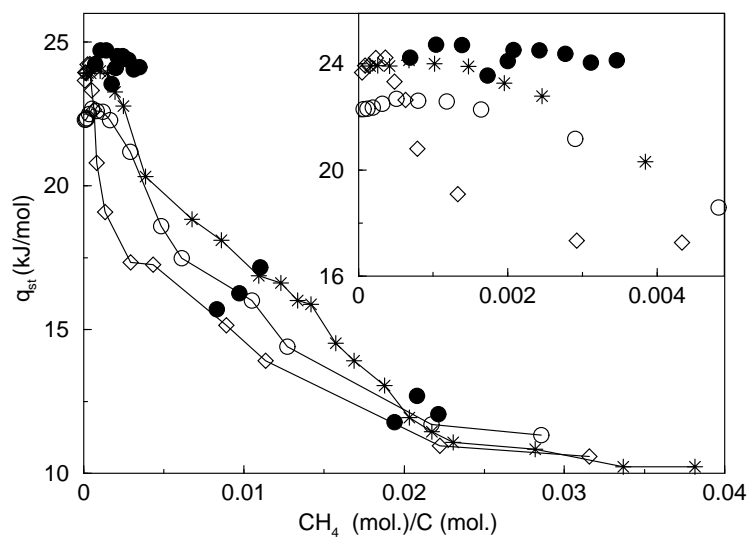


Figure 2.8: Closed 45 tube heterogeneous bundle packing effects on isosteric heat of adsorption for  $\text{CH}_4$ . All simulations were performed at 159.8 K. Diamonds and stars correspond to the Het1 and Het2 bundles shown in Figure 2.3, respectively. Open circles are for simulations performed on a heterogeneous bundle containing 100 tubes. Also shown are the experimental data (filled circles) on nanotubes generated by the electric arc method. [16, 19] Lines are drawn to guide the eye.

The effects of bundle size and degree of optimization on gas adsorption and  $q_{st}$  have also been studied for homogeneous bundles. Simulations on homogeneous bundles containing 25, 45, 70, and 100 (10,10) nanotubes gave  $q_{st}$  values that were virtually identical. The degree of optimization for bundles containing 45 nanotubes did not affect  $q_{st}$  as long as no large (defect) interstitial channels were present in the bundles.

It is clear from our results that  $q_{st}$  is sensitive to the presence of defect ICs at low coverage and that simulation data for heterogeneous bundles are in much better agreement with experimental data for electric arc nanotubes than data from the homogeneous bundle model. What is not clear is how  $q_{st}$  depends on the structure of the bundle apart from the defect IC sites. One might assume that the external groove sites are fairly insensitive to whether the bundle is homogeneous or heterogeneous. In order to investigate this issue we have studied the difference in adsorption capacity for the groove site and the external surface between the homogeneous and heterogeneous bundles. For the Het1 bundle in Figure 2.3, four inside IC defects and one outside channel enclosed by three neighboring tubes (the lower right part of the bundle) were excluded from adsorbing gases in the simulation. These excluded regions contain the highest binding energy sites on the bundle. The isosteric heats and isotherms for these bundles are shown in Figure 2.9 and Figure 2.10, respectively. The adsorbate was chosen to be  $\text{CH}_4$ . The results for both bundles are very similar. The largest difference in  $q_{st}$  between homogeneous and heterogeneous bundles is about 6%. The largest difference in coverage at the same pressure is about 2%. In short, the above simulations strongly indicate that the adsorption capacity for groove sites and the rounded external surface is insensitive to size, heterogeneity, and packing of tubes in the bundles.

### 2.3.3 Adsorption results on opened and partially opened bundles

We have seen that simulated isotherms and  $q_{st}$  values using a heterogeneous bundle with many IC defect sites are in better agreement with experimental data for electric arc bundles. However, we have seen from Figure 2.1 that  $q_{st}$  from electric arc and HiPco nanotubes are quantitatively different. In this section we examine the hypothesis that HiPco SWNTs can

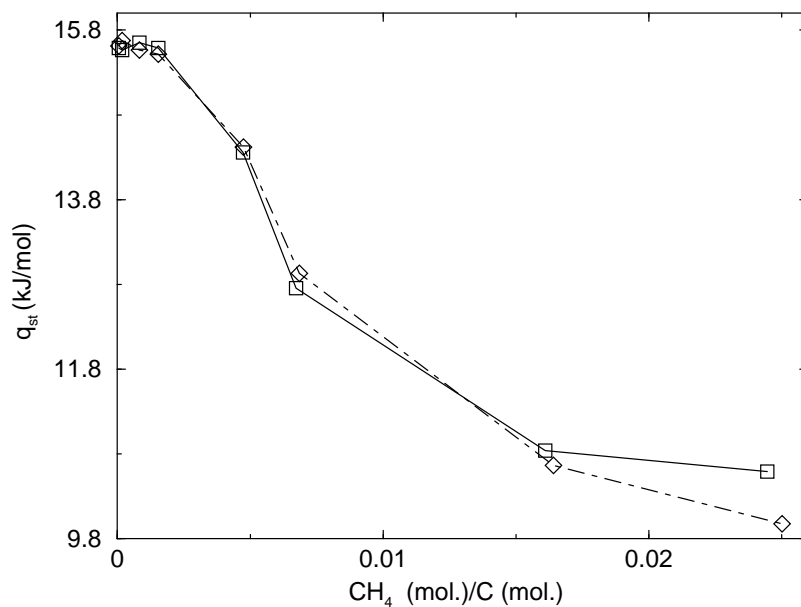


Figure 2.9: Isosteric heats of adsorption for CH<sub>4</sub> on closed homogeneous and heterogeneous bundles at 159.8 K. Diamonds and squares correspond to heterogeneous and homogeneous 45 nanotube bundles, respectively. The heterogeneous bundle used here is the more energy minimized structure (Het1 in Figure 2.3). The interstitial defects and one external surface defect on the heterogeneous bundle were blocked from adsorption during simulations. Lines are drawn to guide the eye.

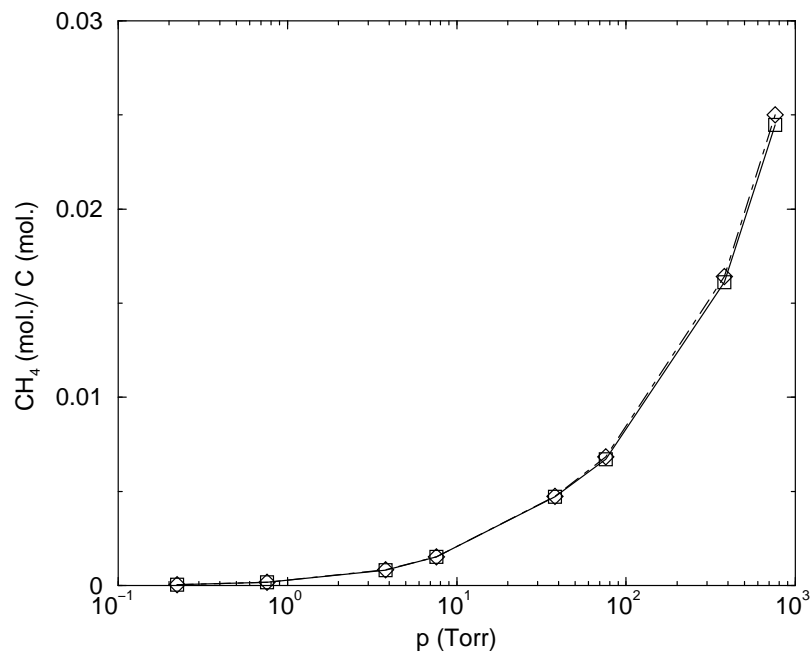


Figure 2.10: Isotherms for CH<sub>4</sub> adsorption on closed homogeneous and heterogeneous bundles at 159.8 K. The two bundles are the same as those in Figure 2.9. The interstitial defects and one external surface defect on the heterogeneous bundle were blocked from adsorption during simulations. Lines are drawn to guide the eye.

be described by a model consisting of a homogeneous bundle containing a fraction of opened nanotubes, as has been previously suggested.[58, 59, 48, 60, 61]

We therefore use experimental  $q_{st}$  data for Xe on HiPco nanotubes[62] to deduce what diameter nanotube best describes the low-coverage  $q_{st}$  values. To this end, we have plotted the zero coverage  $q_{st}$  values for Xe as a function of tube radius in Figure 2.11. We have found that the (9,9) tubes give low-coverage  $q_{st}$  values in good agreement with experiments, as can be seen from Figure 2.12.

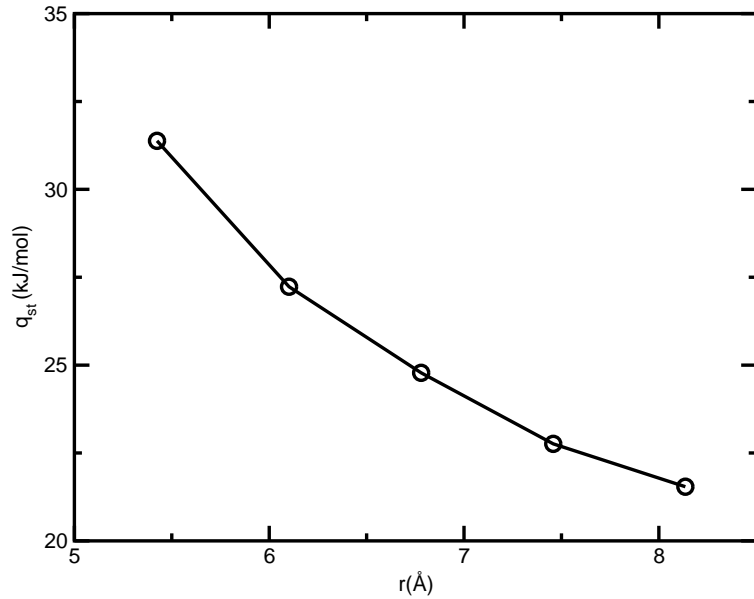


Figure 2.11: Isosteric heat values for Xe using different opened homogeneous bundles containing 37 nanotubes at 145.3 K. The  $x$ -axis is the radius of the nanotubes used in each simulation. From left to right, they are (8,8), (9,9), (10,10), (11,11), and (12,12). The isosteric heat values were taken at coverages less than 0.001 Xe (mol)/C (mol). The line is drawn to guide the eye.

Simulations of bundles consisting of all open nanotubes for Xe are in poor qualitative agreement with experimental data. We therefore performed a series of simulations with different fractions of opened nanotubes in both a homogeneous (9,9) bundle and the Het2 bundle from Figure 2.3. After investigating different numbers of opened nanotubes, we found

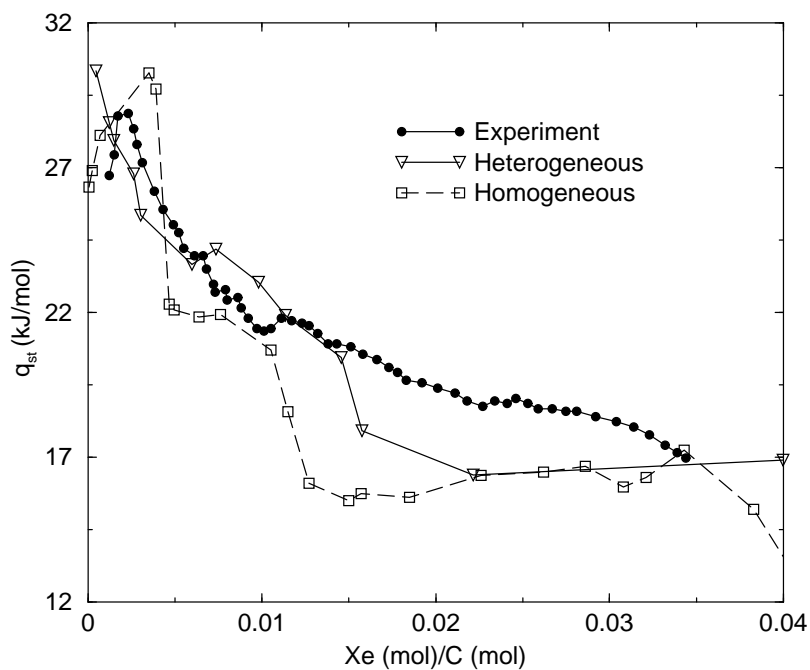


Figure 2.12: Isosteric heats of adsorption from simulations for Xe on a partially opened homogeneous bundle consisting of 37 (9,9) nanotubes (squares) and on the partially open Het2 bundle from Figure 2.3 (triangles). Both bundles have about 11% of their tubes opened. Experimental data from Migone and coworkers[62] are plotted as filled circles. The nanotubes were generated by the HiPco method.

that about 11% open nanotubes for both the (9,9) bundle containing 37 nanotubes (4 open tubes) and the 45 tube Het2 bundle (5 open tubes) gave  $q_{st}$  values that were in fairly good agreement with experiments over the entire range of coverages. These data are plotted in Figure 2.12, along with experimental data.[62] The five opened nanotubes in the Het2 bundle consisted of one each of the (8,8), (9,9), (10,10), and (11,11) SWNTs and an additional tube. We have studied the effect of identity,  $(n, n)$ , of the fifth opened nanotube on the amount adsorbed. We found only minor differences (less than 3%) in the total amount adsorbed when opening two (8,8) versus two (11,11) tubes. It is not possible to tell whether the partially opened homogeneous (9,9) nanotube bundle or the partially opened Het2 bundle gives the best agreement with experiments from the limited  $q_{st}$  data available for gases adsorbing on HiPco nanotubes. We therefore next consider a different metric for characterization of gas adsorption, the specific surface area.

#### 2.3.4 Specific surface area

The specific surface areas for Ar, CH<sub>4</sub>, and Xe have been calculated for closed, open, and partially opened nanotubes on both homogeneous and heterogeneous bundles. The simulations were performed at the same temperatures as in the experiments,[35] which are 77.10, 77.09, and 145.3 K for Ar, CH<sub>4</sub>, and Xe, respectively.

An example illustration showing the calculation of the specific surface area is shown in Figure 2.13 for Xe adsorption on a heterogeneous bundle. Many points on the isotherm are needed to obtain a very smooth curve. Once that is complete, we used the point-B method to compute the specific surface area, which is the same method used in experiments.[35] When implementing the point-B method, it is assumed that isotherm will have a dramatic slope change at low coverage followed by a linear region. A line is then fitted to the linear region of the isotherm. The tangential point of this line is defined as the point at which the line deviates from the isotherm. In Figure 2.13, this deviation occurs at a relative pressure and amount adsorbed of 0.15 and 1212.1, respectively.

We have verified from examining simulation snapshots that the coverage of the surface of the nanotube bundle at the tangent point is nearly complete. It is important to note,

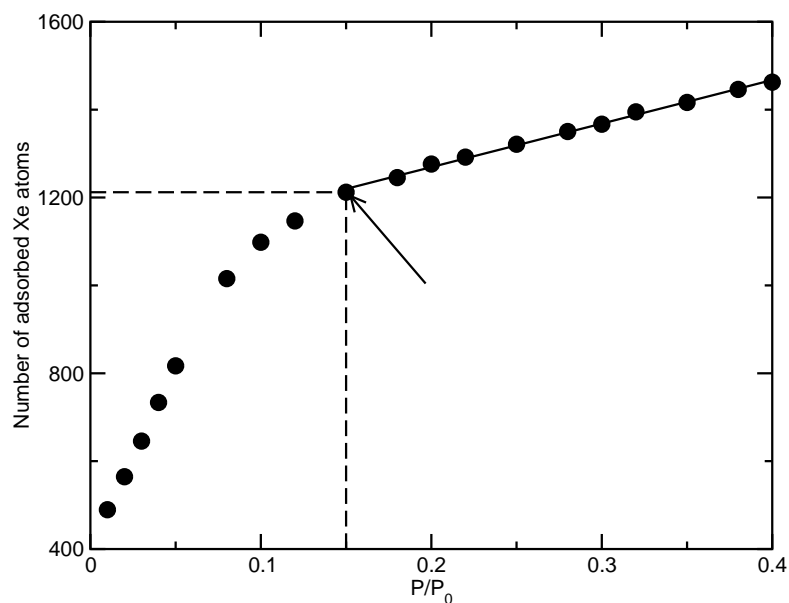


Figure 2.13: Adsorbed amount versus relative pressure of  $P/P_0$  for Xe at 145 K, where  $P_0$  is the saturation vapor pressure at this temperature. The solid line is the linear fitting of the data between 0.15 and 0.4 for  $P/P_0$ . The linear correlation coefficient for this line is 0.998. The solid arrow denotes the tangential point where the solid line and the isotherm curve meet. The vertical and horizontal long dashed lines denote the relative pressure and the monolayer coverage corresponding to the tangential point.

however, that there really is not a point at which the surface of any nanotube bundle is completely covered with a monolayer of adsorbate molecules. This is because second layer groove sites start to fill before the entire convex surface of the nanotubes is completely filled, so that first and second layer sites are being filled at the same bulk pressure. Hence, the notion of monolayer completion for a nanotube bundle is somewhat ambiguous.

The specific surface area (SSA) was calculated from

$$\text{SSA} = N_{\text{ads}}\pi \left(\frac{\sigma_g}{2}\right)^2 \left(\frac{6022}{12N_c}\right), \quad (2.2)$$

where SSA has units of  $\text{m}^2/\text{g}$ ,  $N_{\text{ads}}$  is the number of molecules adsorbed at the tangential point, and  $N_c$  is the number of carbon atoms in the bundle. The numerical values of 12 and 6022 are the molecular weight of carbon and Avogadro's number, respectively, with the latter being multiplied by factor of  $10^{-20} \text{ m}^2/\text{\AA}^2$  to convert  $\sigma_g$  from units of  $\text{\AA}$  to m. The results from the simulations and experiment are shown in Table 2.1. The columns refer to the type of bundle used in the simulations. Hom refers to a 37 nanotube homogeneous bundle containing (9,9) nanotubes. Het1 and Het2 refer to the more and less energy minimized structures on the left and right sides of Figure 2.3, respectively. The specific surface area values calculated from bundle Het1 are uniformly smaller than those for Het2. This is due to the larger number of IC defects contained in the less energy minimized bundle Het2. It is important to note that our goal is to identify a bundle model that has the same SSA trend as the experiments, not necessarily to match the measured SSA values from experiment, because the absolute value of SSA is dependent on the number of nanotubes in a bundle, the impurities present in the sample, and other factors difficult to account for in simulations. The striking feature of the experimental data is that the SSA values for the three adsorbates are roughly the same. We define the relative spread of the data to be the  $(\text{max}-\text{min})/\text{max}$ , where max and min are the largest and smallest values of the data set, respectively. The spread of the experimental data is 4%, which indicates the SSA values are very weakly dependent of adsorbate type.

The underlying assumption behind the experimental work on SSA measurements is that if nanotube bundles present the same adsorption sites to each adsorbate then the measured SSA would be independent of adsorbate size. Specifically, they assumed that if none of the

gases adsorb in the IC sites that adsorbates with different diameters will give essentially the same measured SSA.[17, 35] The ratio of apparent surface area to geometric surface area for close-packed spherical molecules on a planar surface is  $\pi\sigma_g^2/(2\sqrt{3}\sigma_g^2) = \pi/(2\sqrt{3})$  and is independent of molecular diameter,  $\sigma_g$ . Hence, for spherical adsorbates on a planar surface, the specific surface area is independent of adsorbate diameter. We have verified that GCMC isotherms for Ar, CH<sub>4</sub>, and Xe on planar graphite give point-B specific surface areas that are independent of adsorbate size. We carried out isotherm simulations for Ar, CH<sub>4</sub>, and Xe at the temperatures listed in Table 2.1. We used the 10-4-3 graphite potential with the same LJ potentials used in the nanotube simulations. The graphite surface was taken to be square, 100 Å on a side. We observed that the density near monolayer completion as deduced by the point-B method was only about 72% of the closed-packed density. The SSA values for Ar, CH<sub>4</sub>, and Xe from our simulations had a spread of about 1%, indicating that SSA is indeed independent of adsorbate size for spherical molecules on a planar surface.

In contrast to planar surfaces, the SSA on nanotube bundles is not independent of adsorbate size. The groove sites and non-planar surfaces of closed nanotube bundles make SSA depend on the diameter of the adsorbate, even if adsorption in the IC sites is not allowed. To illustrate this point at the most simple level, consider adsorption of spherical molecules on a single isolated closed SWNT. Exactly the same adsorption sites (external surface) are available to Ar, CH<sub>4</sub>, and Xe, but the measured SSA values have significant dependence on the adsorbate molecular diameter. SSA results for isolated (8,8), (9,9), and (10,10) nanotubes have calculated spreads of 10%, 8%, and 11%, respectively. The rather large spread is due to the incommensurate nature of the packing of molecules on the nanotube. Perfect packing of spheres on a cylinder can only occur if the diameter of the spheres is commensurate with the diameter of the cylinder, so that an integer number of molecules exactly makes a close-packed ring on the circumference of the cylinder. Spheres that are incommensurate with the cylinder will exhibit frustrated packing, with larger diameter molecules typically showing the largest frustration. The same sort of incommensurate packing occurs on the surface of nanotube bundles because groove sites impose boundaries for the adsorbate molecules. This is precisely what is observed in Table 2.1. The closed homogeneous bundle has a spread of

21%, even though the exact same sites are accessible to Ar, CH<sub>4</sub>, and Xe, since none of these gases adsorb in the interstitial channels.

In contrast, the heterogeneous bundles have spreads of 12% and 11%. The SSA values for closed heterogeneous bundles are in much better agreement with experiments than closed homogeneous bundles. However, the spread for the simulations is still about a factor of three larger than the experimental data. Simulation results for partially opened bundles are also given in Table 2.1. Surprisingly, the homogeneous bundle again has a spread of 21%. The heterogeneous bundles have spreads of 6% and 5%, for Het1 and Het2, respectively. The reason for the lack of improvement in SSA for the partially opened homogeneous bundle is that Xe cannot pack efficiently in (9,9) nanotubes. In contrast, the opened (10,10) and (11,11) nanotubes in the heterogeneous bundles significantly increase the relative amount of Xe adsorbed at monolayer completion and hence reduces the spread.

As before, we opened one each of the types of nanotubes in the heterogeneous bundles, plus another tube. The the identity of the fifth tube does not significantly effect the spread. The range in the spreads due to changing the diameter of the fifth tube in the Het2 bundle is 4.7 to 5.1%. Considering both the isosteric heats and SSAs, partially opened heterogeneous bundles are the best models for HiPco nanotubes because simulation data using these models are in better agreement with experimental data than other models.

Migone and coworkers have also included Ne results in their comparison of specific surface areas.[35] Quantum effects may be very important for Ne at a temperature of 22 K, where the experimental data were taken. Simulations including quantum effects for Ne will be considered in the next chapter.

## 2.4 CONCLUSION

We report simulation results on various nanotube bundle models to provide insight into the controversy over where gases adsorb. We use three criteria as a basis for comparison: adsorption isotherms, isosteric heats of adsorption, and specific surface areas. Isotherms and isosteric heats for the groove site and outside surface of heterogeneous bundles are very close

to those for the homogeneous bundles, indicating the effect of heterogeneity has no bearing on external surface adsorption.

Simulations on closed homogeneous and heterogeneous bundles revealed that adsorption capacities for closed homogeneous bundles greatly underpredict the experimental data measured on nanotubes prepared by the electric arc method. For the adsorbates  $\text{CH}_4$  and Xe, the isotherms were about 100 and 10-30 times less than experiments, respectively. The closed heterogeneous bundle also underpredicted the  $\text{CH}_4$  experimental results, but only by about a factor of 2-6. The Xe simulation results matched the experiments well, indicating that closed heterogeneous bundles show proper adsorption capacity behavior.

Low coverage isosteric heat values on homogeneous bundles fail to predict the experimental values. This is true for all three gases examined (Ar,  $\text{CH}_4$ , and Xe). The external surface and groove sites do not provide the high energy binding sites needed to match experimental observations on electric arc generated nanotubes. The closed heterogeneous bundles, however, allow for adsorbates to access the higher energy IC defect sites. It was shown for all gases that closed heterogeneous bundle models have calculated low coverage isosteric heat values that correctly predict the experiments. We also examined the effect of temperature on the isosteric heat. We found that in some cases the isosteric heat qualitatively changes with temperature, which is contrary to the prevailing assumption that  $q_{\text{st}}$  is independent of  $T$ .

We assessed homogeneous and heterogeneous bundles having a fraction of open nanotubes as models for nanotubes produced by the HiPco method. We found that roughly 11% open nanotubes for both the homogeneous and heterogeneous bundles show reasonable agreement with experimental  $q_{\text{st}}$  data for Xe in low to intermediate coverage regions. This fraction of open nanotubes is considerably lower than used in previous models. Agnihotri *et al.*[48] estimated their HiPco nanotube bundle samples to have 45% to 60% open nanotubes. Marand *et al.*[60] have determined a value of 47% open nanotubes to describe their HiPco results. This may be attributed to variations between different samples of HiPco nanotubes.

Finally, the specific surface areas have been computed for Ar,  $\text{CH}_4$ , and Xe adsorption on a variety of different bundle models. We demonstrated that the SSA values for curved adsorbents, such as closed homogeneous bundles and isolated closed nanotubes, depend on

the diameter of the adsorbate. Hence, the assumption that SSA should be independent of the adsorbate size if the same sites are available to all adsorbates is not strictly valid. We find that the spread in the experimentally measured SSA values on HiPco nanotubes is best matched by a partially opened heterogeneous bundle, consistent with the observations for isosteric heats.

### 3.0 ADSORPTION OF NEON IN SINGLE WALLED CARBON NANOTUBE BUNDLES

The content of this chapter is taken from M. R. LaBrosse and J. K. Johnson, “Ideal and Defect Interstitial Channel Availability in Carbon Nanotube Bundles: Comparison of Modeling with Experiments”, *J. Phys. Chem. C*, submitted (2009).

#### 3.1 INTRODUCTION

Nanotubes have been synthesized by a variety of methods, including electric arc, laser ablation, and high pressure carbon monoxide (HiPco).[55] Nanotubes produced by the electric arc method have been shown to have closed ends,[57] while as-produced HiPco nanotubes have been shown to have a percentage of the nanotubes that are open.[58, 59, 48, 60, 61] Recent studies have claimed that the HiPco process can produce nanotubes with carbon purities as high as 97%,[84] making them an attractive choice for adsorption experiments. In this chapter, we compare Ne simulation results with experimental data[35, 84] measured on nanotubes prepared by the HiPco process.

Adsorption studies in the literature show general agreement over the nature of adsorption in internal sites, groove sites, and external surface sites.[64, 65, 41, 66, 21, 34] However, there is substantial disagreement over whether gases adsorb in interstitial channels (ICs) created by three or more nanotubes.[17, 45, 35, 48, 46, 63, 12, 21] Two experimental studies by Migone and coworkers have shown that experimental SSAs for Ne are similar to those for other gases. In the case of nanotubes prepared by the electric arc method, Ne and Xe had SSAs of 41 and 38 m<sup>2</sup>/g, respectively.[17] Adsorption results from experiments using

HiPco nanotubes show a similar trend, namely that all gases have roughly the same SSAs (SSA).[35] The experimental results from these two studies strongly indicate that the same types of sites are available for adsorption on SWNT bundles. Therefore, because Xe is too large to adsorb in ICs created by three nanotubes, it is concluded that none of the gases adsorb interstitially. This is a surprising result, because the diameter of Ne is small enough that it is expected to adsorb in the ICs.

LaBrosse and coworkers have recently compared the SSAs, isosteric heats of adsorption, and adsorption isotherms for Ar, CH<sub>4</sub>, and Xe with experiments.[85] Through simulations on various closed and partially opened homogeneous and heterogeneous bundles, it was shown that defect interstitials found in heterogeneous bundle models are critical for describing experimental results. However, Ar, CH<sub>4</sub>, and Xe are all too large to adsorb in the ideal ICs formed by three nanotubes, so no conclusions were drawn about adsorption in these sites.

Simulations show that Ne is small enough, in principle, to access ideal IC adsorption sites that are unavailable for adsorption of Ar, CH<sub>4</sub>, and Xe. Hence, this chapter aims to make a clear distinction between adsorption in ideal and defect ICs. In doing so, we perform simulations with Ne to examine the role of both ideal and defect interstitials for describing experimental results. As with previous work,[45, 85] we consider models of closed and partially opened homogeneous and heterogeneous SWNT bundles.

## 3.2 METHODOLOGY

### 3.2.1 Bundle construction

The details of constructing the bundles used in simulations were described previously.[85] To summarize, several assumptions were made to circumvent the complexities of a fully described nanotube bundle model. There are no interactions between nanotubes during the adsorption simulations and nanotube positions are held fixed. All nanotubes used in simulations are assumed to be straight, parallel, rigid cylinders free of chemical defects. Flexibility issues, such as thermal vibrations, are not considered, which is a reasonable as-

sumption because previous work has shown that thermal vibrations can be safely ignored for transport properties of gases inside SWNTs at high loadings.[71] Homogeneous bundles are constructed such that tube centers are arranged in a two-dimensional hexagonal lattice configuration. Heterogeneous bundles are generated by optimizing the two-dimensional nanotube centers in energy to a local minimum on the potential energy surface. Nanotube centers are then randomly moved to explore the potential energy surface and locate new, possibly more favorable, local minima. During this process, the lowest energy configuration is stored until it is replaced by one even lower in energy. This technique is called the basin-hopping method.[85, 74, 75, 76] The result is a heterogeneous bundle that has settled into a local or global minimum configuration. After the basin-hopping algorithm was completed, the nearest-neighbor nanotube spacing was checked for consistency. The spacing between nanotubes is very close to 3.2 Å for all neighboring pairs of nanotubes in these bundles.

### 3.2.2 Interaction potentials for classical fluids

The Lennard-Jones (LJ) potential was used to calculate fluid-fluid interactions. The LJ potential is given by

$$V_{\text{LJ}}(r) = 4\epsilon_{\text{ff}} \left[ \left( \frac{\sigma_{\text{ff}}}{r} \right)^{12} - \left( \frac{\sigma_{\text{ff}}}{r} \right)^6 \right], \quad (3.1)$$

where  $r$  is the fluid-fluid separation distance and  $\epsilon_{\text{ff}}$  and  $\sigma_{\text{ff}}$  are the LJ parameters for the adsorbate-adsorbate (fluid-fluid) interactions. For Ne,  $\epsilon_{\text{ff}}/k_{\text{B}}$  and  $\sigma_{\text{ff}}$  are 36.83 K and 2.79 Å, respectively, where  $k_{\text{B}}$  is the Boltzmann constant.

Solid-fluid interactions require additional consideration due to the cylindrical geometry of the nanotubes. We assume that the interaction potential between adsorbates and nanotubes is based on a LJ potential. The derivation of the solid-fluid potential includes one additional assumption; nanotubes are curved sheets of graphite with a carbon atom surface density ( $\theta$ ) of 0.38 Å<sup>-2</sup> for all (n,m) type nanotubes.

We have used the hypergeometric series potential to describe the interaction between an adsorbate and an infinitely long cylinder of radius  $R$ .[36, 86] The hypergeometric potential expresses the interaction between an adsorbate atom/molecule and a nanotube as a function of  $r$ , the distance of the atom or molecule from the center of the nanotube. Different hyper-

geometric expressions are used to describe an adsorbate inside or outside of the nanotube. The potential for a molecule outside the nanotube is

$$V_{\text{LJ}}^{\text{out}}(r, R) = 3\pi\theta\epsilon_{\text{sf}}\sigma_{\text{sf}}R \times \left[ \frac{21}{32} \left( \frac{\sigma_{\text{sf}}}{r} \right)^{11} M_{11/2}(x) - \left( \frac{\sigma_{\text{sf}}}{r} \right)^5 M_{5/2}(x) \right], \quad (3.2)$$

where  $x = R/r$ ,  $\sigma_{\text{sf}}$  and  $\epsilon_{\text{sf}}$  are the solid-fluid LJ parameters, and the elliptical integral,  $M_n(x)$ , is given by[86]

$$M_n(x) = \pi \frac{F[1-n, 1-n; 1; x^2]}{(1-x^2)^{2n-1}}. \quad (3.3)$$

The generic form of the hypergeometric series,  $F$ , is given by

$$F[a, b; c; z] = 1 + \frac{ab}{1! c} z + \frac{a(a+1)b(b+1)}{2! c(c+1)} z^2 + \dots \quad (3.4)$$

Inserting Eq. 3.3 and Eq. 3.4 into Eq. 3.2 yields a potential form describing an adsorbate outside of a nanotube as a function of its distance from the center of the nanotube and the nanotube radius. A similar treatment is applied to the potential describing an adsorbate inside of a nanotube. There are two main advantages to using the hypergeometric potential: (1) correct physical description of the interaction potential at all solid-fluid separations and (2) the ability to easily generate potentials for nanotubes of any diameter. Previous studies by LaBrosse and coworkers used an eighth-order polynomial, fit for a specific  $(n, m)$  nanotube and adsorbate pairing to describe solid-fluid interactions.[85] This approach requires polynomial fits to several adsorbate- $(n, m)$  type nanotube combinations and yielded polynomials that do not give the correct asymptotic behavior as  $r \rightarrow \infty$ .

### 3.2.3 Interaction potentials for quantum fluids

**3.2.3.1 Path-integral formalism** Quantum diffraction effects must be taken into account in order to accurately model Ne at the temperatures of interest in this study. One method of accounting for quantum effects in molecular simulations is path-integral Monte Carlo.[87] The path-integral formalism was first described by Feynman in 1948, who postulated a connection between a classical system and a quantum system through a transformation of the classical particle into a polymeric ring of  $P$  “beads”.[88] In this context, each atom or molecule is replaced by a ring polymer. The potential then contains two parts, the

interactions between beads of different rings (intermolecular) and the interactions between beads on the same ring (intramolecular). The intermolecular potential is given by

$$V^{\text{inter}} = \frac{1}{P} \sum_{\alpha=1}^P \sum_{i < j}^N \phi_{ij}^{\alpha}, \quad (3.5)$$

where  $N$  is the total number of polymer rings in the system, and  $\phi_{ij}^{\alpha}$  is the pairwise potential between bead  $\alpha$  on molecule  $i$  and bead  $\alpha$  on molecule  $j$ . [89] The intramolecular potential is given by

$$V^{\text{intra}} = \frac{Pm}{2(\beta\hbar)^2} \sum_{\alpha=1}^P \sum_{i=1}^N |\vec{r}_i^{\alpha} - \vec{r}_i^{\alpha+1}|^2, \quad (3.6)$$

where  $\vec{r}_i^{\alpha}$  is the position of bead  $\alpha$  on ring  $i$ ,  $m$  is the mass of each bead, and  $\beta$  is equal to  $1/(k_{\text{B}}T)$ . [89]

The path integral (PI) formalism gives an exact description of quantum effects as the number of beads  $P$  approaches infinity. In practice, a relatively small finite number of beads is required to converge the properties to sufficient accuracy for most systems. The number of beads used to describe Ne was chosen by comparing the total energy of a small test system as a function of the number of beads. Convergence of the number of beads for Ne produced a value of  $P = 5$  to adequately describe quantum effects. We use the hybrid Monte Carlo approach [90] to efficiently sample phase space for the PI system. [91] However, it has been shown that the efficiency of hybrid Monte Carlo decays exponentially as the system size increases, [92] making it computationally prohibitive to use for systems containing thousands of atoms.

**3.2.3.2 Feynman-Hibbs method** The Feynman-Hibbs (FH) technique is a computationally efficient approach for approximately describing quantum effects. [93] To lowest order, the FH method employs one simple correction term to the potential energy, making the calculation roughly as fast as classical Monte Carlo. Moreover, the convergence of the FH method does not depend on system size, making it an attractive alternative to PI hybrid Monte Carlo for large systems, such as those studied here. The FH implementation we used in this work is given by

$$V_{\text{FH}}(r) = V_{\text{LJ}}(r) + \frac{\beta\hbar^2}{24m} \left( V_{\text{LJ}}'' \right), \quad (3.7)$$

where  $m$  is the mass of a Ne atom, and  $V_{\text{LJ}}$  is given by Eq. 3.1 and Eq. 3.2 for fluid-fluid and solid-fluid interactions, respectively.  $V_{\text{LJ}}''$  is the second derivative of the LJ potential.

Just as for the classical limit, the quantum solid-fluid potential is described by a hypergeometric series potential. This equation has been derived elsewhere.[94] The potential for adsorption outside of a nanotube is given by

$$V_{\text{FH}}^{\text{out}} = V_{\text{LJ}}^{\text{out}} + \pi\theta\epsilon_{\text{sf}}R \left( \frac{\beta\hbar^2}{8m\sigma_{\text{sf}}} \right) \times \left[ \frac{2541}{32} \left( \frac{\sigma_{\text{sf}}}{r} \right)^{13} M_{13/2}(x) - 25 \left( \frac{\sigma_{\text{sf}}}{r} \right)^7 M_{7/2}(x) \right]. \quad (3.8)$$

The solid-fluid potential for adsorption on the inside of a nanotube is similar and is given by Tanaka and coworkers.[94]

### 3.2.4 Specific surface area

The SSA is a quantitative description of the available surface sites for adsorption. The SSA is calculated from the point-B method, which is the same method used in experiments.[35] This method uses a gas adsorption isotherm to determine the SSA by finding the point on the isotherm that best represents the point of monolayer coverage. The point of monolayer completion is determined by first linearly fitting the higher coverage region of an isotherm. At lower coverage, the point at which the isotherm trends downward and deviates from the linear fit corresponds to monolayer completion.

The amount adsorbed at point-B is used to calculate the SSA from the following equation,

$$\text{SSA} = N_{\text{ads}}\pi \left( \frac{\sigma_{\text{ff}}}{2} \right)^2 \left( \frac{6022}{12N_{\text{c}}} \right), \quad (3.9)$$

where  $N_{\text{ads}}$  is the number of molecules adsorbed at the tangential point,  $\sigma_{\text{ff}}$  is the LJ gas diameter in Å, and  $N_{\text{c}}$  is the number of carbon atoms in the simulation bundle. The numerical values of 12 and 6022 are the molecular weight of carbon and Avogadro's number multiplied by  $10^{-20}$  to convert the units of SSA to  $\text{m}^2/\text{g}$ . This approach is assumed to be independent of the dimensionality and topology of the sorbent.

### 3.2.5 Simulation details

Isotherms, isosteric heats of adsorption, and specific surface areas were computed for Ne using the FH potentials from grand canonical Monte Carlo simulations on closed and partially opened homogeneous and heterogeneous bundles. The height of the simulation box was set to be 10 times the LJ  $\sigma_{\text{ff}}$  parameter to ensure negligible interactions with periodic images. For simulations at very low coverage, which requires very low pressures, the box height was increased such that the number of atoms or molecules adsorbed was large enough to ensure good statistics of calculated properties. The side lengths of the simulation box were chosen to be between 150 and 250 Å, so that interactions with periodic images was negligible. The total number of simulation steps for equilibration and production is on the order of  $10^8$ , with half of the steps used for equilibration.

## 3.3 RESULTS AND DISCUSSION

### 3.3.1 Bundle production

Simulations for Ne were run on three different nanotube bundles. The homogeneous bundle was constructed from 37 (9,9) type nanotubes in a perfect hexagonal array. The heterogeneous bundles used in simulations were constructed from 45 nanotubes, comprised of 10 (8,8), 25 (9,9), 5 (10,10), and 5 (11,11) type nanotubes. The tubes were placed in a simulation box and the structure was minimized in energy until a local minimum structure is obtained, which is the structure labelled Het2 on the right in Figure 2.3. The nanotubes within the bundle were then optimized according to the previously described basin-hopping algorithm for a total of  $10^3$  cycles. The resulting optimized structure is shown in Figure 2.3, labelled Het1. As a consequence of the optimization, Het1 has fewer and smaller IC defects than Het2, as can be seen from inspection of Figure 2.3.

### 3.3.2 Comparison of quantum methods

We have computed adsorption isotherms for Ne on the Het2 bundle at 21.9 K (the same temperature used in experiments by Krungleviciute and coworkers.[35] We have used classical simulations (no quantum effects), path integral hybrid Monte Carlo simulations, and FH simulations and compared these calculations in order to assess quantum effects for this system. The results are plotted in Figure 3.1. It is evident that quantum effects are very important for Ne at 21.9 K. We note that the FH calculations are in good agreement with the PI data, but slightly over-predict the quantum effects. However, this over-prediction is greatly outweighed by the computational efficiency of the FH method, typically resulting in more than an order of magnitude less computation time. Convergence of the PI simulations is very slow, due to the system sizes. For this reason, the FH method was used to account for quantum corrections in the remainder of this chapter.

### 3.3.3 Solid-fluid interactions

Solid-fluid interaction parameters,  $\sigma_{sf}$  and  $\epsilon_{sf}$ , are needed for adsorption simulations. It is very common to use Lorentz-Berthelot (LB) combining rules to obtain the solid-fluid parameters from the pure component values.[95] We have used the parameters developed for graphite by Steele to approximate the potential for carbon in nanotubes:  $\sigma_C = 3.4 \text{ \AA}$  and  $\epsilon_C/k_B = 28 \text{ K}$ .[78] However, previous studies of Ne on graphite have shown that the solid-fluid  $\epsilon$  parameter computed from LB combining rules does not compare well experimental results. Bruch et al. have shown that a significantly smaller empirically derived  $\epsilon$  parameter can provide an accurate description of interactions between Ne and graphite.[96] Both the Lorentz-Berthelot and Bruch et al.  $\epsilon_{sf}$  parameters for Ne are presented in Table 3.1. Also shown are the LJ parameters and adsorption isotherm temperatures for Ar, CH<sub>4</sub>, Xe, and Ne.

The Lorentz-Berthelot and Bruch et al. solid-fluid parameters have been used to predict the first to second layering transition of Ne adsorption on planar graphite. Simulations were performed using a slit pore with adsorption taking place on two square graphite planes. The lateral dimension of each graphite plane was  $100 \times \sigma_{ff}$ , or 279  $\text{\AA}$ , and the width of the slit pore

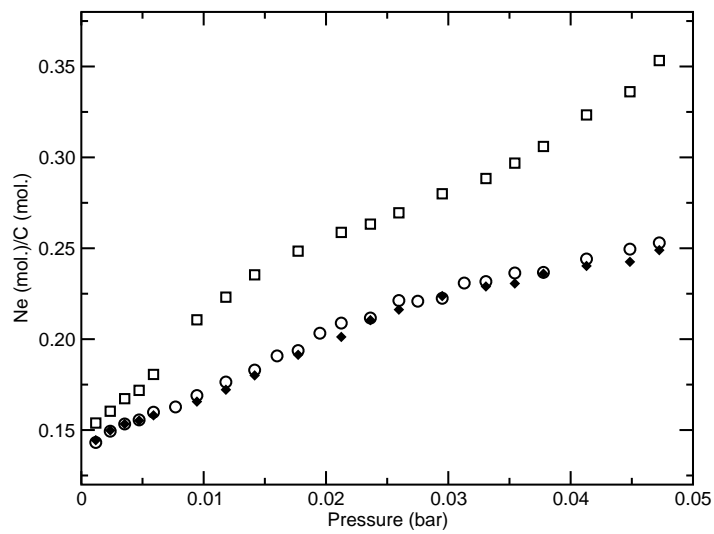


Figure 3.1: Neon adsorption isotherms on a closed 45-tube heterogeneous bundle (Het2 in Figure 2.3) at a temperature of 21.9 K. The open squares are for classical Ne (no quantum effects), the open circles are from path integral calculations, and the filled diamonds are from simulations applying the Feynman-Hibbs corrections.

Table 3.1: Potential parameters used in simulations. Solid-fluid parameters are presented using Lorenz-Berthelot mixing rules ( $\sigma_{\text{sf}}^{\text{LB}}$  and  $\epsilon_{\text{sf}}^{\text{LB}}$ ).[95] We also present the solid-fluid potential well depth for Ne using the empirical estimate from Bruch et al. ( $\epsilon_{\text{sf}}^{\text{Br}}$ ).[96] The fluid triple point ( $T_{\text{tr}}$ ) and simulation temperatures ( $T_{\text{sim}}$ ) used in both the experiments[35] and simulations are presented in the last two rows, respectively.

Parameter	Ar	CH <sub>4</sub>	Xe	Ne
$\sigma_{\text{ff}}$ (Å)	3.42	3.73	4.10	2.79
$\epsilon_{\text{ff}}/k_{\text{B}}$ (K)	124.07	147.90	221.00	36.83
$\sigma_{\text{sf}}^{\text{LB}}$ (Å)	3.410	3.565	3.750	3.095
$\epsilon_{\text{sf}}^{\text{LB}}/k_{\text{B}}$ (K)	58.94	64.35	78.66	32.11
$\epsilon_{\text{sf}}^{\text{Br}}/k_{\text{B}}$ (K)	–	–	–	26.50
$T_{\text{tr}}$ (K)	83.81	90.69	161.40	24.56
$T_{\text{sim}}$ (K)	77.1	77.1	145.0	21.9

was 100 Å, large enough to ignore any effects of the opposing wall. The graphene simulations were performed with the 10-4-3 Steele potential.[97] Simulation data are compared with experimental isotherms from Hanono and coworkers[98] in Figure 3.2. Simulations using the Bruch et al.  $\epsilon_{sf}$  parameter are in much better agreement with experiments at 14 and 17 K than the LB data. Therefore, all simulations for Ne adsorption on SWNT bundles are performed using  $\epsilon_{sf}^{Br}$  in the remainder of this chapter, assuming that the graphene potential is a good approximation to the SWNT potential.

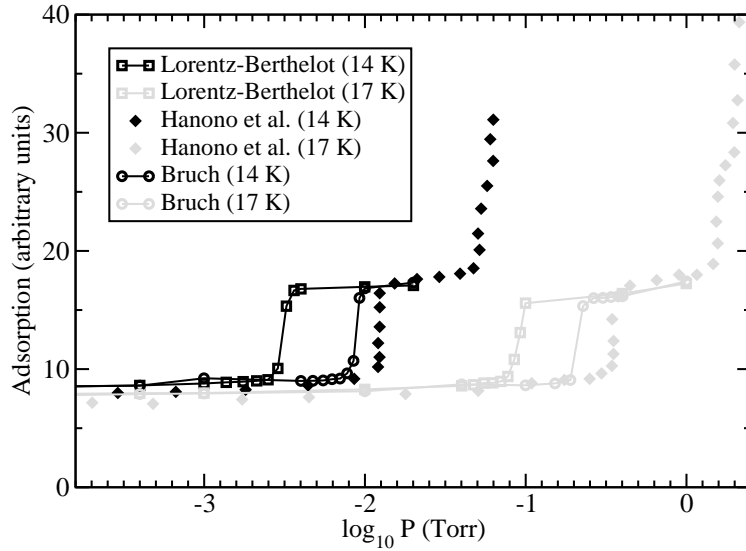


Figure 3.2: First to second layer transition for Ne adsorption on graphite using Bruch et al.[96] and Lorentz-Berthelot[95] solid-fluid parameters. Experimental data are taken from Hanono and coworkers.[98] Isotherms are presented for temperatures of 14 and 17 K (color online). Lines are drawn to guide the eye.

### 3.3.4 Adsorption on graphite

Migone and coworkers[17, 35] have used adsorption isotherms of Ar, CH<sub>4</sub>, Xe, and Ne on SWNTs to conclude that gases do not adsorb in interstitial channels. Their conclusion is

based on the hypothesis that the measured SSA values for different adsorbates will be similar if and only if the same sites are available for adsorption of all gases. Since Ne is theoretically small enough to adsorb in ideal ICs[41] and the other gases are not, then similar values of SSAs for these gases indicate that none of the gases adsorb into ideal ICs. It is rigorously true that adsorption of classical spherical adsorbates on planar surfaces produce the same SSAs. It is not readily apparent that quantum fluids will produce the same SSA as classical fluids on a planar sorbent. To test this hypothesis we have computed adsorption isotherms for Ar, CH<sub>4</sub>, Xe, and Ne on graphite at the experimental temperatures listed in Table 3.1. We calculated the SSA values for each of these adsorbates using Eq. 3.9. As done previously,[85] we define a relative spread for comparing the SSA values of different adsorbates as  $(max - min)/max$ , where  $max$  and  $min$  are the largest and smallest SSA values in the data set, respectively. The SSA values for Ar, CH<sub>4</sub>, Xe, and Ne are 860, 859, 848, and 864 m<sup>2</sup>/g, respectively. The SSA spread for adsorbing these four gases on planar graphite is less than 2%, consistent with assumption that classical and weakly quantum fluids have the same SSAs for planar sorbents.

It is interesting to note that the two-dimensional (2D) radial distribution functions,  $g(r)$ , at monolayer coverage are qualitatively different for these fluids. The monolayer  $g(r)$  data for Ar, CH<sub>4</sub>, Xe, and Ne at the temperatures given in Table 3.1 are plotted in Figure 3.3. From this figure we see that CH<sub>4</sub> and Ne are nearly identical when plotted as a function of reduced distance,  $r/\sigma_{ff}$ . Both fluids appear to be well-ordered, even solid-like, with peaks located at the 2D hcp crystal locations. In contrast, the Ar structure is less ordered, having shoulders where some of the 2D hcp peaks should be, and the Xe  $g(r)$  is liquid-like. These differences in 2D structure can be attributed to differences in the reduced temperatures,  $Tk_B/\epsilon_{ff}$ , which are 0.68, 0.61, 0.73, and 0.67, for Ar, CH<sub>4</sub>, Xe, and Ne, respectively. Hence, CH<sub>4</sub> and Ne have the lowest reduced temperatures and the highest order. Ar has the next lowest reduced temperature, just slightly higher than Ne, and is less ordered, but still solid-like. Xe has the highest reduced temperature and is therefore liquid-like. This is also consistent with Xe having the lowest SSA, however, the liquid-like structure of Xe is not sufficient to greatly affect the SSA spread. Note that Ar and Ne have very similar reduced temperatures but fairly different structures. Moreover, quantum effects for Ne should induce more liquid-like

behavior than the other fluids. In this light, the solid-like structure for Ne seen in Figure 3.3 is unexpected. This point will be addressed in Section 3.3.7.

The above analysis indicates that any differences in the SSA spread for nanotube bundles that have the same sites available for adsorption, e.g., a closed homogeneous nanotube bundle with blocked ICs, must be due to failure of the hypothesis that the SSA for different adsorbates will be the same if the sorbent has the same sites available for adsorption for all gases.

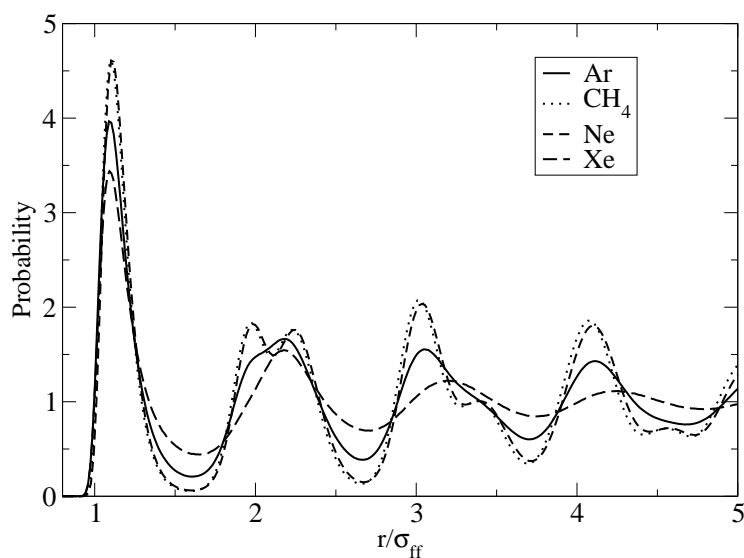


Figure 3.3: Two-dimensional  $g(r)$  probability plots for Ar, CH<sub>4</sub>, Xe, and Ne on planar graphite. The  $g(r)$  analysis was performed at monolayer coverage and the temperatures given in Table 3.1.

### 3.3.5 Defect interstitial adsorption

When nanotubes of the same diameter pack in a 2D hexagonal array, as is the case for homogeneous bundles, the space between three nanotubes is defined as an ideal IC. Defect ICs arise when tubes of different diameters pack together, creating large defect volumes within the

bundle. As can be seen in Figure 2.3, these defect ICs are created by four or more nanotubes. Previous adsorption studies for the classical fluids Ar, CH<sub>4</sub>, and Xe showed the importance of defect interstitial adsorption, thus pointing to heterogeneous bundles as a better model for nanotube bundles produced from the HiPco method.[85] Moreover, it is found that models with ~11% open nanotubes are in even better agreement with experimental SSA values than their closed counterparts.[85] In this section we integrate the adsorption results from the classically behaved fluids with those of Ne, a quantum fluid at the temperatures and pressures of interest, and more importantly having a diameter small enough to allow it to adsorb into the ideal ICs, whereas the other gases tested are too large to adsorb in ideal ICs.

Previous adsorption studies for Ar, CH<sub>4</sub>, and Xe showed that heterogeneous bundles with approximately ~11% open nanotubes gave the best agreement with experimental data for the isosteric heat of adsorption,  $q_{st}$ . [85] Figure 3.4 shows the simulation results for  $q_{st}$  on the two heterogeneous bundles (Het1 and Het2) in Figure 2.3. Also shown are experimental data from Ramachandran and coworkers[84] and unpublished data from Krungleviciute and coworkers.[99] The experimental data were calculated from several isotherms using the following equation,

$$q_{st} = -k_B \left( \frac{\partial \ln P}{\partial (1/T)} \right)_N, \quad (3.10)$$

where  $P$  is the pressure of a point on each isotherm at constant coverage  $N$ . There is generally good agreement with the experiments in the range of intermediate coverage, which corresponds to the filling of the large defect ICs. These bundles also capture the  $q_{st}$  value at very low coverage, corresponding to adsorption on high-energy binding sites found inside opened nanotubes and some groove sites on the outer surface. However, the decrease in isosteric heat is gradual for the heterogeneous bundles in the coverage region between about 0.02-0.06. This can be attributed to complete filling of the opened nanotubes and ideal ICs. The partially opened homogeneous bundle results, however, systematically over-predict the experimental results over the entire range of Ne coverage.

In the previous section, it is shown that planar graphite produced a low SSA spread consistent with Ar, CH<sub>4</sub>, Xe, and Ne accessing the same sites for adsorption. Ne simulations were performed on various nanotube bundle systems at experimental temperatures to compare with previous work on classical fluids. Table 3.2 shows the SSA values and spreads

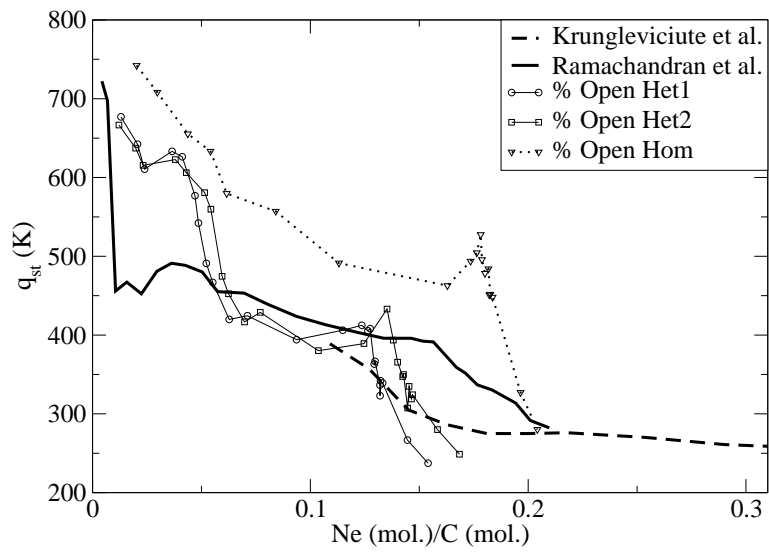


Figure 3.4: Isosteric heats of adsorption for Ne on partially opened SWNT bundle systems. Experimental data on HiPco SWNT bundles is taken from Ramachandran and coworkers (solid line)[84] and Krungleviciute and coworkers (dashed line)[99].

for all simulations. It is clear that adding the Ne results has significantly increased the SSA spreads for all cases. This can be attributed to adsorption of Ne in the ideal interstitial sites. Simulation snapshots confirm that of the four gases, only Ne adsorbs in the ideal ICs for all of the investigated nanotube bundle systems. The effect of ideal interstitial adsorption will be discussed in greater detail in the next section.

Table 3.2: Specific surface areas for Ar, CH<sub>4</sub>, Ne, and Xe adsorption on closed and partially opened ( $\sim 11\%$ ) homogeneous and heterogeneous bundles. The homogeneous bundle, referred to as Hom, is comprised of 37 (9,9) type nanotubes. The heterogeneous bundles, referred to as Het1 and Het2, are shown in Figure 2.3. Experimental results[35] are shown for comparison.

System		Ar	CH <sub>4</sub>	Xe	Ne	Spread
	Hom	220	238	187	511	0.63
Closed	Het1	265	285	251	351	0.28
	Het2	314	330	294	395	0.26
	Hom	263	296	234	560	0.58
% Open	Het1	299	318	300	406	0.26
	Het2	357	361	343	449	0.24
Experiment		324	337	328	318	0.06

Examining the SSA spreads listed in Table 3.2, both the closed and partially opened bundle results show that the homogeneous bundle drastically over-predicts the experimental SSA spread. The heterogeneous bundle simulations are not in good agreement with experiments, but the availability of the defect interstitials lowers the SSA spreads by about a factor of two when compared with the homogeneous simulations, consistent with the previous findings that defect interstitials are important for explaining experimental adsorption results.[45, 85]

### 3.3.6 Ideal interstitial adsorption

It is clear from Table 3.2 that adsorption of Ne in all systems is too high, which leads to elevated SSA spreads. We here explore the effect of blocking Ne adsorption in the ideal ICs, while allowing adsorption in defect ICs. We have carried out simulations of Ne adsorption on all the bundle models discussed previously, but with all ideal ICs blocked. The resulting SSAs and their spreads are presented in Table 3.3, along with the data for Ar, CH<sub>4</sub>, and Xe from Table 3.2.

Table 3.3: Specific surface areas for Ar, CH<sub>4</sub>, Ne, and Xe adsorption on closed and partially opened ( $\sim 11\%$ ) homogeneous and heterogeneous bundles having blocked ideal interstitial channels. Experimental results[35] are shown for comparison.

System		Ar	CH <sub>4</sub>	Xe	Ne	Spread
Closed	Hom	220	238	187	246	0.24
	Het1	265	285	251	283	0.12
	Het2	314	330	294	341	0.14
% Open	Hom	263	296	234	296	0.21
	Het1	299	318	300	337	0.11
	Het2	357	361	343	395	0.13
Experiment		324	337	328	318	0.06

Blocking the ideal interstitials leads to a dramatic reduction in the SSA values for Ne and the SSA spreads for all systems. This likewise supports the experimental claim that gases do not adsorb in ideal ICs.[17, 35] In both the closed and partially opened cases, the heterogeneous bundles have much lower spreads than the homogeneous bundles, indicating the importance of defect interstitial to describe experimental results. Previous simulation results for classical fluids concluded that partially opened heterogeneous bundles served as the best model for HiPco nanotubes.[85] The results in Table 3.3 are in agreement with that conclusion. However, the SSA spreads for closed heterogeneous bundles are very similar to those for partially opened heterogeneous bundles, making it impossible to identify which

model (closed or partially opened) is in better agreement with experiments when Ne is included.

It is important to note that the closed homogeneous nanotube bundle with blocked interstitials presented in Table 3.3 has an SSA spread of 0.24, which is four times larger than the experimental SSA spread and twice as large as the heterogeneous bundles. This is the most critical result when comparing with experimental results. Recall the hypothesis in the experiments is that the SSA for different adsorbates will be the same if the adsorbent has the same sites available for adsorption for all gases. We have shown that this is true for the simple case of planar graphite, which produced a very low SSA spread of 0.02. However, the closed homogeneous bundle with blocked ideal interstitial channels has exactly the same sites available for adsorption for all fluids studied here, but gave an SSA spread an order of magnitude higher than planar graphite and four times larger than experiment. This violates the above hypothesis. We see that a low SSA spread for these fluids results from having both blocked ideal ICs and opened defect ICs.

We next examine the isosteric heat of adsorption for closed and partially opened bundles with blocked ideal ICs in an attempt to identify which model best describes the experimental results. Simulation results for  $q_{st}$  are plotted in Figure 3.5 for Ne on nanotube bundles having blocked ICs. Comparing the results with Figure 3.4, it is evident that blocking the ideal interstitials and closing nanotubes shift the simulation data sets to the left, leading to better agreement with experiments at lower coverage. The sharp decrease at very low coverage seen in experiments is predicted well by the closed homogeneous bundle, but this model fails to reproduce  $q_{st}$  at intermediate coverage, between 0.05 – 0.20. The closed and partially opened heterogeneous bundles capture this behavior at intermediate coverage better than the homogeneous bundle. Simulation snapshots confirm that the intermediate coverage region corresponds to the filling of defect interstitials.

The effect of partially opening nanotubes in a bundle on the isosteric heat can be seen in Figure 3.5. Both the closed and partially opened results are shown for a heterogeneous bundle, Het2 in Figure 2.3. The closed nanotubes retain the same qualitative shape as the partially opened nanotubes, but the data are shifted to the left due to the lower amount adsorbed. This leads to better agreement with experiments at lower coverage, but worse

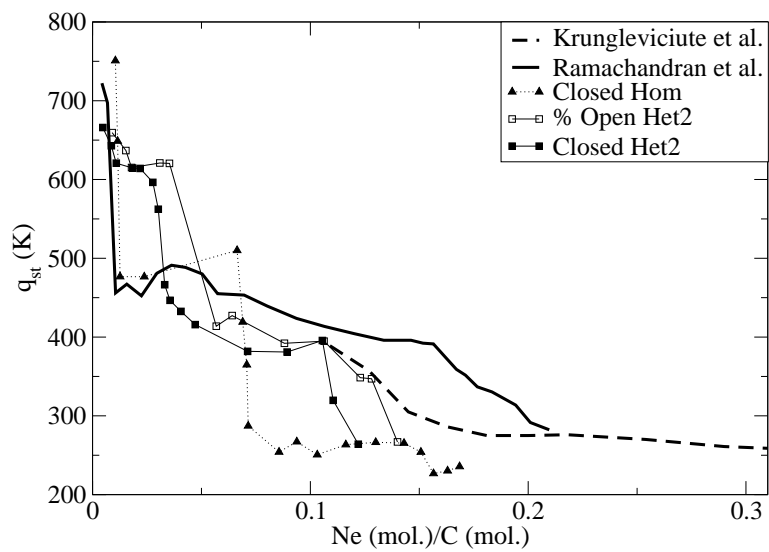


Figure 3.5: Isosteric heats of adsorption for Ne on various SWNT bundles with blocked ideal ICs. Experimental data on HiPco SWNT bundles were taken from Ramachandran et al. (solid line)[84] and Krungleviciute et al. (dashed line)[99].

agreement at intermediate coverage. Hence, examination of  $q_{st}$  cannot be used to identify which model best fits the data for HiPco nanotubes.

We here examine adsorption isotherms for Ne in an attempt to identify whether a closed or opened heterogeneous bundle is the best model for HiPco SWNTs. The adsorption isotherms at a temperature of 21.9 K have been calculated for all the systems listed in Table 3.2 and Table 3.3. For clarity, only a few of these isotherms are plotted in Figure 3.6. Also shown are experimental results from Ramachandran et al.[84] and Krungleviciute et al.[99] at temperatures of 19.2 K and 21.9 K, respectively. We note that the two experimental adsorption isotherms for Ne on HiPco nanotubes are not in good agreement, differing by about 30% at monolayer completion. The difference is unlikely to be caused by the difference in temperatures because simulated adsorption isotherms for Ne ranging from 20-24 K have shown a negligible effect on monolayer coverage. A possible explanation for this discrepancy may be due to inherent differences in the samples. The fact that the samples have rather different reported purities, 97% for Ramachandran and coworkers[84] and 75% for Krungleviciute et al.,[99] supports this explanation. In Figure 3.6, the sample purities have been taken in to consideration when calculating the carbon mass in the sample. However, the presence of impurities may be a factor in hindering adsorption and thus reducing adsorption capacities.

The first thing to notice in Figure 3.6 is that the homogeneous bundle with blocked interstitials fails to predict either of the experimental adsorption isotherms. Combined with the discussion from Table 3.3 and Figure 3.5, we see that this model is not suitable for describing experimental results on HiPco nanotubes by any of the metrics we have used.

We see from Figure 3.6 that adsorption isotherms on the Het2 bundle having closed and partially opened nanotubes, but with blocked ideal ICs are bracketed by the experimental isotherms. Hence, none of the metrics can definitively identify if closed or partially opened heterogeneous bundles is the best model for HiPco nanotubes based on the Ne experimental results.

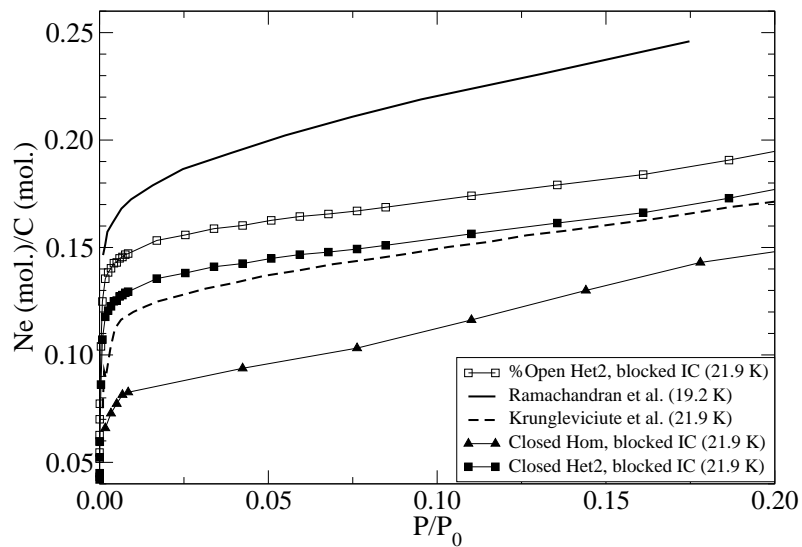


Figure 3.6: Ne adsorption isotherms for closed and partially opened heterogeneous bundles (Het2 from Figure 2.3) with and without blocked ideal interstitials and a 37 nanotube homogeneous (9,9) bundle with blocked ideal ICs. Also shown are two experimental isotherms on HiPco SWNT bundles from Ramachandran et al. (solid line)[84] and Krungleviciute et al. (dashed line)[99].

### 3.3.7 Effect of Ne-graphene binding

The solid-fluid interactions for Ne on a graphene structure, whether it is planar graphite or nanotubes, is qualitatively different than for the other fluids studied here. Figure 3.7 shows the classical solid-fluid interaction potentials for a single (10,10) type carbon nanotube with Ar, CH<sub>4</sub>, Xe, and Ne. Figure 3.7 also shows the Ne solid-fluid potential with applied Feynman-Hibbs quantum corrections for a temperature of 21.9 K. In all cases, the potential has been reduced by the adsorbate well-depth,  $\epsilon_{\text{ff}}$ .

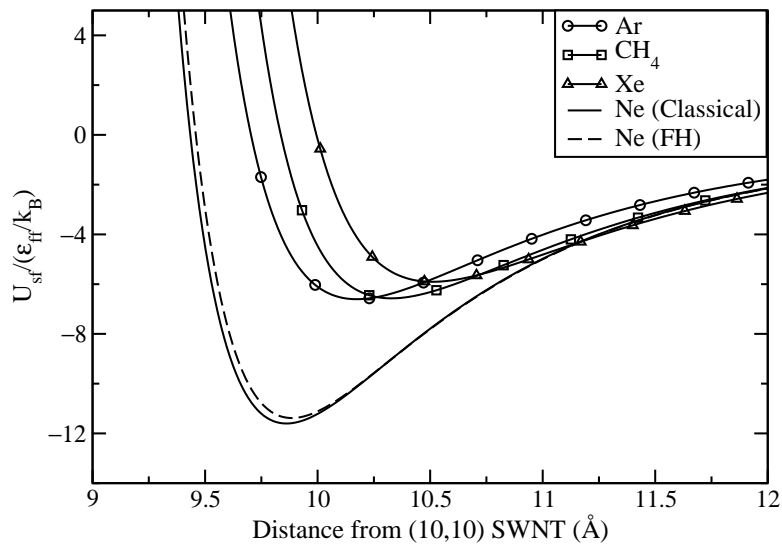


Figure 3.7: Solid-fluid potential curves for Ar, CH<sub>4</sub>, Xe, and Ne with a single (10,10) SWNT reduced by  $\epsilon_{\text{ff}}$ . Distance is measured from the center of the nanotube. The Feynman-Hibbs quantum correction to Ne is for a temperature of 21.9 K.

The magnitude of the reduced solid-fluid potential for Ne is larger than the other fluids. Kim and coworkers observed a similar trend for H<sub>2</sub> adsorption in graphene slit pores.[100] This is consistent with the Ne SSA results observed in Table 3.3. When the ideal interstitial sites are blocked, the same sites are available to all four gases for adsorption. Nevertheless, in all cases, Ne has the highest or very nearly the highest SSA values. Interestingly, this

is not what is found experimentally, where Ne is reported to have the lowest SSA value in comparison with other adsorbates.[17, 35] The simulation results can be explained by considering the nature of adsorption on the nanotubes. The relative strength of the reduced solid-fluid Ne potential to the fluid-fluid potential, coupled with its smaller diameter, allows Ne to penetrate deeper into groove sites present on the outer surface. This is the main reason that the closed homogeneous bundle with blocked ideal ICs is such a poor model for the experimental HiPco system. Although the same sites are available for adsorption of all gases in this model, Ne adsorbs more strongly relative to its fluid-fluid potential and also has a smaller diameter, giving it a much higher SSA than the other gases.

It is not clear why the experiments fail to observe larger SSA values for Ne than the other gases. It may be due to difficulty with temperature control at the lower temperatures required for the Ne adsorption experiments, or perhaps differences in the nanotube samples used for each of the adsorption experiments for the different gases. Errors in the potentials used in the simulations may also contribute to the differences between the experiments and simulations. However, rather unphysically large changes in  $\epsilon_{sf}$  and  $\sigma_{sf}$  would be required to change the results so that Ne had the smallest SSA in simulations.

The larger  $\epsilon_{sf}$  relative to  $\epsilon_{ff}$  for Ne also gives rise to the more ordered 2D structure at monolayer coverage seen in Figure 3.3, in spite of quantum effects and a value of  $Tk_B/\epsilon_{ff}$  that should be high enough to give somewhat liquid-like behavior, as discussed in Section 3.3.4.

### 3.4 CONCLUSION

We report simulation results on several nanotube bundle systems to best determine an appropriate model for experimental adsorption of gases on nanotubes produced by the HiPco process. We used the specific surface area, isosteric heat of adsorption, and adsorption isotherms as metrics to compare with experimental results. Simulations on graphite confirm that the same types of available adsorption sites yield similar SSA values for planar adsorbents, even when Ne (a quantum fluid) is included, and a low SSA spread. However, adsorption SSAs calculated on closed homogeneous bundles with blocked interstitials have a

large spread of 0.24. In both cases, exactly the same sites are available for adsorption, but the SSA spreads are different by an order of magnitude. This result demonstrates that the hypothesis that a complex adsorbent with the same surface sites available for adsorption will yield the same SSAs for different adsorbates is not always correct.

The effect of heterogeneity has been explored for Ne and compared along side results from classical fluids. The isosteric heat of adsorption, adsorption isotherm, and SSA results all point to heterogeneous bundles as being a better model for experimental results than homogeneous bundles. This is consistent with previous simulation work showing that defect interstitials are crucial to modeling experimental results.[45, 85]

We investigated the role of ideal ICs in Ne adsorption. We found that the SSA spreads and isosteric heats of adsorption are in better agreement with experiments when the ideal interstitials are blocked from adsorption. We note that this does not violate previous simulation results of Ar, CH<sub>4</sub>, and Xe adsorption in nanotube bundles because these gases are too large to adsorb in the ideal interstitials. Despite the fact the simulations show that Ne is small enough to enter these ideal interstitials, careful comparison with experiments, most prominently the SSA spreads, show that heterogeneous bundles with a fraction of open nanotubes and closed ideal interstitials are in best agreement with experiments. Our results confirm earlier experimental claims that gases do not adsorb in the ideal ICs of nanotube bundles.[17, 35] However, our simulations lend no explanation as to why these ideal interstitials are inaccessible for adsorption. We estimate that an increase in the solid-fluid LJ parameter of approximately 6% would be needed to prevent Ne from adsorbing in the ideal ICs created by (9,9) nanotubes. We feel that such a large increase in  $\sigma_{sf}$  is unlikely. Hence, we conclude that the ideal ICs must be physically blocked.

## 4.0 TUNGSTEN AND VACANCY DIFFUSION IN FCC COBALT

The content of this chapter is taken from M. R. LaBrosse, L. Chen, and J. K. Johnson, “First Principles Study of Vacancy and Tungsten Diffusion in fcc Cobalt”, *Model. Sim. Mater. Sci. Eng.*, in press (2009).

### 4.1 INTRODUCTION

Cobalt-based alloys are known to have greater high temperature strength than the conventional superalloys.[101] Moreover, experimental work has shown that microwave sintered materials such as tungsten carbide/cobalt possess much higher strength and corrosion resistance than thermal and pressure treated materials having the same nominal composition.[102, 103, 104] Thermal sintering of WC/Co parts requires long sintering cycles and results in unwanted grain growth. In contrast, microwave sintering of WC/Co green parts takes place in a short amount of time with very little grain growth.[103, 104] It has also been observed that the composition of the Co phase is strikingly different between thermally and microwave processed materials. The thermally processed materials have Co binder containing about 20 wt% W, which is the eutectic compositions of the Co/W melt at about 1200°C.[105] In contrast, microwave processed WC/Co materials have Co phases containing virtually no W. Experimental studies on conventional sintering indicate that the composition of the cobalt binder may change significantly during cooling.[105] Therefore, the diffusion of W atoms in the Co binder phase plays a vital role in the sintering process and in determining the physical and chemical properties of the final product. An atomistic understanding of

diffusion of W in Co is therefore a first step toward understanding processes in thermal and microwave sintering of WC/Co materials.

Density functional theory has been extensively used to accurately predict defect formation energies and migration barrier energies, which are of particular importance in vacancy-mediated diffusion in solids.[106, 107, 108] Vacancy-mediated diffusion in solids has been studied using kinetic Monte Carlo[109] and DFT methods.[110, 111, 106, 112] Mantina and co-workers recently described a method for calculating vacancy-mediated self-diffusion coefficients, including both energetic and entropic terms, from first principles.[113] To the best of our knowledge, there are no DFT studies dealing with diffusion in Co. The goal of this chapter is to provide atomic-level examination of vacancy diffusion (Co self-diffusion) and impurity (W) diffusion mechanisms in Co.

## 4.2 COMPUTATIONAL METHODS

In this work, DFT calculations were performed using the spin polarized Perdew-Wang (PW91)[114] generalized gradient approximation as implemented within VASP.[115, 116, 117, 118] The magnetization was checked during and after each calculation to verify ferromagnetic ordering was preserved. We used an energy cutoff of 236.47 eV. The electron-ion interactions were described with ultrasoft pseudopotentials.[119, 120, 121] For fcc cobalt, ultrasoft pseudopotentials were in better agreement than the projector augmented wave pseudopotentials for a number of bulk properties, including the fcc lattice constant, cohesive energy, bulk modulus, and the magnetic moment. Calculations were carried out on a cubic supercell approximately 1.06 nm on a side and nominally containing 108 atoms. The Brillouin zone was sampled within a  $3\times 3\times 3$  Monkhorst-Pack mesh.[122] This corresponds to a reciprocal spacing of about  $0.03 \text{ \AA}^{-1}$ . Tests with smaller values of reciprocal spacing (larger k-points grid) give essentially the same energies. The DFT calculations were performed on fcc Co, the stable crystal phase above 690 K. This phase is relevant to the temperatures in thermal and microwave sintering processes. We have carried out calculations on bulk W in order to compute substitution energies of W in Co. The bulk W phase was taken to be bcc.

The calculated lattice constants for bulk Co and W are 3.54 and 3.18 Å, which agree very well with the experimental values of 3.54[123] and 3.16 Å,[124] respectively. The nudged elastic band (NEB) and climbing-image nudged elastic band (cNEB) methods of Jónsson and co-workers[125, 126] were used to compute the minimum energy diffusion pathways.

Mantina and co-workers have shown that applying surface intrinsic error corrections is critical to achieving good agreement between experimental and calculated Al vacancy formation energies and diffusion coefficients.[113] When an atom is removed from the bulk, resulting in a vacancy defect, a small amount of internal surface is also created. It has been shown that exchange correlation energies from DFT underestimate the vacancy formation energy due to the surface intrinsic energy.[127] This short-coming is attributed to the fact that exchange correlation functionals were developed for bulk systems, leading to a failure to capture the Kohn-Sham wave function evanescence observed at surfaces.[128] Mattsson and Mattsson have shown good agreement between corrected DFT vacancy formation energies and experimental values for Pt, Pd, and Mo.[129] The value of the surface intrinsic error depends on the jellium density and the effective radius,  $R_{\text{eff}}$ , of the hole created in the jellium. The corrected vacancy formation energy,  $E_f^{\text{corr}}$ , is given by

$$E_f^{\text{corr}} = E_f + A\Delta\sigma, \quad (4.1)$$

where  $E_f$  is the uncorrected vacancy formation energy,  $A$  is the internal surface area, defined in terms of the effective radius,

$$A = 4\pi R_{\text{eff}}^2, \quad (4.2)$$

and  $\Delta\sigma$  is the surface intrinsic error. Values for  $\Delta\sigma$  have been obtained using an algorithm from Mattsson and co-workers.[130, 131]

To obtain corrections for Pt, Pd, and Mo, Mattsson and Mattsson scaled the effective radius of the jellium hole in Al by the respective lattice constants of the elements. If we apply this method to Co, we obtain a value of 1.05 Å for the effective radius. However, recent studies by A. Mattsson and co-workers on interstitial Si have shown the internal surface area ( $A$ ), and hence  $R_{\text{eff}}$ , can be solved for directly from a system of equations.[132] We follow their approach in this work.

For the Co jellium density, the ratio of  $\Delta\sigma$  values for different functionals is 0.30:0.76:1.00 for LDA:PBE:PW91. LDA and PBE refer to local density approximation[133] and Perdew-Burke-Ernzerhof[114] functionals, respectively. It should be noted that the PW91 is used for all calculations in this chapter. However, mono-vacancy formation energies using the LDA and PBE functionals were used to calculate  $A$ . As outlined by Mattsson et al.,[132] we start by using the relationships between the surface error of the different functionals.

$$\Delta\sigma^{\text{LDA}} = 0.30\Delta\sigma^{\text{PW91}} \quad (4.3)$$

$$\Delta\sigma^{\text{PBE}} = 0.76\Delta\sigma^{\text{PW91}} \quad (4.4)$$

We next assume that the surface intrinsic error is the dominant error and therefore the corrected vacancy formation energy for each functional will be equivalent. From this, we can substitute the relationships in Eqns. (4.3) and (4.4) in to Eq. (4.1) to obtain an over-specified system of equations given by Eqns. (4.5)–(4.7). From these equations, the two unknowns ( $E_f^{\text{corr}}$  and  $A$ ) are solved for using linear regression.

$$E_f^{\text{corr}} = E_f^{\text{PW91}} + A\Delta\sigma^{\text{PW91}} \quad (4.5)$$

$$E_f^{\text{corr}} = E_f^{\text{PBE}} + 0.76A\Delta\sigma^{\text{PW91}} \quad (4.6)$$

$$E_f^{\text{corr}} = E_f^{\text{LDA}} + 0.30A\Delta\sigma^{\text{PW91}} \quad (4.7)$$

### 4.3 RESULTS

We have calculated vacancy formation energies in bulk cobalt starting from a 108 atom supercell. Defects consisting of one to six adjacent vacancies were generated by placing vacancies in tightly packed configurations. The defective structures were fully relaxed until the forces converged to 0.05 eV/Å. The formation energy for  $i$  vacancies is defined as

$$E_{f,i} = E_{(n-i)\text{Co}} - \frac{(n-i)}{n} E_{n\text{Co}}, \quad (4.8)$$

where  $E_{(n-i)\text{Co}}$  is the energy of cobalt with  $i$  vacancies,  $\frac{(n-i)}{n} E_{n\text{Co}}$  is the energy of  $(n-i)$  bulk cobalt atoms, and  $n = 108$  in this study. The uncorrected formation energy for a

single vacancy, corresponding to about the 1% defect concentration level, was found to be 1.71 eV; the formation energy for two adjacent point defects was 3.30 eV. There are limited experimental data for cobalt with which to compare. Matter et al. obtained a value of  $1.34 \pm 0.07$  eV for the mono-vacancy formation energy of cobalt found from positron annihilation, calculated from data spanning a temperature range of about 500-1000 K.[134] This is substantially lower than the value predicted by DFT. In regards to the validity of this value, the range of experimental data can be quite large, so it is difficult to draw conclusions from a single point. Mattsson and Mattsson noted that the range of Mo experimental vacancy formation energies is 2 eV.[129]

The above vacancy formation energy values have not been corrected by the surface intrinsic error mentioned previously. Cobalt has a jellium density of  $0.814 \text{ \AA}^{-3}$ . When this value is entered into the web-based calculator,[131]  $\Delta\sigma = 0.0454 \text{ eV/\AA}^2$ . Using linear regression on Eqns. (4.5)–(4.7), shown in Table 4.1, a value of  $13.83 \text{ \AA}^2$  is obtained for the internal surface area, giving an intrinsic error correction of 0.63 eV for each vacancy. The value of  $R_{\text{eff}}$  obtained from Eq. (4.2) is  $1.05 \text{ \AA}$ . Interestingly, this is the same value obtained from simply scaling  $R_{\text{eff}}$  for Al ( $1.2 \text{ \AA}$ )[129] by the ratio of the lattice constants of Co to Al, previously done by Mattsson and Mattsson.[129] It is important to note that the effective diameter of the jellium hole ( $2.10 \text{ \AA}$ ) is smaller than the interatomic distance of Co in the bulk ( $2.50 \text{ \AA}$ ), meaning there are no overlap effects for multiple vacancies. Hence, the corrected mono- and di-vacancy formation energies become 2.34 and 4.56 eV, respectively.

Contrary to previous work,[127, 129] applying the surface intrinsic error correction to the mono-vacancy formation energy leads to worse agreement with experiment. This may indicate a short-coming in the correction methodology. The error correction has been developed for non-spin polarized metals (Al, Pt, Pd, and Mo). There is no apparent reason this correction can not be applied to magnetic materials. However, our calculations for Co,  $\alpha$ -Fe, and Ni indicate that the corrected  $E_f$  values for magnetic materials are all over-predicted (see Table 4.2).

Beyond the surface intrinsic error, it is reasonable to assume there may be other contributions to the over-prediction of  $E_f$ , like the choice of pseudopotential, for instance. Kresse and co-workers describe in detail the development of ultrasoft and projector augmented-wave

Table 4.1: Calculated and corrected vacancy formation energy results from different exchange-correlation functionals. Ultrasoft pseudopotentials were used in each case. The corrected values were computed from Eqns. (4.5)–(4.7) using a value of  $A = 13.83 \text{ \AA}^2$ . All energies have units of eV.

Functional	$E_f$	$E_f^{\text{corr}}$
PW91	1.71	2.34
PBE	1.84	2.32
LDA	2.15	2.34

(PAW) pseudopotentials for magnetic materials: Co, Fe, and Ni.[137, 138] However, there are no results or discussion indicating their performance in describing defect behavior. DFT calculations were performed using PAW pseudopotentials to obtain values of  $E_f$  for each of the metals (not shown). The difference was less than 0.1 eV for each metal, lending no change to any discussion points regarding the surface intrinsic error.

The values of the corrected vacancy formation energy per vacancy (VFEPV) for one to six adjacent (coalesced) vacancies are plotted in Figure 4.1. The VFEPV decreases as the number of vacancies grows. Hence, there is an energetic advantage for multiple vacancies to coalesce, indicating that it is very likely that vacancies in Co will tend to condense to form voids under the right conditions. This result is in qualitative agreement with experimental observations that Co nanocrystals can be used to form hollow cobalt oxide or sulfide nanoparticles by the outward diffusion of Co atoms and the inward diffusion of vacancies at relatively low temperatures.[139] We note, however, that the thermodynamic driving force in this process is not vacancy coalescence, but Co oxide or sulfide formation.

We have computed the interaction energy between a pair of vacancies and have plotted the energy as a function of distance between vacancies in Figure 4.2. We see that the vacancy-vacancy interaction beyond the third nearest neighbor is within 1% of the formation energy of a pair of vacancies at infinite separation (twice the energy of a single vacancy). The

Table 4.2: Summary of uncorrected, corrected, and experimental mono-vacancy formation energies for spin-polarized DFT calculations of Co,  $\alpha$ -Fe, and Ni. All energies have units of eV.

	$E_f$	$E_f^{\text{corr}}$	$E_f^{\text{exp}}$
fcc Co	1.71	2.34	1.34 <sup>a</sup>
bcc Fe	1.80	2.15	1.40-2.00 <sup>b</sup>
fcc Ni	1.31	2.00	1.54-1.80 <sup>c</sup>

<sup>a</sup> Matter et al.[134]

<sup>b</sup> de Schepper et al.[135]

<sup>c</sup> Wolff et al.[136]

di-vacancy formation energy shows a slight oscillatory behavior as a function of separation distance. The origin of the oscillations is unclear, but we have ruled out several potential causes. The oscillations are not an artifact of the pseudopotential used because the same phenomenon is observed when using the projector augmented wave method.[140, 138] We have investigated the various convergence criteria in the DFT calculations. Increasing the energy cutoff to 354.7 eV, tightening the force convergence criteria to 0.01 eV/Å, and decreasing the width of the partial occupancy smearing all show minor quantitative changes to the di-vacancy formation energies, but not qualitative changes in the oscillations observed in Figure 4.2. Non-spin polarized calculations on the di-vacancy configurations gave substantial changes in the total energies, but did not affect the oscillations. Finally, density of states calculations were performed on the optimized di-vacancy geometries in an effort to relate the energy differences to shifts in the d-band centers for both spin-up and spin-down. However, the d-band center energies are all within 0.006 eV of each other (average  $E_{\text{dbc}} = -1.718 \pm 0.003$  eV), and differences do not follow the trend of the oscillations observed in Figure 4.2. One possible cause for the small oscillations may be artificial strain from interactions arising from periodic boundary conditions.[141] This effect can be inves-

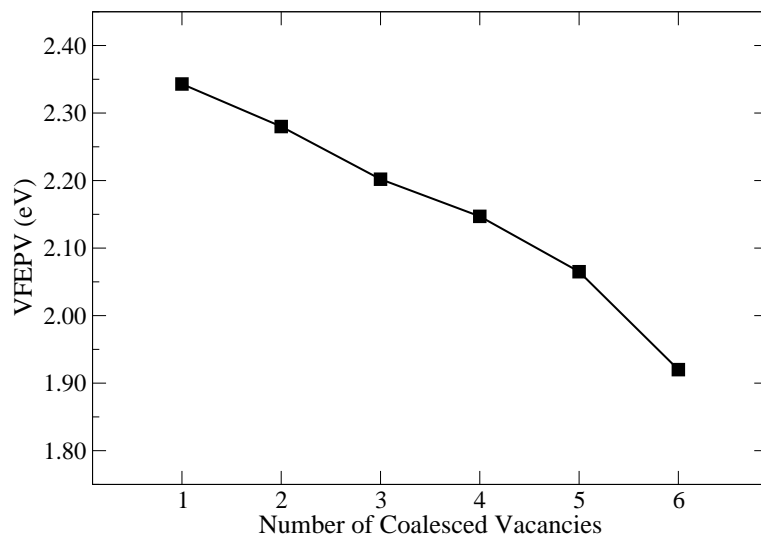


Figure 4.1: Vacancy formation energy per vacancy (VFEPV) for 1 to 6 coalesced vacancies. Surface intrinsic error corrections have been applied. The line is drawn to guide the eye.

tigated by extrapolation to infinite system size for a fixed symmetry.[141] Given the size of the di-vacancy systems in our study, extrapolation to larger, symmetry equivalent systems is computationally prohibitive at this time.

We next investigated the diffusion pathway of single and double vacancy defects in cobalt. We used eight linearly interpolated images along the reaction path in addition to the pre-optimized initial and final points in each cNEB calculation. The calculated activation barrier energy for single vacancy diffusion is 0.98 eV. We have also calculated the mono-vacancy diffusion barrier for paramagnetic Co. The barrier height is 1.34 eV, leading to worse agreement with the experimental activation energy, which is discussed later in the results.

For fcc metals, the diffusion coefficient of an atom can be described as[142]

$$D_s = f a_0^2 \nu_E \exp\left(\frac{\Delta S_m + \Delta S_f}{k}\right) \exp\left(\frac{-(\Delta H_m + \Delta H_f)}{kT}\right), \quad (4.9)$$

where  $f$  is the correlation factor,  $a_0$  is the lattice constant,  $\nu_E$  is the Einstein vibrational frequency,  $\Delta S_m$  is the vacancy migration entropy,  $\Delta S_f$  is the vacancy formation entropy,  $\Delta H_m$  is the vacancy migration barrier height,  $\Delta H_f$  is the vacancy formation enthalpy,  $k$  is the Boltzmann constant, and  $T$  is the absolute temperature. For most fcc metals,  $\Delta S_m + \Delta S_f = 1.8\text{--}2.0 k$ . [143] The overall vacancy-mediated self-diffusion activation energy is a sum of the contribution from vacancy formation energy (1.71 eV) and vacancy migration energy (0.98 eV). [144] Therefore, our calculated activation energy for cobalt self-diffusion in this simple swapping mechanism is  $1.71\text{ eV} + 0.98\text{ eV} = 2.69\text{ eV}$ , which is bracketed by the range of experimental values (2.52–2.98 eV).[145, 146] To apply surface intrinsic error corrections, there is an additional piece needed for the vacancy migration energy. The diffusing atom divides the vacancy volume at the transition state, creating additional internal surface. Following the methodology previously outlined by Sandberg et al.,[147] a surface correction of 0.21 eV is obtained for the migration energy. Using the corrected vacancy formation and migration energies, we get  $2.34\text{ eV} + 1.19\text{ eV} = 3.53\text{ eV}$ , which is higher than the range of experimental values. This over-estimation is a consequence of using a corrected  $E_f$  value that over-predicts the experimental  $E_f$ . There are many more possible self-diffusion mechanisms than the simple swapping mechanism we considered above for an otherwise perfect crystal with a single vacancy. These other mechanisms are likely to involve higher

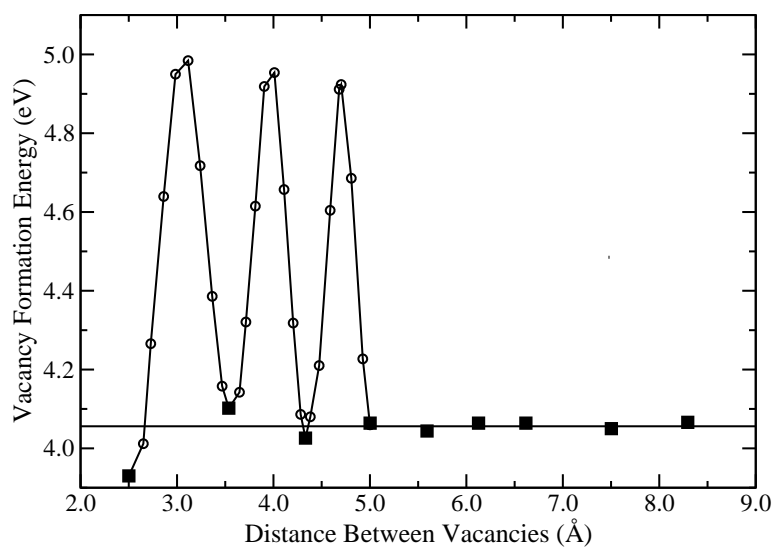


Figure 4.2: Vacancy formation energies (uncorrected) for vacancy pairs as a function of separation distance (solid squares). The horizontal line represents the infinite separation limit (twice the single vacancy energy). The diffusion pathway energy barriers are also shown (open circles) as computed from the NEB method.

energy pathways and we therefore suggest that the calculated corrected (uncorrected) value of 3.53 eV (2.69 eV) is a lower bound on the activation energy.

The uncorrected diffusion pathway energy barriers for two vacancies as a function of distance are also plotted in Figure 4.2. The corrected (uncorrected) barrier height for a pair of vacancies going from the first nearest neighbor position to the second nearest neighbor position is 1.26 (1.05) eV. The reverse pathway has a barrier of 1.09 (0.88) eV. Note that the diffusion barrier height for the reverse pathway is slightly less than the value for an isolated vacancy. The forward and reverse diffusion barrier heights for a pair of vacancies going from second to third nearest neighbors are 1.06 (0.85) and 1.14 (0.93) eV, respectively, compared with a value of 1.19 (0.98) eV for an isolated vacancy. The third to fourth nearest neighbor forward and reverse diffusion barriers are 1.11 (0.90) and 1.07 (0.86) eV. This means that a vacancy-Co exchange in the presence of another vacancy slightly lowers the diffusion barrier, further suggesting that it is energetically favorable for vacancies to coalesce in pure Co in the condensed phase.

We now turn to the substitution of tungsten atoms in cobalt with vacancy defects. We inserted one W atom into the pre-optimized defective structures consisting of one to three vacancies. We then optimized the structures with all forces converged to 0.05 eV/Å. The substitution energy is defined as

$$E_s = E_{W/Co} - E_W - (E_{V/Co} - E_{f,i}), \quad (4.10)$$

where the four terms on the right-hand side of Eq. (4.10) are the energy of the Co with the substitutional W atom, the energy of a W atom in bulk W, the energy of cobalt with vacancy defects, and the vacancy formation energy for creating  $i$  defects in Co, respectively. The values of  $E_s$  are 0.73, 1.41, and 2.15 eV for a single substitutional W atom and an additional zero to two vacancies, respectively. Thus, it is energetically more favorable to locate a W atom in a smaller cavity for at least up to two additional vacancies. This is likely due to the higher coordination of W offered by smaller cavities. It should be noted that the values of  $E_s$  have been corrected by  $\Delta\sigma$ .

We have investigated two different vacancy-mediated W diffusion mechanisms in Co for the case of a single W substitutional defect with an additional vacancy defect present to

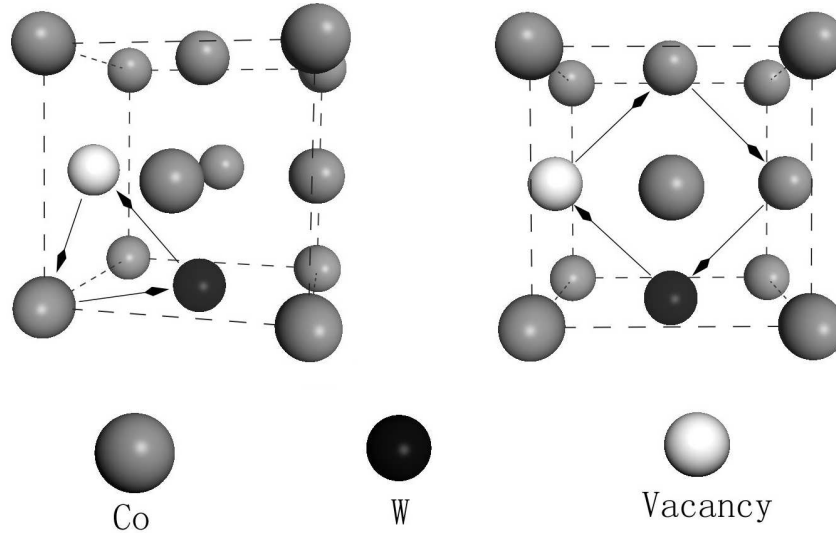


Figure 4.3: Schematic diagrams representing the triangle and quadrangle mechanisms. Left: triangle mechanism in the (111) plane. Right: quadrangle mechanism in the (100) plane. Atoms are not sized to scale.

facilitate W diffusion. These are identified as the triangle and quadrangle mechanisms. Diffusion of W involves multiple steps in these proposed mechanisms. The first step in each case is the exchange of W with a neighboring vacancy. Second, the vacancy migrates to the first nearest Co site following either a triangle or quadrangle path, in the  $\{111\}$  or  $\{100\}$  planes, respectively. Schematics of the triangle and quadrangle mechanisms are shown in Figure 4.3. The diffusion pathways for these mechanisms were calculated using the NEB method rather than the cNEB method. It was found to be quicker to locate the transition state by optimizing the highest energy image from a regular NEB path up-hill in energy using a quasi-Newton algorithm.

The uncorrected W diffusion pathways from the proposed mechanisms are plotted in Figure 4.4. The first peak in Figure 4.4(a) corresponds to the energy barrier for the exchange of the W atom and the vacancy; this step has a corrected (uncorrected) barrier height of 1.11 (0.90) eV. Remarkably, the barrier for W-vacancy exchange is 0.08 eV lower in energy than for Co-vacancy exchange. This is contrary to intuition because W is larger than Co

(has a larger bulk nearest neighbor distance), and therefore should require a larger energy to translate through bulk Co. The second peak in Figure 4.4(a) corresponds to the barrier for the vacancy-Co exchange, which has a height of 1.44 (1.23) eV. The barrier for Co-vacancy exchange when Co and the vacancy are nearest neighbors of W is 0.25 eV higher than in pure Co, indicating that Co hopping is hindered by the presence of W. The quadrangle diffusion pathway barriers are plotted in Figure 4.4(b). The first peak is the vacancy-W exchange, which is exactly the same as the first peak in Figure 4.4(a). The second and third peaks are the vacancy-Co exchanges in the quadrangle mechanism. These corrected (uncorrected) barrier heights are 1.15 and 1.09 (0.94 and 0.88) eV, respectively.

Using the barrier height from the W-vacancy exchange, we can calculate an analogous  $E_f$  value for the W-doped Co system using Eq. 4.8. Using this equation, we get  $E_f$  and corrected  $E_f$  values of 2.37 and 3.00 eV, respectively. As before with pure Co, the activation energy for diffusion is the sum of  $E_f$  and the NEB barrier height, 0.90 eV, which yields values of 4.11 (3.27) eV for the corrected (uncorrected) activation energy.[144] These values again over-predict the activation energy found in literature, 2.92 eV.[148]

The barriers heights for diffusion are related to the energy penalties of moving atoms to accommodate a transition state configuration. We have computed the average atomic displacement for each of the NEB barriers by computing the root mean square (RMS) displacement of the highest energy structure, the transition state (TS), relative to the initial minimum energy structure. Surprisingly, the W-vacancy exchange TS has the lowest RMS displacement, 1.28 Å, despite W having a larger diameter than Co. The RMS displacement of the Co-vacancy exchange TS in pure Co is 1.36 Å. Hence, the reason for the W-vacancy exchange having a lower barrier than the pure Co-vacancy exchange is that, for reasons unclear, the former requires less movement of adjacent atoms than the latter. The second step in the triangle mechanism involves Co-vacancy exchange in the nearest neighbor presence of W. The step has the highest TS RMS displacement, 1.41 Å. Accordingly, this step (second peak in Figure 4.4(a)) has a higher barrier than Co-vacancy exchange in pure Co. The second step in the quadrangle mechanism (second peak in Figure 4.4(b)) involves Co-vacancy exchange, where the vacancy goes from first to second nearest neighbor with respect to the W atom. This step has a slightly lower energy barrier than the pure Co-vacancy exchange,

consistent with the lower RMS displacement value of 1.33 Å. The third step in the quadrangle mechanism moves the vacancy from second to first nearest neighbor with respect to W. The TS RMS displacement for this step is 1.29 Å, about the same as the W-vacancy exchange, although the barrier height is 0.02 eV lower than the W-vacancy exchange.

#### 4.4 CONCLUSION

We have studied the vacancy formation energy in Co as a function of the number of vacancies and vacancy separation. There is an energetic driving force for vacancies to coalesce and the interactions between vacancies are relatively short ranged. The calculated cobalt self-diffusion activation energy is 3.53 eV (2.69 eV), with (without) the surface intrinsic error correction. These values bracket the experimental energy of 2.91 eV.[149] We have proposed two possible mechanisms for vacancy-mediated diffusion of W in bulk Co. The corrected (uncorrected) activation barriers for W-vacancy exchange in both the triangle and quadrangle mechanisms were found to be 1.11 (0.90) eV. The triangle mechanism has one additional step having a barrier of 1.44 (1.23) eV and the quadrangle mechanism has two additional steps having barriers of 1.15 and 1.09 (0.94 and 0.88) eV. These mechanisms have W-vacancy diffusion barriers similar to Co-vacancy diffusion barriers, meaning W and Co are expected to exhibit roughly similar diffusive behavior in solid Co. These findings are consistent with the experimental observations that W is essentially frozen in solid cobalt below 850°C, where Co is also immobile.[150]

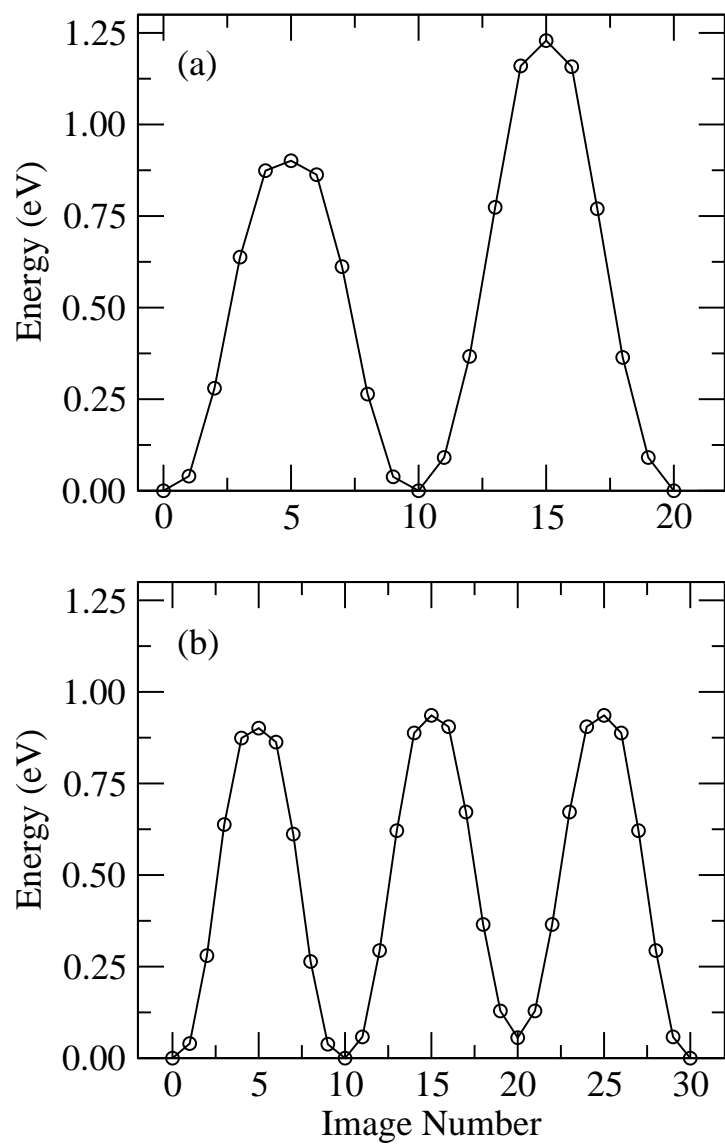


Figure 4.4: Calculated (uncorrected) diffusion pathways of tungsten following the (a) triangle and (b) quadrangle mechanisms.

## 5.0 REACTIVE FORCE FIELD DEVELOPMENT FOR COBALT

The content of this chapter is taken from M. R. LaBrosse, J. K. Johnson, and A. C. T. van Duin, “Development of a Transferable Reactive Force Field for Cobalt”, *J. Chem. Theory Comput.*, submitted (2009).

### 5.1 INTRODUCTION

Transition metals are widely used in a variety of industrial processes. Co is often combined with other elements to form dense alloys with high mechanical strength, resistance to deformation, and high resistance to corrosion. These are desirable properties for industrial applications in turbines, engines, and machine tooling.[151, 152] Metals such as Co, Fe, Ni, and Ru are employed in Fisher-Tropsch and other reactions.[1, 2] It is desirable to complement experimental research of these catalytic materials with computational studies. Design and improvement of catalysts requires detailed knowledge of reactions on simple and complex surfaces. Large-scale molecular dynamics simulations are ideal to study these materials under realistic conditions.

Quantum mechanical (QM) calculations using density functional theory can accurately describe bulk and surface energetics of condensed phase transition metals. However, DFT calculations have very unfavorable scaling with size. Non-reactive empirical force field (EFF) potentials employ harmonic equations to describe bond bending, bond stretching, and bond torsion events, with additional expressions to handle long-range electrostatic and van der Waals interactions.[153, 154] These potentials have an advantage over DFT in that large-scale molecular dynamics simulations are feasible. However, non-reactive EFF potentials

do not allow for bond breaking and forming events. In 2001, van Duin et al. developed a reactive empirical force field for hydrocarbons capable of handling changes in bond order without having to explicitly define atom connectivity.[155] Since its development, the ReaxFF formalism has been applied to many different systems.[156, 157, 158, 159, 160, 161, 162, 163] Force field parameters for ReaxFF are found by fitting to DFT data using a successive one-parameter search technique.[164] We present the development and validation of condensed phase Co parameters for molecular dynamics simulations with ReaxFF as well as condensed phase molecular dynamics applications.

## 5.2 METHODOLOGY

### 5.2.1 QM calculations

The training set for cobalt parameterization was comprised of DFT calculations performed with VASP.[115, 116, 117, 118] For these calculations, a Vanderbilt ultrasoft pseudopotential[119, 120, 121] was used to describe the core electrons and the electron exchange-correlation functional was described by the Perdew-Wang (PW91)[165] generalized gradient approximation. The VASP calculations show good agreement with experimentally obtained values for a variety of fcc cobalt properties: lattice constants ( $a_0$ ), cohesive energy ( $E_0$ ), magnetization ( $\mu_B$ ), bulk modulus ( $B_0$ ), and elastic strain moduli ( $c_{11}$ ,  $c_{12}$ ,  $c_{44}$ ), as shown in 5.1. We note that fcc is the stable phase of Co at temperatures greater than 690 K.[166]

### 5.2.2 ReaxFF

ReaxFF is a bond-order potential based on a concept first introduced by Tersoff.[169] The bond order/bond energy relationship is the cornerstone of the reactive force field. [155] Typical EFF methods involve simple empirical equations to describe bond stretching, bond bending, and bond torsion potentials. Expressions for long range electrostatic and van der Waals forces are added to describe the non-bonded interactions. The main difference between ReaxFF and non-reactive force fields is that ReaxFF does not require a user-specified

connectivity table. Connectivity between atoms is determined at each time step during a simulation. This separates ReaxFF from most other EEF potentials in that bond breaking and bond forming events can be captured during molecular dynamics simulations.

For a ReaxFF description of Co, bond orders are calculated from interatomic distances. The appropriate bond energy is determined by correcting with over- or under-coordination energies. Dispersion interactions are described by van der Waals potential functions. The total energy is simply a summation of the partitioned energy pieces, shown by

$$E_{\text{system}} = E_{\text{bond}} + E_{\text{over/under}} + E_{\text{vdW}}. \quad (5.1)$$

Molecular dynamics simulations in the canonical ensemble (NVT) were performed using a velocity Verlet algorithm and a time step of 1.0 fs and a temperature damping constant of 250 fs. For MD simulations at higher temperatures, a time step 0.5 fs was required to conserve energy during micro-canonical simulations. The system temperature was controlled by a Berendsen thermostat.[170]

## 5.3 RESULTS AND DISCUSSION

### 5.3.1 QM training of force field

For ReaxFF to accurately describe cobalt in the condensed phase, the QM training set should include descriptions of many of the possible crystalline phases. Equation of state (EOS) curves for sc, bcc, fcc, hcp, and diamond phases were generated by performing complete relaxations on cobalt unit cells at various fixed volumes. These data were used to generate a plot of the cohesive energy as a function of the lattice volume, which was fitted to a Murnaghan EOS[171] yielding equilibrium cohesive energies, equilibrium lattice constants, bulk moduli, and elastic strain moduli, shown in 5.2. A complete volume relaxation was performed to verify the Murnaghan EOS identified the correct equilibrium volume and cohesive energy for each phase. It should be noted that ReaxFF is fit to these EOS curves, but the cohesive energy is taken as the experimental value of 4.39 eV. The Murnaghan EOS

curves are shown in 5.1. Due to the low atomic packing fraction of the diamond phase (0.34), the EOS curve shows a much higher equilibrium volume and cohesive energy than the other phases. For comparison, the packing fraction for the bcc, fcc, and hcp phases is 0.68-0.74.

Elastic constants are important for capturing bulk phase strain behavior of cobalt. They are measured experimentally by applying a mechanical strain to the crystal. The direction of the strain with respect to the crystal cell corresponds to different elastic constants. In simulations, these moduli are calculated by manipulating the lattice vectors describing the positions of the atoms, a procedure outlined by Mehl and co-workers. [172] These vectors can be perturbed to represent a strain on the system, which leads to calculation of the different elastic moduli. The elastic constants  $c_{11}$ ,  $c_{12}$ , and  $c_{44}$  for many phases of cobalt are shown in 5.2, along with equilibrium information extracted from the Murnaghan EOS curves in 5.1.

Accurate description of vacancies and defect behavior is critical to performing large scale molecular dynamics simulations. Vacancies mediate diffusion and bulk crystal phase transitions. To capture the possible vacancy interactions that may be encountered, we include vacancy formation energies for 1-6 coalesced vacancies in fcc cobalt in the QM training set. The formation energy has been calculated on a per vacancy basis and linearly decreases from 2.34-1.92 eV for 1-6 coalesced vacancies, respectively.[173] The data suggest that vacancies prefer to be coalesced rather than separated. LaBrosse et al. have also calculated the two-vacancy formation energy as a function of vacancy-vacancy separation. Two vacancies are placed in a  $3\times 3\times 3$  supercell of fcc cobalt at first through ninth nearest neighbors. These results show that it is most energetically favorable to have two vacancies as nearest neighbors, again indicating that vacancies prefer to be coalesced in the bulk.

In addition to vacancy studies, we have also calculated energies of amorphous Co configurations and stacking fault energies for a variety of bulk crystal defects. Amorphous structures were generated from VASP by performing an NVT molecular dynamics on a 108 atom fcc lattice at 2500 K for 450 fs. Single images were pulled from the calculation at time intervals of 90 fs, large enough to prevent correlation between geometries. Single point energy calculations were performed on these images to include in the training set. To obtain for the investigated cubic phases, we have induced a half-lattice offset in the [100] direction. For

the hcp phase stacking fault energies, we have induced a layering transition from hcp(0001) to fcc(111).

For simulations of a surface-active material such as cobalt to be accurate, the behavior of surfaces must be included in the training set. Of particular interest is the surface formation energy ( $E_{\text{sf}}$ ), defined by

$$E_{\text{sf}} = (E_{\text{s}} - nE_0) / (2A), \quad (5.2)$$

where  $E_{\text{s}}$  is the energy of the relaxed crystal slab exposed to a vacuum,  $n$  is the number of atoms in the slab,  $E_0$  is the cohesive energy per atom of the crystal phase, and  $A$  is the area of the surface exposed to vacuum. For our calculations, a minimum of 10 Å was used for the vacuum layer. The factor of 2 arises because two sides of the crystal slab are exposed to vacuum and therefore relaxed. For the cubic phases (sc, bcc, fcc), this was done for low-Miller index surfaces; (100), (110), and (111). For the hcp phase, we have investigated the (0001) surface. Finally, it is important to capture the energetics of surface with higher Miller indices. For this, we have calculated the surface formation energy of the (310) and (510) surfaces for the cubic phases sc, bcc, and fcc. Surface formation energies are shown in 5.4.

Surface reconstruction is observed when adatoms on an exposed surface migrate to form a more energetically favorable surface. The migration behavior of cobalt atoms on an exposed surface must be captured by ReaxFF. For this, adatoms were placed on a variety of sc, bcc, and fcc surfaces. These adatoms were placed on various top, bridge, or hollow sites. The DFT calculations were fully relaxed such that the adatom was allowed to move to the lowest energy configuration.

Small groups of atoms are needed to connect the near bulk-like behavior of catalytic materials to that of the condensed phase crystal. This is particularly important for future comparisons with experimental work, such as formation of hollow nanospheres[174] or CO dissociation on cobalt nanoparticles.[175, 176] For this, we have calculated the cohesive energies for a set of small clusters of sizes 2, 3, 4, 5, 6, 8, and 13 atoms, pictures of which are shown in 5.2. The clusters were subjected to full ionic relaxation and their energies (per atom) are plotted in 5.4.

### 5.3.2 Parameterization and validation of ReaxFF

During the force field optimization procedure, the goal is to reproduce heats of formation to within 4.0 kcal/mol and bond lengths to within 0.01 Å. Calculations using the fitted parameters agree very well with many of the systems included in the training set. ReaxFF parameters describe the high density crystal phases (fcc, hcp, bcc), clusters, and defect behavior particularly well. The fit to the hcp, fcc, and bcc EOS curves can be seen in 5.3. As previously mentioned, the cohesive energy is fit from the experimental value of 4.39 eV, not the DFT value of hcp Co (4.99 eV). ReaxFF predicts an hcp cohesive energy of 4.48 eV. Elastic moduli calculated from ReaxFF optimized parameters, shown in 5.3, compare well with data in 5.2, particularly for the fcc and hcp phases. The parameters also agree well with clean surface formation energy calculations, shown in 5.4.

Not all the data in the training set can be fitted equally well. The ReaxFF fit to the diamond phase equation of state (not shown) fails to capture the *ab initio* equation of state. Likewise, ReaxFF predictions to the diamond phase elastic moduli are not correct. However, 5.2 shows the diamond phase is more than 1 eV per atom higher in energy than the most stable hcp and fcc phases. Energetics would dictate that the diamond phase is not expected to be sampled during molecular dynamics simulations, therefore the lack of agreement is not critical.

To validate the fitted Co ReaxFF parameters, the optimized force field is compared to additional VASP calculations to test their accuracy at predicting DFT calculations that were withheld from the training set. In addition to DFT, the ReaxFF Co potential is compared with embedded atom method (EAM) results. For our EAM calculations with Co, we chose to use parameters from Pasianot and Savino[177] implemented within the LAMMPS code.[178] To test the ReaxFF parameters, the following calculations were chosen to examine their predictive ability: eight surface calculations, two surface adatom calculations, two small clusters, and four vacancy defect calculations (two in the hcp phase and two in the bcc phase). Surface formation energies and adatom adsorption energies are presented side by side in 5.5. ReaxFF performs fairly well at predicting surface formation and adatom adsorption

energies as compared with the DFT calculations. The predictions from the EAM potential systematically under-predict both the surface formation and adatom adsorption energies.

Two additional clusters have been constructed for validation of ReaxFF parameters: one with 7 atoms and one with 9 atoms. As can be seen from 5.4, ReaxFF is in very good agreement with the calculated cohesive energies from VASP while the EAM potential for Co over-predicts all of the cluster energies. As a reference, 5.4 also includes the data for the other cobalt clusters included in the fitting. These are included to show that ReaxFF correctly predicts the trend of increasing the cluster size. As the cluster size increases, the cohesive energy becomes larger and should approach the limit of cohesive energy of bulk hcp Co, the lowest energy phase.

Defect behavior must also be validated. The training set explores vacancy coalescence and vacancy-vacancy interactions in fcc cobalt. For validation, the other high-density phases (bcc and hcp) were chosen. In each phase, two calculations were performed with VASP: a coalesced 4-vacancy configuration and a separated 2-vacancy configuration. The separation distance for the vacancy-vacancy calculation is somewhat arbitrary, so the fourth nearest-neighbor was chosen for both phases. As seen from 5.6, ReaxFF is in good predictive agreement with the DFT calculations. These results, combined with the surface formation energies (5.5) and cluster cohesive energies (5.4), provide confidence that the optimization procedure provide a good overall fit to the quantum mechanical data.

### 5.3.3 Thermophysical property predictions from ReaxFF

The optimized ReaxFF parameters have been used to calculate the melting point of condensed phase cobalt. To obtain an estimate for the melting temperature, we used the method of temperature hysteresis, which involves performing molecular dynamics simulations in the NPT ensemble to observe the maximum super-heating temperature ( $T_+$ ) and recrystallization temperature ( $T_-$ ). [179, 180] The melting point is then computed from

$$T_{\text{mp}} = T_+ + T_- - \sqrt{T_+ T_-}. \quad (5.3)$$

An example calculation of the hysteresis loop is shown in 5.5. To generate these loops, an ideal fcc crystal consisting of 500 atoms was subjected to a specified heating rate by

changing the set temperature a small amount at each time step. Using a timestep of 0.5 fs, a temperature change of 0.005 K at each timestep yields an overall heating rate of  $10^{13}$  K/s, a typical temperature change rate found in previous simulation work on large systems.[179] Lower temperature change rates,  $10^{10}$  K/s, are possible for small nanoclusters melting over a smaller temperature range, as has been shown by Thompson and co-workers.[180] After the crystal had deformed to become a liquid state, this geometry was cooled at the same rate until recrystallization was observed. Both phase transition events show dramatic changes in the potential energy, easily observed in 5.5.

We note that Ojwang and co-workers reported a heating rate of  $2.5 \times 10^9$  K/s for calculating the melting point of Al clusters using ReaxFF.[162] However, the reported heating rate is in error and the actual heating rate based on the temperature range, time step, and number of MD steps is  $2.13 \times 10^{12}$  K/s. This is close to the heating rate used in our work.

Point defects may also effect the melting point of a material. The effect of vacancies on the melting point was studied at the temperature change rates of  $10^{13}$  K/s; results are shown in 5.7. For these calculations, 5 cobalt atoms (vacancy concentration of 1%) were selected at random and removed from the simulation box. The hysteresis loops were then generated in the same manner as before. The addition of vacancy defects lowers the estimate of  $T_{\text{mp}}$ , but both ReaxFF values are higher than the experimental value of 1768 K.[167] We note that Järvi and co-workers have predicted the melting point of Au from ReaxFF using a procedure in which a solid/liquid interface was followed at various temperatures to observe solid or liquid phase growth.[163] At the melting point, no phase growth is observed. Using their Au-ReaxFF potential, they observed a Au melting point of  $(2125 \pm 25)$  K, substantially higher than the experimental value of 1337 K. Also shown in 5.7 are the hysteresis results for EAM. The EAM potential under-predicts the experimental melting temperature for both the pure and defected crystal.

In addition to calculating a melting point, ReaxFF has been used to predict liquid ( $D_l$ ) and solid ( $D_s$ ) phase diffusion coefficients. For cobalt in the liquid phase, several one ns molecular dynamics runs have been performed at various temperatures to obtain mean square displacement (MSD) trajectories. In order to compare with literature results, temperatures below the predicted ReaxFF melting point are needed. This was accomplished

by starting with a melted configuration and doing a short equilibration at the temperature of interest. The melt is meta-stable at these temperatures. From the MSD trajectories, diffusion coefficients were obtained and used to determine the activation energy ( $E_a$ ) for self-diffusivity, according to the Arrhenius expression,

$$D_s(T) = D_0 \exp^{-E_a/(kT)}. \quad (5.4)$$

By plotting the log of the temperature-dependent diffusion coefficient ( $\ln D_s$ ) versus the inverse temperature ( $1/T$ ), a linear relationship can be obtained to find the Arrhenius prefactor ( $D_0$ ) and  $E_a$ . Results for temperatures ranging from 2000-2800 K are shown in 5.6. A linear fit to these data yields an activation energy of 65.5 kJ/mol and an Arrhenius prefactor of  $1.273 \times 10^{-3}$  cm<sup>2</sup>/s. By inserting the linear fit parameters into Eq. 5.4, direct comparison are made with predicted diffusion coefficients from literature at other temperatures. Yokoyama and co-workers have derived a theoretical model to approximate  $D_1$  for a hard-sphere fluid using correlation entropy. With this model, they have employed two variations to estimate liquid self-diffusivities. The first method used experimental results for the volume and viscosity at the melting temperature.[181] The second approach is a more generic model constructed from other metals and was used to predict  $D_1$  for Co.[182] Han and co-workers have performed experiments to measure the surface tension of pure liquid cobalt, which can be related to the liquid self-diffusivity through viscosity and the Stokes-Einstein relationship. [183] These predictions are shown in 5.8. As can be seen, liquid self-diffusivities predicted from ReaxFF are smaller than each of the other methods.

These results, along with the melting temperature results, suggest possible room for improvement in the force field parameters. The training set could be expanded to include vacancy-mediated diffusion barriers for various Co crystals; this would likely provide a more accurate description of the bulk phase dynamics. However, LaBrosse et al. have recently shown that the DFT activation energy for vacancy-mediated diffusion in fcc Co over-predicts experiments.[173] Hence, careful consideration must be made before including additional DFT calculations and re-tuning the Co force field parameters.

Predicted self-diffusivities in the fcc solid phase were found in a similar manner. However, self-diffusivities in the solid phase must be measured at their equilibrium vacancy concentration  $C_{\text{eq}}$ . Obtaining this value is trivial, as it is related to the vacancy formation energy ( $E_{\text{vf}}$ ) through  $C_{\text{eq}}(T) = \exp(-E_{\text{vf}}/kT)$ .<sup>[185]</sup> For our calculations, we used the literature value of 1.34 eV for the mono-vacancy formation energy.<sup>[134]</sup>

At temperatures near the melting point (1768 K), the equilibrium concentration of vacancies is approximately  $10^{-4}$ . Simulations at this concentration of defects requires a very large simulation box. Therefore, several smaller simulation boxes were used ranging from 108-864 atoms, with one atom left out in each system for the mono-vacancy defect. These data were plotted in 5.7 for temperatures of 1800 and 2200 K. For metal systems, the diffusion coefficient is proportional to  $\exp(-E_{\text{vf}}/kT)$ ,<sup>[142]</sup> which leads to a linear relationship between  $D_s$  and  $C$ . Linear fits to these data were forced through the origin because there is no diffusion observed without vacancies at these temperatures in the solid phase.

Predicted values of the solid diffusion coefficient for ReaxFF at temperatures near the experimental and ReaxFF-predicted melting points are presented in 5.9. Also represented are extrapolated values from the Arrhenius expression from Nix and Joumot.<sup>[149]</sup> As with the liquid phase diffusion results, ReaxFF under-predicts the experimental results (within a factor of 4). In both the liquid and solid cases, this can be explained by examination of the liquid activation energies from Arrhenius expressions. For ReaxFF, the activation energy is 65.5 kJ/mol. Han and co-workers report a value of 26.5 kJ/mol from their surface tension experiments.<sup>[183]</sup> Two different embedded atom potentials for cobalt report values of 48.8 and 31.7 kJ/mol.<sup>[184, 177]</sup> The higher activation energy for ReaxFF means a higher energy penalty must be paid to induce mobility, which explains under-prediction of diffusion coefficients.

## 5.4 CONCLUSION

We have developed reactive force field parameters for cobalt that give good descriptions of the energetics of crystal phases, amorphous configurations, various clusters, vacancies,

and surfaces. Validation of the fitted cobalt parameters shows good predictive agreement with a variety of different DFT surface, adatom, and defect calculations not included in the training set. Predicted melting point and diffusion coefficients in the liquid and solid phases indicate ReaxFF somewhat over-predicts the cohesive energy of the condensed phase. We have compared predictions from ReaxFF with an accepted EAM parameterization for Co. We find that surface properties predicted from ReaxFF are in much better agreement with DFT calculations than predictions from EAM.

ReaxFF can be extended to include cross-parameters for surface chemistry involving Co-C, Co-O, and Co-H in a straightforward way. Previous work has shown transition metal force fields can be extended to accurately describe heterogeneous interactions.<sup>[156, 186, 187]</sup> This work is a critical first step toward modeling condensed phase systems containing Co with many thousands of atoms, e.g., crack propagation in Co alloys, and heterogeneous systems such as high pressure reactions on supported catalysts.

Table 5.1: Comparison of calculated condensed phase properties of fcc Co with experiments. Values are calculated from *ab initio* methods described in the text.

Property	VASP	Experiment
$a_0$ (Å)	3.537	3.54 <sup>a</sup>
$E_0$ (eV)	4.97	4.39 <sup>b</sup>
$\mu_B$	1.68	1.72 <sup>b</sup>
$B_0$ (GPa)	202	191 <sup>b</sup> , 198 <sup>c</sup>
$c_{11}$ (GPa)	237	223 <sup>c</sup>
$c_{12}$ (GPa)	184	186 <sup>c</sup>
$c_{44}$ (GPa)	149	110 <sup>c</sup>

<sup>a</sup> Taylor[123]

<sup>b</sup> Kittel[167]

<sup>c</sup> Gump et al.[168]

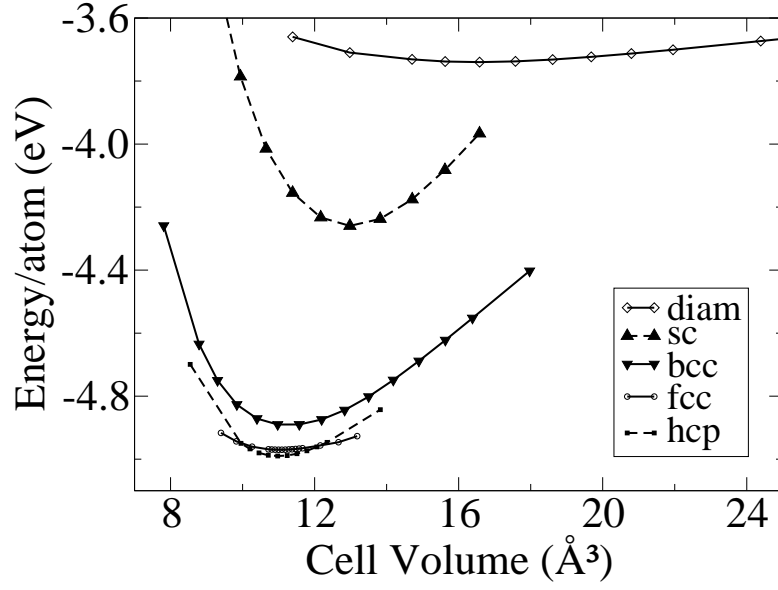


Figure 5.1: Murnaghan EOS curves for sc, bcc, fcc, hcp, and diamond phases of cobalt.

Table 5.2: Elastic Moduli, lattice constants, and cohesive energies of Co in the sc, bcc, fcc, hcp, and diamond phases calculated from *ab initio* methods.

Property	sc	bcc	fcc	hcp	diamond
$a_0$ (Å)	2.349	2.823	3.537	2.502, 4.058	5.069
$E_0$ (eV)	4.26	4.89	4.97	4.99	3.74
$B_0$ (GPa)	137	179	202	199	75
$c_{11}$ (GPa)	205	143	237	262	87
$c_{12}$ (GPa)	103	197	184	168	69
$c_{44}$ (GPa)	-49	108	149	97	42

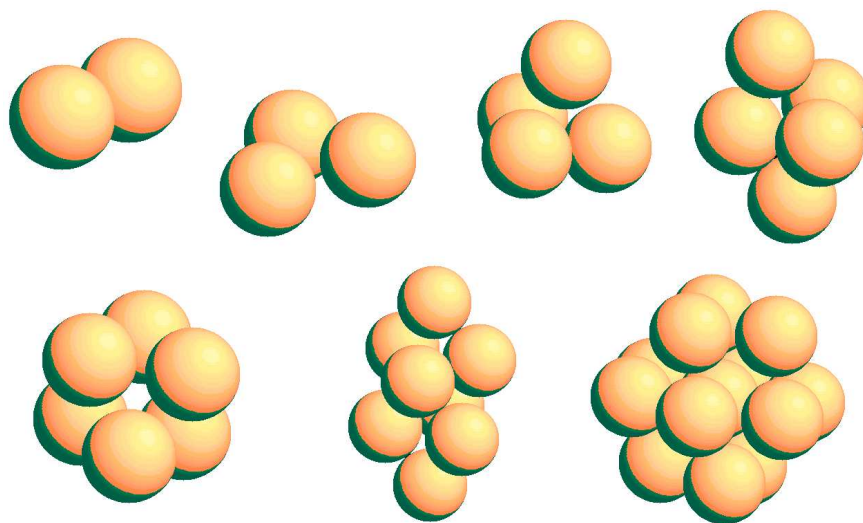


Figure 5.2: Co clusters consisting of 2-6, 8, and 13 atoms.

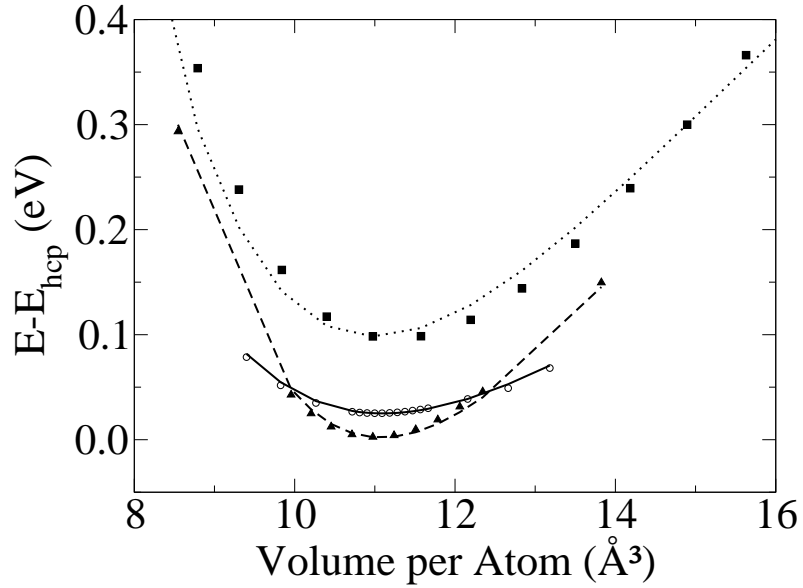


Figure 5.3: ReaxFF parameter fit to high density equations of state (fcc, hcp, and bcc). The squares, circles, and triangles represent the VASP data for the bcc, fcc, and hcp phases, respectively. The dotted, solid, and dashed lines are the ReaxFF fits to the DFT data for the bcc, fcc, and hcp phases, respectively.  $E_{hcp,min}$  is the energy of the hcp Co phase from VASP or ReaxFF, where appropriate.

Table 5.3: ReaxFF fit to elastic moduli of Co phases. All elastic constants have units of GPa.

	sc	bcc	fcc	hcp
$B_0$	106	158	205	208
$c_{11}$	202	173	237	268
$c_{12}$	58	151	189	178
$c_{44}$	-47	174	172	113

Table 5.4: Surface formation energies using ReaxFF optimized parameters as compared with VASP calculations. All formation energies have units of ( $\text{J}/\text{m}^2$ ).

Surface	VASP	ReaxFF
hcp (0001)	2.11	2.08
fcc (100)	2.39	2.12
fcc (510)	2.54	2.31
bcc (100)	2.28	2.11
bcc (310)	2.30	2.13
sc (100)	1.46	1.46
sc (111)	1.62	1.17
sc (510)	1.63	1.53

Table 5.5: Predicted surface formation energies ( $\text{J/m}^2$ ) and adatom binding energies ( $\text{kJ/mol}$ ) using ReaxFF optimized parameters. The ReaxFF values have been compared to VASP and EAM calculations.

Surface	VASP	ReaxFF	EAM
fcc (110)	2.35	2.32	1.31
fcc (111)	2.03	2.07	0.96
fcc (310)	2.59	2.38	1.36
bcc (110)	2.07	2.03	1.03
bcc (111)	2.35	2.37	1.86
bcc (510)	2.29	2.12	1.20
sc (110)	1.62	1.42	0.83
sc (310)	1.54	1.63	0.71
sc (100) + adatom	77.0	80.9	86.5
bcc (111) + adatom	122.5	122.9	164.7

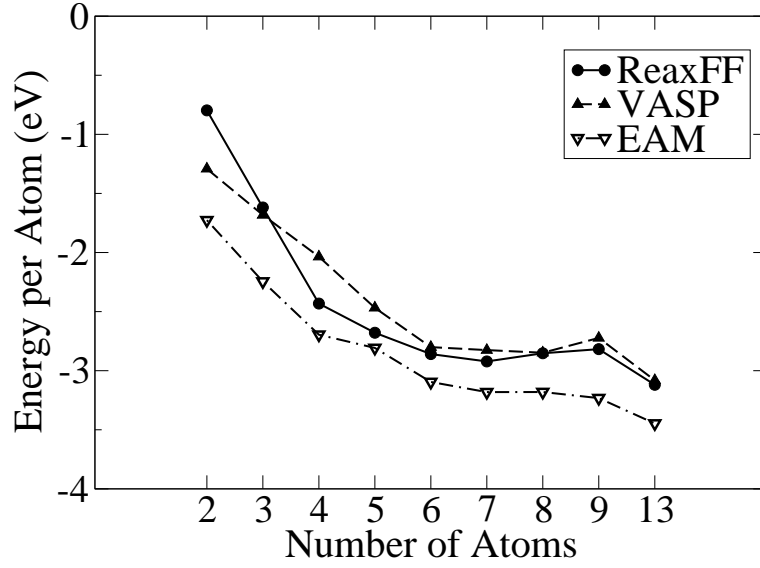


Figure 5.4: Comparison of predicted ReaxFF, EAM, and VASP cohesive energies for 7 and 9 atom clusters. Also included are the data for the 2, 3, 4, 5, 6, 8, and 13 atom clusters included in the training set.

Table 5.6: Predicted 2 (2V) and 4 (4V) vacancy formation energies using ReaxFF optimized parameters. The ReaxFF values are compared to VASP and EAM calculations in bcc and hcp cobalt. All formation energies have units of eV.

System	VASP	ReaxFF	EAM
bcc(2v)	1.82	2.15	1.47
bcc(4v)	1.50	1.45	0.74
hcp(2v)	2.49	2.57	0.62
hcp(4v)	2.20	1.98	0.58

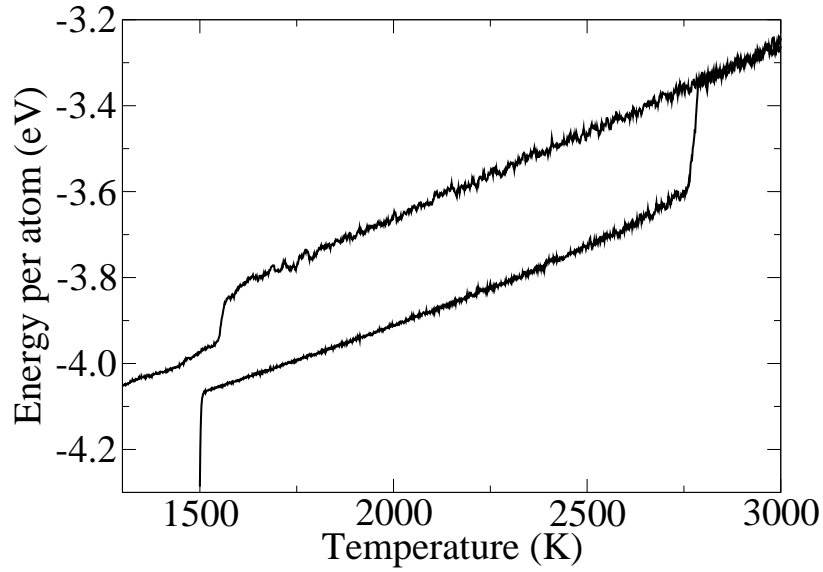


Figure 5.5: Temperature hysteresis loop using ReaxFF for a heating/cooling rate of  $10^{13}$  K/s using a perfect fcc Co crystal of 500 atoms.

Table 5.7: Comparison of melting point estimates from temperature hysteresis loops for ReaxFF and EAM methods at a temperature change rate of  $10^{13}$  K/s. All temperatures are in K.

	% Vac	$T_+$	$T_-$	$T_{mp}$
ReaxFF	0	2765	1563	2249
	1	2678	1455	2159
EAM	0	2073	842	1594
	1	2015	810	1547

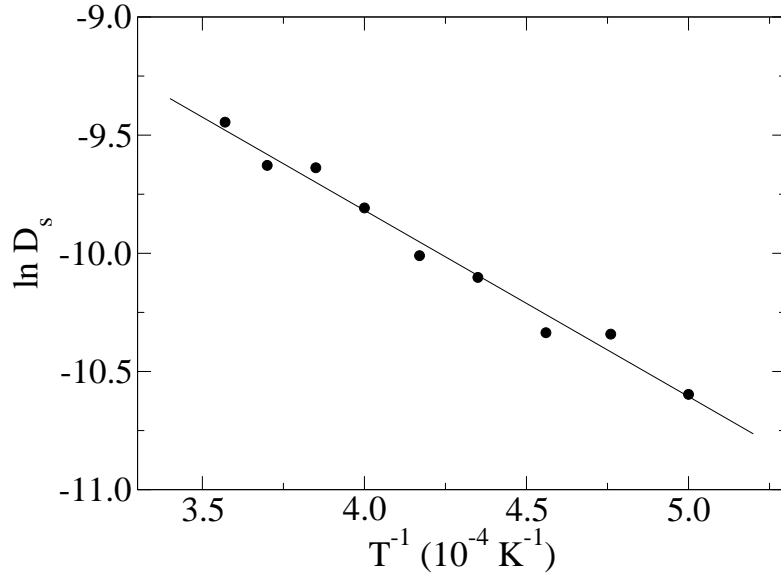


Figure 5.6: Arrhenius plot for liquid Co at various temperatures. The solid line represents the linear fit to the data.

Table 5.8: Calculated ReaxFF self-diffusion coefficients of liquid Co as compared with various methods for prediction: hard-sphere (HS)[181], correlation entropy (CE)[182], surface tension (ST)[183] measurements, and embedded atom methods (EAM1)[177] and (EAM2)[184]. All diffusion coefficients have units of ( $10^{-5} \text{ cm}^2/\text{s}$ ).

T (K)	ReaxFF	HS	CE	ST	EAM1	EAM2
1768	1.48	—	—	3.95	4.67	7.30
1823	1.69	4.55	3.51	4.19	5.16	7.79
1873	1.90	5.24	4.20	4.39	5.62	8.24
1923	2.11	5.68	4.58	4.59	6.10	8.69
2023	2.59	6.47	—	4.98	7.10	9.58

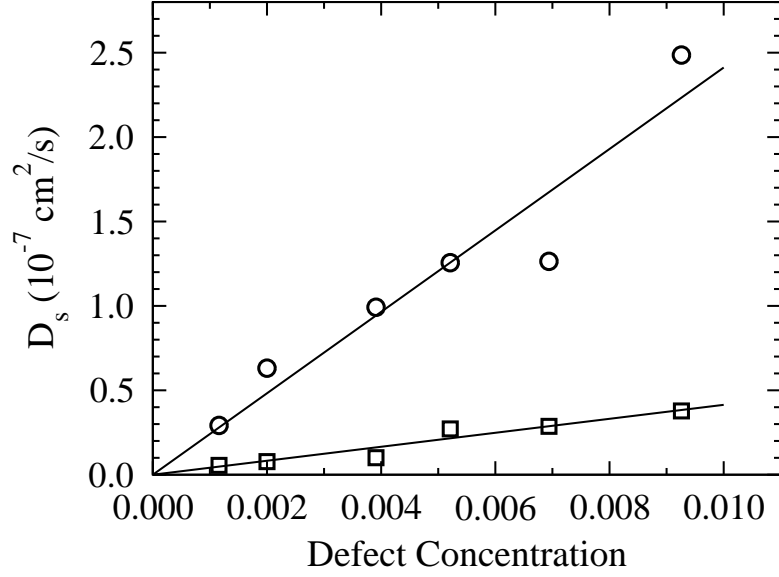


Figure 5.7: Plot of diffusion coefficients in the fcc solid as a function of the concentration at temperatures of 1800 (squares) and 2200 K (circles).

Table 5.9: Calculated ReaxFF self-diffusion coefficients for solid fcc Co compared with experiment.[149]

ReaxFF		Experiment	
T (K)	$D_s$ (cm <sup>2</sup> /s)	T (K)	$D_s$ (cm <sup>2</sup> /s)
1800	$7.32 \times 10^{-10}$	1768	$1.91 \times 10^{-9}$
2200	$2.05 \times 10^{-8}$	2200	$8.10 \times 10^{-8}$

## 6.0 REACTIVE FORCE FIELD FOR HETEROGENEOUS SYSTEMS

The content of this chapter is taken from M. R. LaBrosse, J. K. Johnson, and A. C. T. van Duin, “Development of a Reactive Force Field Potential for Co/C/O”, in preparation.

### 6.1 INTRODUCTION

First-principles methods can be used to accurately describe various catalytic surface interactions. However, these quantum mechanical methods become computationally infeasible as the system size approaches hundreds of atoms. Statistical mechanical methods typically employ empirical potentials that greatly exceed the system size limitations of QM methods, but trade accurate descriptions of physics for performance. One example of such a potential is an empirical force field, which employs harmonic equations to describe bond bending, bond stretching, and bond torsion events, with additional expressions to handle long-range electrostatics and van der Waals interactions.[153, 154] However, these non-reactive EFF potentials do not allow for bond breaking and forming events.

As previous discussed, the Tersoff potential is the first attempt to accurately describe the energetics of reactions.[169] This potential uses a bond order term to describe the coordination state of each atom. Since its conception, variants of the bond order potential have been introduced.[188, 189] In recent years, the ReaxFF formalism has been expanded to include descriptions for many different binary and tertiary systems.[156, 157, 158, 159, 160, 161, 162, 163, 186, 187] In this chapter, we present the development of a reactive force field for binary (Co/C, Co/O) and tertiary (Co/C/O) catalytic systems from QM methods. We also present applications using the optimized reactive force field parameters.

## 6.2 METHODOLOGY

### 6.2.1 QM Calculations

To properly describe the binary and tertiary interactions of the system, force field parameters are optimized against an extensive training set of QM data. All QM calculations are performed using the density functional theory software package VASP.[115, 116, 117, 118] Previous DFT work on Co[190] used a Vanderbilt ultrasoft pseudopotential to describe the core electrons of Co atoms.[119, 120, 121] The electron exchange-correlation functional was described by the Perdew-Wang (PW91)[165] generalized gradient approximation. For consistency, the same type of pseudopotential and exchange-correlation functional was used to describe C and O. In all of our bulk and surface calculations, the Brillouin zone is sampled with a reciprocal k-points spacing no greater than  $0.03 \text{ \AA}^{-1}$ .

The DFT training set is comprised of five different surfaces for adsorption calculations: hcp(0001), hcp(1 $\bar{1}$ 01), fcc(011), fcc(001), and bcc(011). These five surfaces were chosen because they offer different coordination features for adsorbates, based on their first and second layer atom positions. Two additional surfaces, fcc(111) and bcc(001), are used in calculations to validate the optimized ReaxFF parameters, which will be discussed in a later section. These two surfaces were extracted from the original group of seven surfaces because their features are similar to the five surfaces included in the DFT training set. For example, the fcc(111) and hcp(0001) surfaces share the same two-dimensional surface atom densities and have identical first layers, but have different layer ordering.

All surfaces were constructed in an orthorhombic manner, such that each surface layer contains four atoms. Surfaces range between five to eight layers, depending on layer spacing, such that each surface slab is roughly  $8 \text{ \AA}$  in thickness. The atom positions in the bottom two to four layers were fixed, again depending on the surface. The adsorbates and atoms in the other layers were fully relaxed during calculations. The clean surfaces were relaxed with approximately  $15 \text{ \AA}$  of vacuum so that the later addition of adatoms or molecules would still leave at least  $10 \text{ \AA}$  of vacuum spacing. Due to the choice of fixing the bottom layers, surface dipole corrections were applied to all VASP surface calculations.

### 6.2.2 ReaxFF

ReaxFF determines bond orders at every MD timestep allowing for dynamic formation and destruction of bonds in the system. Instantaneous bond orders are calculated from interatomic distances. The bond order energy is then corrected by an under- or over-coordination term to force the bonded atoms to have an appropriate number of bonded interactions. Energy contributions from other sources are largely described by harmonic functions. The total energy of the system is calculated through a summation of the partitioned energy pieces, shown by

$$E_{\text{system}} = E_{\text{bond}} + E_{\text{over/under}} + E_{\text{val}} + E_{\text{tors}} + E_{\text{conj}} + E_{\text{vdW}} + E_{\text{Coul}} + E_{\text{charge}}, \quad (6.1)$$

where the terms on the right hand side of the equation are, respectively, the bond-order, over- or under-coordination penalty, valence angle, torsion angle, angle conjugation, van der Waals, Coulomb, and charge polarization energies.

Molecular dynamics simulations in the canonical ensemble were performed using a velocity Verlet algorithm and a time step of 0.5 fs. This timestep was found to be the maximum time step to conserve energy during micro-canonical simulations at the higher temperatures used during MD simulations. The system temperature was controlled by a Berendsen thermostat with a temperature damping constant of 200 fs.[170]

## 6.3 RESULTS

### 6.3.1 Force field parameterization

Parameter optimizations for Co, C, O, and binary C/O interactions are taken from previous studies.[155, 190] These parameters are not changed in this work. To obtain descriptions for binary (Co/C, Co/O) and tertiary (Co/C/O) ReaxFF interactions, many *ab initio* calculations were performed on a variety of systems. Because this potential will be primarily used in calculations of surface reactions on Co using carbon and oxygen, a comprehensive set of surface adsorption calculations were performed to capture different adsorption energies. A

previously developed description for Co showed that low density phases of Co were not energetically favorable.[190] Hence, in this chapter we limit our DFT training set calculations to the hcp, fcc, and bcc phases. The surfaces used were described in the previous section.

Tables 6.1 and 6.2 contain the VASP adsorption energies for C and O adatoms, 4 atom C and O adlayers, dissociated CO, and molecular CO adsorbed on Co surfaces. ReaxFF must handle adsorption of C, O, and CO species on a variety of surfaces so that surface chemistry of these species can be accurately observed. Adsorption energies for both VASP and ReaxFF use graphite and gas-phase oxygen ( $O_2$ ) as the ground state references for C and O, respectively. The adlayer adsorption energies are presented on a per adsorbate basis ( $E_{\text{ads}}/4$ ). The goal during parameter optimization is to reproduce heats of formation as close to the VASP results as possible. This can be very difficult because C and O atoms visit many different states in the breadth of configurations presented in the training set. For example, an O adatom has a much different coordination, bond order, and charge than the an O atom in a CO molecule. As such, some configurations are fit very well (e.g. C adlayer on the hcp(0001) surface), and some systems are not described as accurately (e.g. CO molecule on the hcp(1 $\bar{1}$ 01) surface).

During MD simulations of Co surfaces and Co nanoclusters, it is likely that C and O atoms will undergo surface substitutions and sub-surface diffusion into interstitial sites. Table 6.3 shows ReaxFF fits to heats of formation for substitutional and interstitial configurations. Also shown are some C adatom adsorption energies on a Co surface with a C atom substitution. There is generally decent agreement, with most energy differences being less than 20 kJ/mol. Previous ReaxFF studies had an optimization goal of 4 kcal/mol (16.7 kJ/mol) as an acceptable energy difference.[155, 190] Many of the energy differences in Table 6.3 are close to this optimization goal.

Large-scale MD simulations of systems at high temperatures with mixed elements may produce alloy materials. These phases must be described by ReaxFF to ensure transferability of the potential. Table 6.4 shows the ReaxFF fit to VASP data for C substitutions of high density phases of Co (bcc and fcc). The size of the unit cells chosen for the configurations are small, leading to C dopant percentages ranging from 3 to 50%. The agreement for the

fcc phase is better than the bcc phase, which is desirable because fcc is a more stable phase of bulk Co.

Figure 6.1 shows equation of state curves for both the  $\text{Co}_2\text{C}$  and  $\text{CoO}$  binary crystal phases. The ReaxFF fits to both curves is acceptable, differing by less than 10 kJ/mol at points near equilibrium.  $\text{Co}_2\text{C}$  is the most stable carbide phase of Co.[191, 192] For cobalt oxides, the  $\text{CoO}$  and  $\text{Co}_3\text{O}_4$  crystal phases are the stable low temperature crystal phases. At high temperatures,  $\text{Co}_3\text{O}_4$  decomposes to  $\text{CoO}$ . [193] Unfortunately, the  $\text{Co}_3\text{O}_4$  phase is not described well by ReaxFF, which is discussed later in more detail.

### 6.3.2 Validation of force field

To validate the optimized Co/C/O force field parameters, we compare with additional DFT data that was not included in the training set. We also note that some of the Co/O and Co/C/O data in the training set were not included in the parameter optimization because it was problematic to provide worthwhile descriptions for all systems containing oxygen. To allow the optimization to include all of the training set calculations involving oxygen, it may be necessary to allow the O parameters to be adjusted. This would require many more DFT calculations on pure oxygen configurations, which is beyond the scope of this work. The parameter fitting was constrained to just the Co/C, Co/O, and Co/C/O parameters. As previously mentioned, the C, O, and Co parameters were not allowed to change during the parameter optimization.

Tables 6.5 and 6.6 show comparisons between additional VASP calculations and the predicted ReaxFF results for binary interactions (Co/C and Co/O). For both binary systems, we include adatom, adlayer, surface substitution, and interstitial configurations. Consistent with results from the training set fit, some configurations are described better than others. There is generally good agreement for adatoms and adlayers, while substitutions and interstitial configurations show larger predicted energy differences.

Just as the for the binary interactions, ReaxFF was used to predict DFT energies in a variety of tertiary configurations. Adsorption energies for adatoms on substituted surfaces are presented in Table 6.7. Without including these calculations in the parameter optimization,

ReaxFF over-predicts most the adsorption energies by an average of about 49 kJ/mol, which is about 3 times higher than the desirable optimization goal in previous work.[155, 190] We have also calculated adsorption of dissociated CO and 1 and 2 Co molecules on a variety of surfaces, shown in Table 6.8. There is general good predictive agreement for the tertiary adsorption energies.

### 6.3.3 Limitations of Co/C/O description

As with any semi-empirical potential, ReaxFF is not without limitations. The most noticeable is the lack of description for configurations that are dissimilar from those used in the parameter optimizations for which ReaxFF must interpolate and extrapolate from known configurations to calculate energies. This results in a poor descriptions for some systems. As mentioned before, an atomic species in one configuration (O in a condensed phase oxide) may behave very differently than in another configuration (O in a hydrocarbon molecule).

Table 6.9 shows examples of systems not well-described by the optimized Co/C/O ReaxFF parameters. Top-site adsorption energies on an hcp(0001) surface are more than 100 kJ/mol over-predicted for C, O, and CO configurations. For the cases of the C and O adatoms, this is not a large problem because these adatoms would likely adsorb in hollow adsorption sites. The CO molecule, however, should be stable in the top site. Surface substitutions of O atoms can also be poorly reproduced by ReaxFF optimized parameters. Likewise, C adatom adsorption energies on an O substituted surface are also largely over-predicted.

The equation of state for CoO presented in Figure 6.1 is described well by ReaxFF, but bulk phase atomic substitutions of O in bcc and fcc Co are not. Shown in Table 6.9, these configurations are simply not captured by the ReaxFF potential. One possible explanation for the lack of agreement may be the exclusion of much of training set configurations containing oxygen. A possible solution to this problem, as mentioned before, may be to allow the C, O, and Co parameters to be adjusted during a parameter optimization so that very accurate descriptions can be realized for all the investigated training set data.

Another source of error may be the manner in which the parameter optimization is performed. All ReaxFF and VASP energies are converted to heats of formation by subtracting the ground state energies for each of the atoms in a particular configuration. For Co, C, and O we use the bulk phase hcp, bulk graphite, and O<sub>2</sub> molecule as references, respectively. These were chosen because they are highly stable phases of each element. However, because we fit ReaxFF parameters to energy differences (e.g. heat of formation), absolute configurational energies are not equivalent. Hence, if we compare a different calculated quantity with a different way to reference a ground state, the agreement may be worse. The Co atoms in adsorption energies, for example, are referenced to the clean Co surface, not hcp Co.

In an effort to quantify the performance of the Co/C/O parameter optimization, Table 6.10 shows the average and standard deviations for different groupings of data. The averaged property is the energy difference between VASP and ReaxFF, given by  $|E_{\text{VASP}} - E_{\text{ReaxFF}}|$ , for all the adsorption and formation energy data found in previous tables. The data has been grouped into two pieces, data included in the optimization training set and data used to validate the Co/C/O parameters. Within these groupings, the averages and standard deviations were calculated for binary systems with Co and C only (Co/C) and systems involving O (Co/O, Co/C/O). It is evident that ReaxFF has consistent average energy differences and standard deviations in predicting results not included in the training set. The average error for all cases is just over 40 kJ/mol, which is just over two times the optimization goal of 16.7 kJ/mol used in the optimization of Co parameters.[190] The average energy difference from Table 6.9 is also presented. The poor agreement for these systems is taken in to consideration during the parameter fit. Each configuration is assigned a weighting factor during the optimization which essentially determines how much influence the configuration has on the overall optimization. Once it was determined these configurations would not be described well, their weighting factors were adjusted down such that their influence on the overall fit was small.

### 6.3.4 Cobalt-carbide segregation in nanoparticles

Carbide segregation is problematic in the tool and die industry because localized concentrations of carbon reduce the strength of the carbide material.[194] The optimized ReaxFF parameters are used to observe the effect of annealing in vacuum of a carbide nanocluster. Molecular dynamics simulations are performed on a 461 atom nanoparticle with a diameter of 20 Å. The nanoparticle is constructed from the Co<sub>2</sub>C phase, the stable carbide phase of Co. This nanoparticle is placed in vacuum and annealed at 1500 K for 300 ps.

At this temperature, it is observed that the Co<sub>2</sub>C phase nanoparticle segregates on a short time scale. Figure 6.2 shows the initial configuration and the configurations after 100, 200, and 300 ps. The progression of the C atoms during the MD simulation shows the migration from the bulk to the surface (image A to B), the formation of C chains on the surface image B to C), and finally the migration of C chains on the surface to conglomerate together, forming small graphene structures (image C to D). Simulation snapshots between 200 and 300 ps (image C to D) show the formation of 5 and 6 membered C ring structures, precursors for graphene production.

### 6.3.5 Oxidation of nanoclusters

It has been observed experimentally that Co nanocluster form hollow nanospheres in the presence of oxygen.[174] The phenomenon, analogous to the Kirkendall effect, states that the diffusion rate of bulk phase Co atoms through the oxide layer to the surface is greater than the diffusion rate of O atom into the nanoparticle. The mismatch in diffusion rates is balanced by the diffusion of vacancies into the nanoparticle. It has been shown in previous ReaxFF calculations that it is energetically favorable for vacancies to coalesce in the bulk.[190] Figure 6.3 shows a 500 ps ReaxFF simulation of fcc Co with 9 vacancies removed (~1%). ReaxFF predicts complete coalescence of the vacancies within 500 ps. Hence, vacancies contained within the boundary of the oxide layer of a Co nanocluster may have an affinity to coalesce in the center of the nanoparticle.

Oxidation using ReaxFF was performed on a ~20 Å diameter (461 atom) fcc Co nanoparticle at a temperature of 1500 K, higher than the 455 K temperature used in experiments.[174]

This higher temperature was used to increase kinetics in the simulation because the experimental observations are recorded in minutes. Figure 6.4 shows the final configuration of the nanoparticle after 300 ps. The surrounding O<sub>2</sub> fluid has been removed for image clarity. Unfortunately, ReaxFF predicts the formation of a solid oxide nanoparticle that is not hollow. However, the lack of agreement with experiments may not be a short-coming of the ReaxFF heterogeneous parameters. Several variables have been changed from the experimental conditions. As previously mentioned, the temperature has been increased to accelerate diffusion kinetics. We have also used an O<sub>2</sub> fluid concentration close to liquid conditions, effectively increasing the chemical potential. The O<sub>2</sub> source in the experiments bubbled through a colloidal suspension of Co nanoparticles. Finally, the nanoparticles used in experiments are on the order of 100 Å in diameter, not 20 Å. This corresponds to more than 15000 Co atoms, which is computationally very expensive. Perhaps there is minimum oxide layer thickness needed before the difference in counter-diffusion rates of O and Co is observable. Nanoparticles used in these simulations may not be large enough to form a thick oxide layer.

Ignoring O<sub>2</sub> molecules adsorbed on the surface, the ratio of Co to O atoms in the nanoparticle is approximately 1:1, consistent with the stoichiometry of the most stable oxide crystal phase, CoO. To explore the possibility of observing the formation of hollow oxide nanospheres, we look at diffusion barriers in the CoO crystal. Recall that CoO is cubic with a NaCl structure. Table 6.11 shows calculated diffusion energy barriers for two different mechanisms; vacancy-mediated and interstitial diffusion. For both O and Co, ReaxFF predicts that diffusion through the interstitial void space is more energetically favorable than vacancy-mediated diffusion. Assuming interstitial diffusion is the more likely to be observed, Co has a 38% lower energy barrier to diffuse through a cobalt oxide, which corresponds to a higher diffusion rate. This is consistent with experimental observations, as it is core Co atoms that diffuse more quickly through the oxide layer.

## 6.4 CONCLUSION

We have performed an extensive set of *ab initio* calculations used to develop parameters for a heterogeneous reactive force field. The optimized parameters have been shown to reproduce a variety of Co surface adsorption energies and heats of formation for configurations involving C and O within an average of about 40 kJ/mol. Validation calculations using the optimized parameters also reproduce various energies with the same average difference.

The optimized force field parameters were used to observe that a 461 atom (20 Å diameter) nanocluster of  $\text{Co}_2\text{C}$  will segregate in to a solid Co core with all of the C atoms on the surface. ReaxFF predicts this phenomenon will occur on short time scales. The C atoms on the surface form long C chains and some five- and six-membered rings, which are precursors of a larger graphene structure. Longer MD simulations are needed to observe the formation of a surface graphene structure. ReaxFF has also been used to validate the principles surrounding the formation of hollow nanospheres from oxidized Co nanoparticles. Predicted diffusion barriers of Co and O through a cobalt oxide crystal are consistent with the concept of the Kirkendall effect; ReaxFF predicts Co will diffuse through an oxide layer faster than oxygen. These binary applications demonstrate the transferability of transition metal descriptions of ReaxFF to heterogeneous systems.

Table 6.1: Adatom and adlayer adsorption energies (kJ/mol) for C and O. Adlayer energies are presented on a per atom basis. Calculated results for Reax are from the fit to the QM data. All adatoms occupy hollow adsorption sites.

Surface	System	VASP	Reax
bcc (011)	C	63.2	157.3
fcc (001)	C	6.0	59.7
fcc (011)	C	70.6	121.5
hcp (0001)	C	110.8	180.5
hcp (1 $\bar{1}$ 01)	C	182.8	250.6
bcc (011)	4 C	241.8	235.8
fcc (001)	4 C	134.6	182.7
fcc (011)	4 C	136.4	166.4
hcp (0001)	4 C	236.5	240.7
hcp (1 $\bar{1}$ 01)	4 C	147.9	179.7
bcc (011)	O	-249.0	-246.9
fcc (001)	O	-280.4	-261.7
fcc (011)	O	-228.6	-240.9
hcp (0001)	O	-249.1	-255.1
hcp (1 $\bar{1}$ 01)	O	-223.0	-177.4
bcc (011)	4 O	-83.6	-121.7
fcc (001)	4 O	-153.7	-166.5
fcc (011)	4 O	-178.5	-198.5
hcp (0001)	4 O	-155.8	-137.7
hcp (1 $\bar{1}$ 01)	4 O	-190.4	-215.9

Table 6.2: Reax fit to QM adsorption energies (kJ/mol) of dissociated CO and a CO molecule adsorbed on various Co surfaces. Adatoms and molecules occupy hollow (h) adsorption sites, with the exception of the hcp(0001) surface, which includes one bridge (b) site configuration.

Surface	System	VASP	Reax
bcc (011)	C+O (h-h)	-121.7	-51.8
fcc (001)	C+O (h-h)	-175.6	-117.7
fcc (011)	C+O (h-h)	-69.9	-28.4
hcp (0001)	C+O (h-h)	-46.3	-3.1
hcp (1 $\bar{1}$ 01)	C+O (h-h)	-35.5	-51.5
bcc (011)	CO (h)	-232.9	-263.1
fcc (001)	CO (h)	-217.3	-267.0
fcc (011)	CO (h)	-176.3	-240.4
hcp (0001)	CO (b)	-209.6	-238.8
hcp (0001)	CO (h)	-219.6	-250.5
hcp (1 $\bar{1}$ 01)	CO (h)	-196.6	-86.8

Table 6.3: Heats of formation (kJ/mol) of C and O surface substitutions and interstitial C and O atoms. Also shown are adsorption energies (kJ/mol) for adsorbing a C adatom on a surface with a single C atom substitution.

Surface	System	VASP	Reax
bcc (011)	C subs	951.9	949.9
fcc (001)	C subs	920.1	829.5
fcc (011)	C subs	1227.2	1191.8
hcp (0001)	C subs	761.5	748.5
hcp (1 $\bar{1}$ 01)	C subs	1277.4	1268.1
bcc (011)	C/CoC	184.2	177.0
fcc (001)	C/CoC	60.8	91.5
fcc (011)	C/CoC	19.8	27.2
hcp (0001)	C/CoC	-46.4	-123.4
hcp (1 $\bar{1}$ 01)	C/CoC	92.7	116.3
bcc (011)	C int	942.2	958.7
fcc (001)	C int	886.2	844.3
fcc (011)	C int	1244.7	1199.8
hcp (0001)	C int	673.6	720.6
bcc (011)	O int	748.1	728.2
fcc (001)	O int	793.8	640.0
fcc (011)	O int	872.8	788.6
hcp (0001)	O int	551.5	585.6

Table 6.4: Heats of formation (kJ/mol) for bulk fcc and bcc phases with C atom substitutions.

Supercell	System	VASP	Reax
bcc (1 × 1 × 1)	C	371.1	370.2
bcc (2 × 2 × 2)	C	397.5	481.5
bcc (2 × 2 × 2)	2 C	812.5	923.5
fcc (1 × 1 × 1)	C	410.0	381.0
fcc (2 × 2 × 2)	C	437.7	404.5
fcc (2 × 2 × 2)	2 C	813.8	801.3

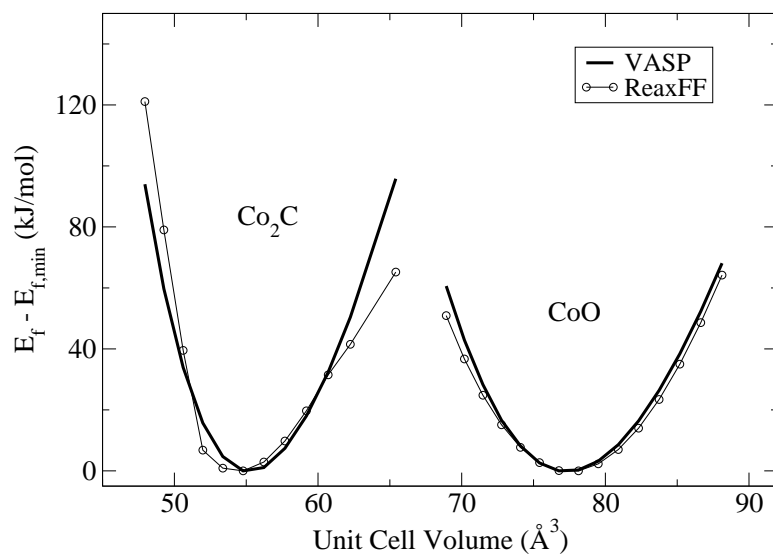


Figure 6.1: Comparison of the ReaxFF fit to equation of state curves for  $\text{Co}_2\text{C}$  (left) and  $\text{CoO}$  (right) crystal phases calculated from VASP.

Table 6.5: Reax predictions to various Co-C QM surface systems. Adatom and adlayer results are presented as adsorption energies (kJ/mol) while surface substitutions and interstitial C atom systems are heats of formation (kJ/mol). Adlayer results are presented on a per atom basis. (h) refers to adsorption of a surface hollow site. The fcc(111) surface has two distinct hollow sites, labelled (h1) and (h2).

Surface	System	VASP	Reax
bcc (001) adatom	C (h)	23.2	85.6
fcc (111) adatom	C (h1)	112.4	180.3
fcc (111) adatom	C (h2)	131.7	183.6
bcc (001) adlayer	4 C (h)	56.3	130.2
fcc (111) adlayer	4 C (h1)	234.5	240.7
fcc (111) adlayer	4 C (h2)	237.9	243.2
bcc (001) substitution	C	1173.8	1147.6
fcc (111) substitution	C	763.1	714.0
bcc (001) interstitial	C	1239.2	1189.9
fcc (111) interstitial	C	680.6	724.3

Table 6.6: Reax predictions to various Co-O QM surface systems. Descriptions of calculated systems are similar to those found in Table 6.5.

Surface	System	VASP	Reax
bcc (001) adatom	O (h)	-275.5	-265.5
fcc (111) adatom	O (h1)	-250.2	-255.1
fcc (111) adatom	O (h2)	-243.1	-255.5
bcc (001) adlayer	4 O (h)	-221.0	-207.2
fcc (111) adlayer	4 O (h1)	-159.3	-137.4
fcc (111) adlayer	4 O (h2)	-158.8	-137.3
fcc (111) substitution	O	406.8	462.1
fcc (111) interstitial	O	565.3	543.5
bcc (011) substitution	O	682.8	569.4
hcp (1 $\bar{1}$ 01) substitution	O	1033.2	913.3

Table 6.7: Predicted C and O adatom adsorption energies (kJ/mol) of substituted surfaces. All adatoms are adsorbed in hollow surface sites.

Surface	System	VASP	Reax
bcc (011)	C/CoO	256.9	322.6
fcc (011)	C/CoO	79.2	124.1
hcp (1 $\bar{1}$ 01)	C/CoO	96.9	162.3
bcc (001)	O/CoC	-259.2	-243.3
bcc (011)	O/CoC	-212.2	-156.3
fcc (001)	O/CoC	-302.8	-253.7
fcc (011)	O/CoC	-297.7	-316.2
hcp (1 $\bar{1}$ 01)	O/CoC	-274.9	-322.1
fcc (001)	O/CoO	-308.8	-223.4
fcc (011)	O/CoO	-318.7	-267.8
hcp (1 $\bar{1}$ 01)	O/CoO	-278.7	-269.8

Table 6.8: Predicted adsorption energies (kJ/mol) for 1 and 2 CO molecules as well as C and O adatoms. (h), (b), and (t) refer to hollow, bridge, and top adsorption sites, respectively.

Surface	System	VASP	Reax
bcc (001)	CO (h)	-207.1	-248.0
fcc (111)	CO (h1)	-219.6	-250.9
fcc (111)	CO (h2)	-217.4	-263.6
bcc (001) dissociated	C+O (h-h)	-167.6	-110.3
fcc (111) dissociated	C+O (h1-h1)	-50.4	-2.8
fcc (111) dissociated	C+O (h2-h2)	-28.8	0.3
bcc (011)	2 CO (h-h)	-209.6	-231.7
fcc (001)	2 CO (h-h)	-172.5	-209.6
fcc (011)	2 CO (h-h)	-129.9	-156.5
hcp (0001)	2 CO (h-b)	-219.4	-233.7
hcp (0001)	2 CO (h-t)	-204.0	-165.2
hcp (0001)	2 CO (b-b)	-196.6	-190.4
hcp (0001)	2 CO (b-t)	-202.3	-164.2
hcp (1 $\bar{1}$ 01)	2 CO (h-h)	-148.3	-159.4

Table 6.9: Comparison of fit results for (t) site adsorption energies and adatom adsorption energies on O substituted surfaces (kJ/mol). Also shown are predicted formation energies (kJ/mol) for O substitutions in bcc and fcc surface and bulk configurations.

Surface	System	VASP	Reax
hcp (0001)	C (t)	304.3	184.0
hcp (0001)	O (t)	-106.3	12.7
hcp (0001)	CO (t)	-214.2	-95.6
hcp (0001)	2 CO (t-t)	-164.1	-44.5
bcc (001) substitution	O	954.5	756.7
fcc (001) substitution	O	728.9	507.6
fcc (011) substitution	O	977.1	815.5
bcc (001)	C/CoO	-80.9	131.1
fcc (001)	C/CoO	-143.8	45.2
bcc (1 × 1 × 1)	O	-13.1	304.8
bcc (2 × 2 × 2)	O	178.1	226.7
bcc (2 × 2 × 2)	2 O	360.4	881.7
fcc (1 × 1 × 1)	O	135.6	410.5
fcc (2 × 2 × 2)	O	189.6	294.4
fcc (2 × 2 × 2)	2 O	312.9	655.3

Table 6.10: Measure of overall optimized fit and predictive results for the Co/C/O ReaxFF parameters taking the average difference between VASP and ReaxFF energies (Ave) and the standard deviation (SD) for a given data set. The results are split up into calculations involving only Co and C (Co/C) and those involving O (Co/O and Co/C/O). The corresponding tables used in the calculations are shown in parentheses. All averages and standard deviations have units of kJ/mol.

Results (Tables)	Carbon		Oxygen	
	Ave	SD	Ave	SD
Training Set (6.1,6.2, 6.3,6.4)	39.1	30.6	39.3	31.7
Predictions (6.5,6.6, 6.7,6.8)	43.6	23.9	44.1	32.9
Limitations (6.9)	—	—	200.9	120.8

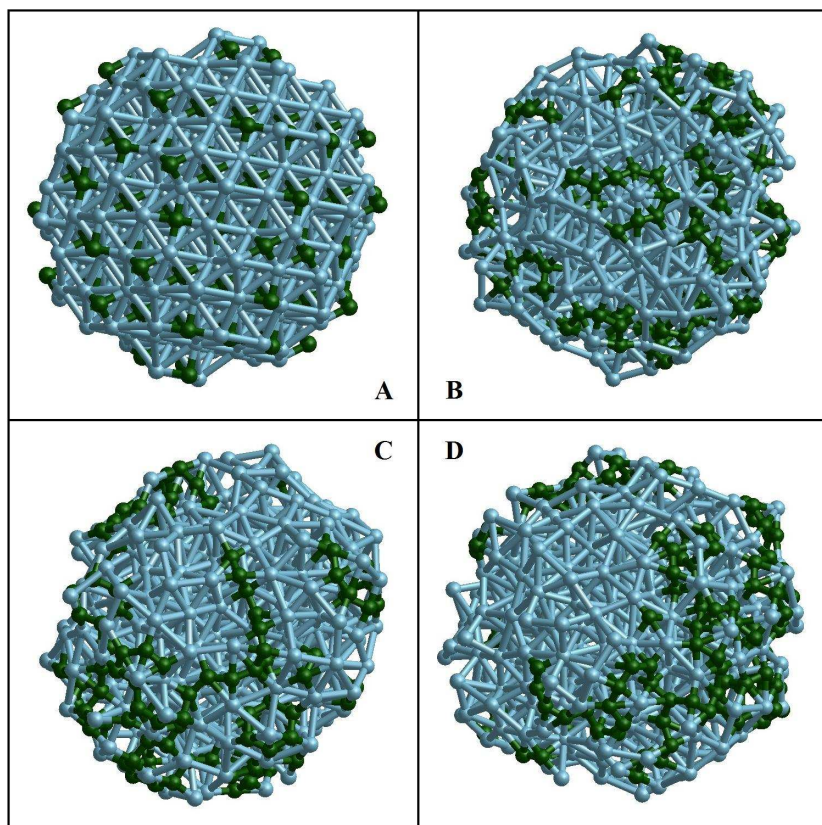


Figure 6.2: Molecular dynamics progression of a 461 atom  $\text{Co}_2\text{C}$  nanoparticle at 1500 K. The panels show nanoparticle configurations at (A) 0 ps, (B) 100 ps, (C) 200 ps, and (D) 300 ps. Co atoms are shown as light grey and O atoms are shown as dark gray.

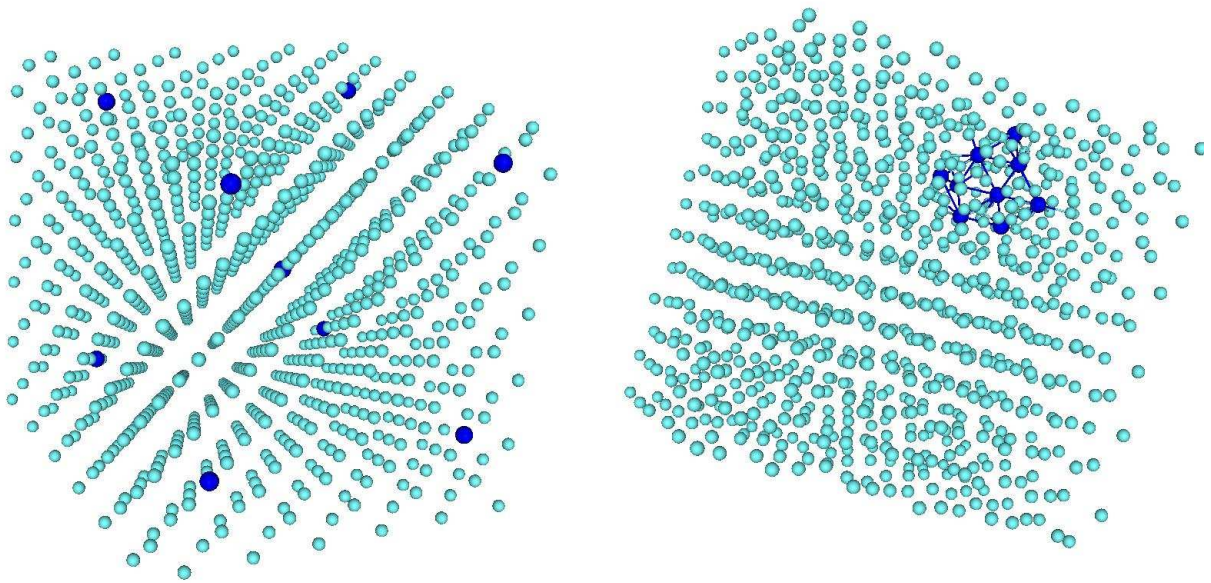


Figure 6.3: Molecular dynamics simulation of cobalt with  $\sim 1\%$  vacancies. The initial image and final image after 500 ps are shown on the left and right, respectively. The nine vacancies are represented as dark spheres.

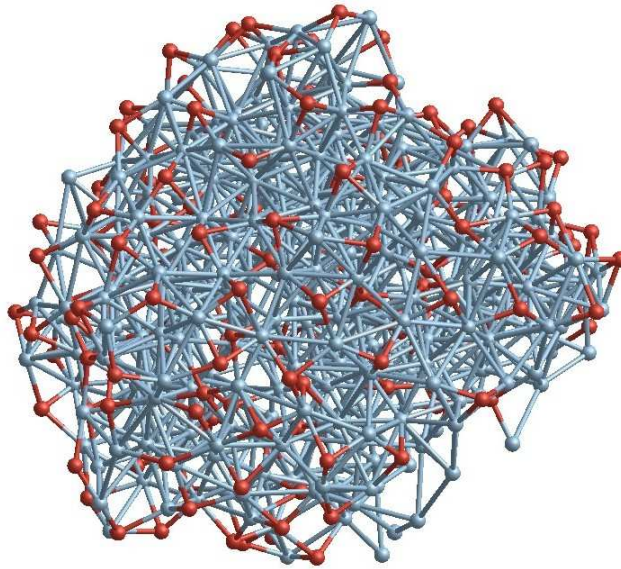


Figure 6.4: Final configuration of an oxidized 461 atom fcc Co nanoparticle at a temperature of 1500 K.

Table 6.11: Diffusion energy barriers (kJ/mol) for Co and O in bulk CoO using two different diffusion mechanisms.

Mechanism	$E_b$ (kJ/mol)
O-V swap	148.2
Co-V swap	157.2
O interstitial	86.6
Co interstitial	53.4

## 7.0 FUTURE WORK

As previously discussed, the ReaxFF Co/C/O is not without limitations. An important part of continued work in the field of ReaxFF is to identify sources of poorly described configurations in our heterogeneous system (e.g. CO top site adsorption). This could potentially provide useful feedback to Adri van Duin and the greater ReaxFF community of users. That said, an important next step in this field of work is to apply our heterogeneous reactive potential to systems of current interest in literature.

### 7.1 GRAIN BOUNDARIES AND TWINNING

Because ReaxFF is an empirical potential, it has the ability to handle simulations of hundreds or thousands of atoms. An area of interest to the condensed phase community is that of crystal grain boundaries and dislocation phenomena. Figure 7.1 displays a first attempt at a molecular dynamics simulation of reconstructing a twinned boundary at a temperature of 1000 K. The left image shows the initial configuration of two periodic fcc Co slabs placed in contact. The top slab is oriented in the [310] direction and the bottom slab is oriented in the [111] direction. From previous work, it was shown that the (111) surface formation energy (2.07 J/m<sup>2</sup>) is lower than that of the (310) surface (2.38 J/m<sup>2</sup>). Consistent with these results, the [111] phase promotes the [310] phase to reconstruct (right image). This event results in the top slab reconstructing to become hcp phase oriented in the [0001] direction, which is very similar to the fcc oriented in the [111] direction. ReaxFF predicts this occurs on a short time scale of 50 ps at this temperature.

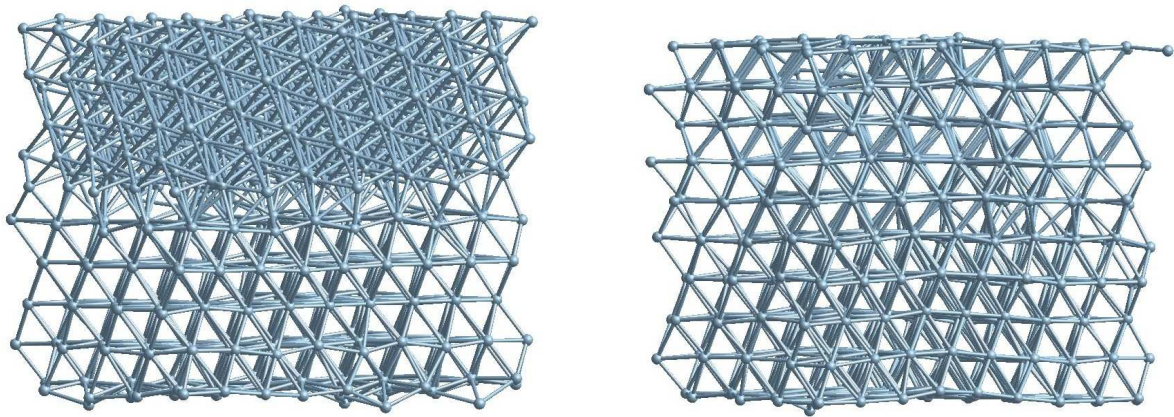


Figure 7.1: Molecular dynamics progression of a twinned structure at a temperature of 1000 K. The interfacial contacts are that of fcc(111) and fcc(310) surfaces.

Simulations studying grain boundaries requires thousands of atoms to accurately describe the local interfacial behavior. The simple twinned structure presented in Figure 7.1 contains 680 atoms and was able to run on a single processor in a reasonable amount of time. More complicated systems will likely contain more atoms and require more computation time. To accommodate these larger systems, software is needed that can run ReaxFF on a parallel processing platform. LAMMPS (large-scale atomic/molecular massively parallel simulator) is an open-source molecular dynamics code written by Steve Plimpton at Sandia National Laboratories.[178] Recently, LAMMPS software has been upgraded to include an implementation of the ReaxFF potential.

One beneficial feature of LAMMPS is the ability to apply shear stress to a system of atoms. This could very useful in studying gliding at grain boundaries. Using ReaxFF, one could determine a critical shear force required to induce gliding at an interface. This could be very useful to determine optimal grain orientations to resist gliding. In addition to gliding, a ReaxFF implementation in LAMMPS can be used to study recrystallization, perhaps identifying critical temperatures for seeded grain growth at variety of differently oriented interfaces.

## 7.2 SURFACE RECONSTRUCTION

Reconstruction of transition metal surfaces is important in understanding catalysis because of the surface adsorption sites that are created and destroyed during this process. Of particular interest is the reconstruction of chiral surfaces which have unique surface features that lack symmetry. Figure 7.2 shows the reconstruction of a fcc phase (986) surface at a temperature of 1000 K. Consistent with previous kinetic Monte Carlo simulations by Sholl et al.,<sup>[195]</sup> ReaxFF shows significant reconstruction of the surface and predicts step edge kinks will coalesce during reconstruction. Using the implementation within LAMMPS, ReaxFF could be used to predict critical temperatures for reconstruction of a variety of low-Miller index, high-Miller index, and chiral surfaces.

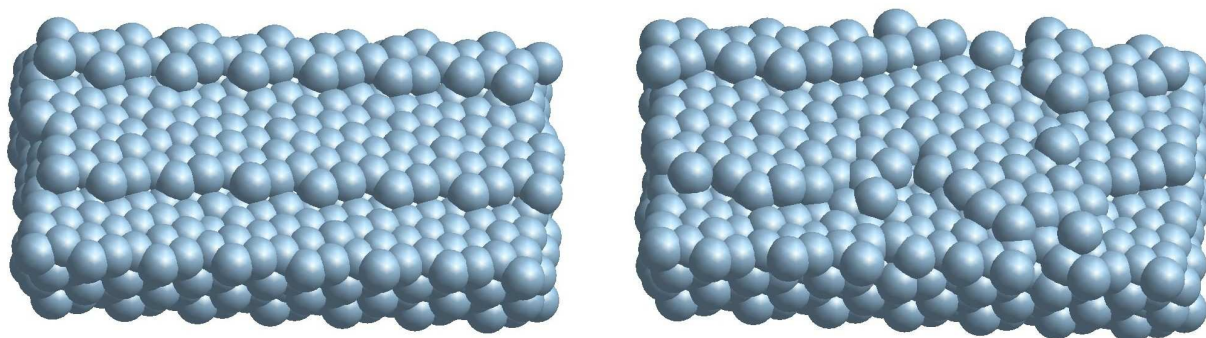


Figure 7.2: Molecular dynamics reconstruction of an fcc(986) chiral surface at 1000 K. The left and right images are taken at 0 and 100 ps, respectively.

## 7.3 CO DISSOCIATION ON CO NANOPARTICLES

Building on the surface reconstruction results, the heterogeneous Co/C/O ReaxFF potential could be used to investigate the adsorption mechanisms of CO gas molecules on various Co surfaces. To improve the design of the industrial catalysts, it is important to understand the nature of CO adsorption on Co surfaces. However, not all catalysis is done on surfaces.

Nanoparticles are used in a variety of industrial applications involving fluidized bed reactors because they offer attractive surface to volume ratios and provide many different types of surface adsorption sites. ReaxFF could be used to study the effect of nanoparticle size on surface reactions (e.g. CO dissociation), perhaps identifying an optimal size distribution to be used in industry.

## BIBLIOGRAPHY

- [1] A. Criscuoli, A. Basilea, E. Driolia, and O. Loiacono, *J. of Mem. Sci.* **181**, 21 (2001).
- [2] S. Adhikari and S. Fernando, *Ind. Eng. Chem. Res.* **45**, 875 (2006).
- [3] D. R. Simbeck, *Energy* **29**, 1633 (2004).
- [4] C. Liu, Y. Y. Fan, M. Liu, H. T. Cong, H. M. Cheng, and M. S. Dresselhaus, *Science* **286**, 1127 (1999).
- [5] A. C. Dillon, K. M. Jones, T. A. Bekkedahl, C. H. Kiang, D. S. Bethune, and M. J. Heben, *Nature* **386**, 377 (1997).
- [6] P. Chen, X. Wu, J. Lin, and K. L. Tan, *Science* **285**, 91 (1999).
- [7] Y. Ye, C. C. Ahn, C. Witham, B. Fultz, J. Liu, A. G. Rinzler, D. Colbert, K. A. Smith, and R. E. Smalley, *Appl. Phys. Lett.* **74**, 2307 (1999).
- [8] R. T. Yang, *Carbon* **38**, 623 (2000).
- [9] G. G. Tibbetts, G. P. Meisner, and C. H. Olk, *Carbon* **39**, 2291 (2001).
- [10] P. E. Pinkerton, B. G. Wicke, C. H. Olk, G. G. Tibbetts, G. P. Meisner, M. S. Meyer, and J. F. Herbst, *J. Phys. Chem. B* **104**, 9460 (2000).
- [11] M. Muris, N. Dufau, M. Bienfait, N. D. Pavlovsky, Y. Grillet, and J. P. Palmari, *Langmuir* **16**, 7019 (2000).
- [12] M. Muris, N. D. Pavlovsky, M. Bienfait, and P. Zeppenfeld, *Surf. Sci.* **492**, 67 (2001).
- [13] W. Teizer, R. B. Hallock, E. Dujardin, and T. W. Ebbesen, *Phys. Rev. Lett.* **82**, 5305 (1999).
- [14] W. Teizer, R. B. Hallock, E. Dujardin, and T. W. Ebbesen, *Phys. Rev. Lett.* **84**, 1844 (2000).
- [15] A. Kuznetsova, D. B. Mawhinney, V. Naumenko, J. T. Yates, Jr., J. Liu, and R. E. Smalley, *Chem. Phys. Lett.* **321**, 292 (2000).

- [16] S. E. Weber, S. Talapatra, C. Journet, A. Z. Zambano, and A. D. Migone, *Phys. Rev. B* **61**, 13150 (2000).
- [17] S. Talapatra, A. Z. Zambano, S. E. Weber, and A. D. Migone, *Phys. Rev. Lett.* **85**, 138 (2000).
- [18] S. Talapatra and A. D. Migone, *Phys. Rev. Lett.* **87**, 206106 (2001).
- [19] S. Talapatra and A. D. Migone, *Phys. Rev. B* **65**, 045416 (2002).
- [20] S. Talapatra, D. S. Rawat, and A. D. Migone, *J. Nanosci. Nanotechnol.* **2**, 467 (2002).
- [21] A. Fujiwara, K. Ishii, H. Suematsu, H. Kataura, Y. Maniwa, S. Suzuki, and Y. Achiba, *Chem. Phys. Lett.* **336**, 205 (2001).
- [22] A. Z. Zambano, S. Talapatra, and A. D. Migone, *Phys. Rev. B* **64**, 075415 (2001).
- [23] A. Zuttel, P. Sudan, P. Mauron, T. Kiyobayashi, C. Emmenegger, and L. Schlapbach, *Int. J. Hydrogen Energ.* **27**, 203 (2002).
- [24] T. Wilson, A. Tyburski, M. R. DePies, O. E. Vilches, D. Becquet, and M. Bienfait, *J. Low Temp. Phys.* **126**, 403 (2002).
- [25] D. H. Yoo, G. H. Rue, Y. H. Hwang, and H. K. Kim, *J. Phys. Chem. B* **106**, 3371 (2002).
- [26] D. H. Yoo, G. H. Rue, J. Y. Seo, Y. H. Hwang, M. H. W. Chan, and H. K. Kim, *J. Phys. Chem. B* **106**, 9000 (2002).
- [27] D. H. Yoo, G. H. Rue, M. H. W. Chan, Y. H. Hwang, and H. K. Kim, *J. Phys. Chem. B* **107**, 1540 (2003).
- [28] C. M. Yang, H. Kanoh, K. Kaneko, M. Yudasaka, and S. Iijima, *J. Phys. Chem. B* **106**, 8994 (2002).
- [29] H. Ulbricht, G. Moos, and T. Hertel, *Phys. Rev. B* **66**, 075404 (2002).
- [30] H. Ulbricht, J. Kriebel, G. Moos, and T. Hertel, *Chem. Phys. Lett.* **363**, 252 (2002).
- [31] M. R. Smith, Jr., E. W. Bittner, W. Shi, J. K. Johnson, and B. C. Bockrath, *J. Phys. Chem. B* **107**, 3752 (2003).
- [32] M. Bienfait, P. Zeppenfeld, N. Dupont-Pavlovsky, J. P. Palmari, M. R. Johnson, T. Wilson, M. DePies, and O. E. Vilches, *Phys. Rev. Lett.* **91**, 035503 (2003).
- [33] C. Matranga, L. Chen, B. Bockrath, and J. K. Johnson, *Phys. Rev. B* **70**, 165416 (2004).

- [34] M. Bienfait, P. Zeppenfeld, N. Dupont-Pavlovsky, M. Muris, M. R. Johnson, T. Wilson, M. DePies, and O. E. Vilches, *Phys. Rev. B* **70**, 035410 (2004).
- [35] V. Krungleviciute, L. Heroux, S. Talapatra, and A. D. Migone, *Nano Lett.* **4**, 1133 (2004).
- [36] G. Stan and M. W. Cole, *J. Low Temp. Phys.* **110**, 539 (1998).
- [37] Q. Y. Wang and J. K. Johnson, *J. Phys. Chem. B* **103**, 4809 (1999).
- [38] P. A. Gordon and R. B. Saeger, *Ind. Eng. Chem. Res.* **38**, 4647 (1999).
- [39] K. A. Williams and P. C. Eklund, *Chem. Phys. Lett.* **320**, 352 (2000).
- [40] F. Darkrim and D. Levesque, *J. Phys. Chem. B* **104**, 6773 (2000).
- [41] G. Stan, M. J. Bojan, S. Curtarolo, S. M. Gatica, and M. W. Cole, *Phys. Rev. B* **62**, 2173 (2000).
- [42] V. V. Simonyan, J. K. Johnson, A. Kuznetsova, and J. T. Yates, Jr., *J. Chem. Phys.* **114**, 4180 (2001).
- [43] M. M. Calbi, S. M. Gatica, M. J. Bojan, and M. W. Cole, *J. Chem. Phys.* **115**, 9975 (2001).
- [44] M. M. Calbi, F. Toigo, and M. W. Cole, *Phys. Rev. Lett.* **86**, 5062 (2001).
- [45] W. Shi and J. K. Johnson, *Phys. Rev. Lett.* **91**, 015504 (2003).
- [46] M. R. Johnson, S. Rols, P. Wass, M. Muris, M. Bienfait, P. Zeppenfeld, and N. Dupont-Pavlovsky, *Chem. Phys.* **293**, 217 (2003).
- [47] F. Ancilotto, M. M. Calbi, S. M. Gatica, and M. W. Cole, *Phys. Rev. B* **70**, 165422 (2004).
- [48] S. Agnihotri, J. P. B. Mota, M. Rostam-Abadi, and M. J. Rood, *Langmuir* **21**, 896 (2005).
- [49] S. Rols, R. Almairac, L. Henrard, E. Anglaret, and J. E. Sauvajol, *Eur. Phys. J. B* **10**, 263 (1999).
- [50] S. Bandow, S. Asaka, Y. Saito, A. M. Rao, L. Grigorian, E. Richter, and P. C. Eklund, *Phys. Rev. Lett.* **80**, 3779 (1998).
- [51] A. M. Rao, E. Richter, S. Bandow, B. Chase, P. C. Eklund, K. A. Williams, S. Fang, K. R. Subbaswamy, M. Menon, A. Thess, R. E. Smalley, G. Dresselhaus, and M. S. Dresselhaus, *Science* **275**, 187 (1997).

- [52] A. G. Rinzler, J. Liu, H. Dai, P. Nikolaev, C. B. Huffman, F. J. Rodríguez-Macías, P. J. Boul, A. H. Lu, D. Heymann, D. T. Colbert, R. S. Lee, J. E. Fischer, A. M. Rao, P. C. Eklund, and R. E. Smalley, *Appl. Phys. A* **67**, 29 (1998).
- [53] J. W. G. Wildoer, L. C. Venema, A. G. Rinzler, R. E. Smalley, and C. Dekker, *Nature* **391**, 59 (1998).
- [54] A. Thess, R. Lee, P. Nikolaev, H. Dai, P. Petit, J. Robert, C. Xu, Y. Lee, S. Kim, A. Rinzler, D. Colbert, G. Scuseria, D. Tomanek, J. Fischer, and R. Smalley, *Science* **273**, 483 (1996).
- [55] *Carbon Nanotubes Synthesis, Structure, Properties, and Applications*, edited by M. S. Dresselhaus, G. Dresselhaus, and P. Avouris (Springer-Verlag, Berlin, 2001).
- [56] M. J. Bronikowski, P. A. Willis, D. T. Colbert, K. A. Smith, and R. E. Smalley, *J. Vac. Sci. Technol., A* **19**, 1800 (2001).
- [57] C. Journet and P. Bernier, *Appl. Phys. A* **67**, 1 (1998).
- [58] W.-F. Du, L. Wilson, J. Ripmeester, R. Dutrisac, B. Simard, and S. Déommée, *Nano Lett.* **2**, 343 (2002).
- [59] C. Matranga and B. Bockrath, *J. Phys. Chem. B* **108**, 6170 (2004).
- [60] S. Kim, L. Chen, J. K. Johnson, and E. Marand, *J. Mem. Sci.* **294**, 147 (2007).
- [61] S. Agnihotri, Y. Zheng, J. P. B. Mota, I. Ivanov, and P. Kim, *J. Phys. Chem. C* **111**, 13747 (2007).
- [62] D. S. Rawat, L. Heroux, V. Krungleviciute, and A. D. Migone, *Langmuir* **22**, 234 (2006).
- [63] A. D. Migone and S. Talapatra, in *Encyclopedia of Nanoscience and Nanotechnology*, edited by H. S. Nalwa (American Scientific Publishers, Los Angeles, 2004), Vol. 3, pp. 749–767.
- [64] P. Kondratyuk, Y. Wang, J. K. Johnson, and J. T. Yates, Jr., *J. Phys. Chem. B* **109**, 20999 (2005).
- [65] O. Byl, J. Liu, and J. T. Yates, Jr., *Carbon* **44**, 2039 (2006).
- [66] M. M. Calbi, M. W. Cole, S. M. Gatica, M. J. Bojan, and G. Stan, *Rev. Mod. Phys.* **73**, 857 (2001).
- [67] S. Wu, *Prog. Theor. Phys.* **53**, 21 (1975).
- [68] K. Bolton and A. Rosén, *Phys. Chem. Chem. Phys.* **4**, 4481 (2002).
- [69] M. M. Calbi, F. Toigo, and M. W. Cole, *J. low Temp. Phys.* **126**, 179 (2002).

- [70] Y. Ye, C. C. Ahn, C. Witham, B. Fultz, J. Kiu, A. G. Rinzler, D. Colbert, K. A. Smith, and R. E. Smalley, *Appl. Phys. Lett.* **74**, 2307 (1999).
- [71] H. Chen, J. K. Johnson, and D. S. Sholl, *J. Phys. Chem. B* **110**, 1971 (2006).
- [72] T. J. H. Vlugt and M. Schenk, *J. Phys. Chem. B* **106**, 12757 (2002).
- [73] A. J. Fletcher, K. M. Thomas, and M. J. Sosseinsky, *J. Solid State Chem.* **178**, 2491 (2005).
- [74] D. J. Wales and J. P. K. Doye, *J. Phys. Chem. A* **101**, 5111 (1997).
- [75] D. J. Wales and H. A. Scheraga, *Science* **285**, 1368 (1999).
- [76] J. P. K. Doye and D. J. Wales, *Phys. Rev. Lett.* **80**, 1357 (1998).
- [77] A. H. Stroud and D. Seacrest, *Gaussian Quadrature Formulas* (Prentice Hall, New Jersey, 1966).
- [78] W. A. Steele, *The Interaction of Gases with Solid Surfaces* (Pergamon Press, Oxford, 1974).
- [79] J. E. Dennis, Jr., *Numerical Methods for Unconstrained optimization and Nonlinear Equations* (Prentice-Hall, New Jersey, 1983).
- [80] A. I. Skoulidas and D. S. Sholl, *J. Phys. Chem. B* **106**, 5058 (2002).
- [81] M. P. Allen and D. J. Tildesley, *Computer Simulation of Liquids* (Clarendon, Oxford, 1987).
- [82] A. D. Migone, (private communication).
- [83] L. W. Bruch, M. W. Cole, and E. Zaremba, *Physical Adsorption: Forces and Phenomena* (Oxford University Press, Oxford, 1997).
- [84] S. Ramachandran and O. E. Vilches, *Phys. Rev. B* **76**, 075404 (2007).
- [85] M. R. LaBrosse, W. Shi, and J. K. Johnson, *Langmuir* **24**, 9430 (2008).
- [86] X. Zhang, W. Wang, and G. Jiang, *Flu. Pha. Eq.* **218**, 239 (2004).
- [87] D. M. Ceperley, *Rev. Mod. Phys.* **67**, 279 (1995).
- [88] R. P. Feynman, *Rev. Mod. Phys.* **20**, 367 (1948).
- [89] Q. Y. Wang, J. K. Johnson, and J. Q. Broughton, *J. Chem. Phys.* **107**, 5108 (1997).
- [90] S. Duane, A. D. Kennedy, B. J. Pendleton, and D. Roweth, *Phys. Rev. B* **195**, 216 (1987).

- [91] M. E. Tuckerman, B. J. Berne, G. J. Martyna, and M. L. Klein, *J. Chem. Phys.* **99**, 2796 (1993).
- [92] C. R. Sweet, S. S. Hampton, R. D. Skeel, and J. A. Izaguirre, *J. Chem. Phys.* **131**, 174106 (2009).
- [93] R. P. Feynman and A. Hibbs, *Quantum Mechanics and Path-Integrals* (McGraw-Hill, New York, 1965).
- [94] H. Tanaka, J. Fan, H. Kanoh, M. Yudosaka, S. Iijima, and K. Kaneko, *Molec. Sim.* **31**, 465 (2005).
- [95] G. C. Maitland, M. Rigby, E. B. Smith, and W. A. Wakeham, *Intermolecular Forces* (Oxford, Clarendon, 1981).
- [96] L. W. Bruch, J. M. Phillips, and X.-Z. Ni, *Surf. Sci.* **136**, 361 (1984).
- [97] W. A. Steele, *Surf. Sci.* **36**, 317 (1973).
- [98] F. Hanono, C. E. N. Gatts, and E. Lerner, *J. Low Temp. Phys.* **60**, 73 (1985).
- [99] V. Krungleviciute and A. D. Migone, 2009, private communications.
- [100] H. Y. Kim, A. D. Lueking, S. M. Gatica, J. K. Johnson, and M. W. Cole, *Molec. Phys.* **106**, 1579 (2008).
- [101] J. Sato, T. Omori, K. Oikawa, I. Ohnuma, R. Kainuma, and K. Ishida, *Science* **312**, 90 (2006).
- [102] R. Roy, D. Agrawal, J. Cheng, and S. Gedevanishvili, *Nature* **399**, 668 (1999).
- [103] J. P. Cheng, D. K. Agrawal, S. Komarneni, M. Mathis, and R. Roy, *Materials Research Innovations* **1**, 44 (1997).
- [104] D. K. Agrawal, *Current Opinion in Solid State and Materials Science* **3**, 480 (1998).
- [105] E. Breval, J. P. Cheng, D. K. Agrawal, P. Gigl, M. Dennis, R. Roy, and A. J. Papworth, *Mat. Sci. Eng. A* **391**, 285 (2005).
- [106] X. Y. Liu, W. Windl, K. M. Beardmore, and M. P. Masquelier, *App. Phys. Lett* **82**, 1839 (2003).
- [107] H. Raebiger, M. Ganchenkova, and J. V. Boehm, *App. Phys. Lett.* **89**, 012505 (2006).
- [108] A. Satta, F. Willaime, and S. de Gironcoli, *Phys. Rev. B* **57**, 11184 (1998).
- [109] P. Ramanarayanan, K. Cho, and B. Clemens, *J. App. Phys.* **94**, 174 (2003).
- [110] M. Fähnle, J. Mayer, and B. Meyer, *Intermetallics* **7**, 315 (1999).

- [111] A. Choneos, H. Bracht, R. W. Grimes, and B. P. Uberuaga, *App. Phys. Lett.* **92**, 172103 (2008).
- [112] C. Janke, R. Jones, S. Öberg, and P. R. Briddon, *Phys. Rev. B* **77**, 075208 (2008).
- [113] M. Mantina, Y. Wang, R. Arroyave, L. Q. Chen, Z. K. Liu, and C. Wolverton, *Phys. Rev. Lett.* **100**, 215901 (2008).
- [114] J. P. Perdew, K. Burke, and M. Ernzerhof, *Phys. Rev. Lett.* **77**, 3865 (1996).
- [115] G. Kresse and J. Hafner, *Phys. Rev. B* **47**, 558 (1993).
- [116] G. Kresse and J. Hafner, *Phys. Rev. B* **49**, 14251 (1994).
- [117] G. Kresse and J. Furthmüller, *Comput. Matter. Sci.* **6**, 15 (1996).
- [118] G. Kresse and J. Furthmüller, *Phys. Rev. B* **54**, 11169 (1996).
- [119] D. Vanderbilt, *Phys. Rev. B* **41**, 7892 (1990).
- [120] K. Laasonen, R. Car, C. Lee, and D. Vanderbilt, *Phys. Rev. B* **43**, 6796 (1991).
- [121] K. Laasonen, A. Pasquarello, R. Car, C. Lee, and D. Vanderbilt, *Phys. Rev. B* **47**, 10142 (1993).
- [122] H. J. Monkhorst and J. D. Pack, *Phys. Rev. B* **13**, 5188 (1976).
- [123] A. Taylor, *J. Inst. Metals* **77**, 585 (1950).
- [124] C. Kittel, *Introduction to Solid State Physics*, fourth ed. (Wiley, New York, 1971).
- [125] G. Mills, H. Jónsson, and G. K. Schenter, *Surf. Sci.* **324**, 305 (1995).
- [126] H. Jónsson, G. Mills, and K. W. Jacobsen, in *Classical and Quantum Dynamics in Condensed Phase Simulations*, edited by B. J. Berne, G. Ciccotti, and D. F. Coker (World Scientific, Singapore; River Edge, NJ, 1998).
- [127] K. Carling, G. Wahnström, T. R. Mattsson, A. E. Mattsson, N. Sandberg, and G. Grimvall, *Phys. Rev. Lett.* **85**, 3862 (2000).
- [128] A. E. Mattsson and W. Kohn, *J. Chem. Phys.* **115**, 3441 (2001).
- [129] T. R. Mattsson and A. E. Mattsson, *Phys. Rev. B* **66**, 214110 (2002).
- [130] A. E. Mattsson, R. Armiento, P. A. Schultz, and T. R. Mattsson, *Phys. Rev. B* **73**, 195123 (2006).
- [131] See the surface intrinsic error calculator at <http://dft.sandia.gov/functionals/webcalculator.html>.
- [132] A. E. Mattsson, R. R. Wixom, and R. Armiento, *Phys. Rev. B* **77**, 155211 (2008).

- [133] P. Hohenberg and W. Kohn, *Phys. Rev.* **136**, B864 (1964).
- [134] H. Matter, J. Winter, and W. Triftshäuser, *App. Phys.* **20**, 135 (1979).
- [135] L. de Schepper, D. Segers, G. Knuyt, L. Dorikens-Vanpraet, M. Dorikens, L. Stals, and P. Moser, *Phys. Lett. A* **95**, 121 (1983).
- [136] J. Wolff, M. Franz, J. E. Kluin, and D. Schmid, *Acta Mater.* **45**, 4759 (1997).
- [137] E. G. Moroni, G. Kresse, J. Hafner, and J. Furthmüller, *Phys. Rev. B* **56**, 15629 (1997).
- [138] G. Kresse and D. Joubert, *Phys. Rev. B* **59**, 1758 (1999).
- [139] Y. Yin, R. M. Rioux, C. K. Erdonmez, S. Hughes, G. A. Somorjai, and A. P. Alivisatos, *Science* **304**, 711 (2004).
- [140] P. E. Blöchl, *Phys. Rev. B* **50**, 17953 (1994).
- [141] A. Rockett, D. D. Johnson, S. V. Khare, and B. R. Tuttle, *Phys. Rev. B* **68**, 233208 (2003).
- [142] M. E. Glicksman, *Diffusion in Solids* (Wiley, New York, 2000).
- [143] J. J. Burton, *Phys. Rev. B.* **5**, 2948 (1972).
- [144] F. El-Mellouhi, N. Mousseau, and P. Ordejón, *Phys. Rev. B.* **70**, 205202 (2004).
- [145] K. H. Kraatz, G. Froberg, and H. Wever, *Phys. Stat. Sol. A* **52**, 149 (1979).
- [146] W. Bussmann, C. Herzig, W. Rempp, K. Maier, and H. Mehrer, *Phys. Stat. Sol. A* **56**, 87 (1979).
- [147] N. Sandberg, B. Magyari-Köpe, and T. R. Mattsson, *Phys. Rev. Lett.* **89**, 065901 (2002).
- [148] J. Ružičková, B. Million, and J. Kučera, *Kovové Materiály* **19**, 3 (1981).
- [149] F. C. Nix and F. E. J. Jr., *Phys. Rev.* **82**, 72 (1951).
- [150] S. Haglund and J. Ågren, *Acta Mater.* **46**, 2801 (1998).
- [151] V. N. Mackiw and T. W. Benz, in *Extractive Metallurgy of Copper, Nickel, and Cobalt*, edited by P. Queneua (Wiley-Interscience, New York, 1961), pp. 503–534.
- [152] F. T. Manheim, *Science* **232**, 600 (1986).
- [153] G. Nemethy, M. S. Pottle, and H. A. Scheraga, *J. Phys. Chem.* **87**, 1883 (1983).
- [154] M. J. Sippl, G. Nemethy, and H. A. Scheraga, *J. Phys. Chem.* **88**, 6231 (1984).

- [155] A. C. T. van Duin, S. Dasgupta, F. Lorant, and W. A. G. III, *J. Phys. Chem. A* **105**, 9396 (2001).
- [156] S. Cheung, W. Q. Deng, A. C. T. van Duin, and W. A. Goddard III, *J. Phys. Chem. A* **109**, 851 (2005).
- [157] S. S. Han, J. K. Kang, H. M. Lee, A. C. T. van Duin, and W. A. Goddard III, *J. Chem. Phys.* **123**, 114703 (2005).
- [158] S. S. Han, A. C. T. van Duin, W. A. Goddard III, and H. M. Lee, *J. Phys. Chem. A* **109**, 4575 (2005).
- [159] K. D. Nielson, A. C. T. van Duin, J. Oxgaard, W. Deng, and W. A. G. III, *J. Phys. Chem. A* **109**, 493 (2005).
- [160] M. J. Buehler, A. C. T. van Duin, and W. A. Goddard III, *Phys. Rev. Lett.* **96**, 095505 (2006).
- [161] J. Ludwig, D. G. Vlachos, A. C. T. van Duin, and W. A. Goddard III, *J. Phys. Chem. B* **110**, 4274 (2006).
- [162] J. G. O. Ojwang, R. van Santen, G. J. Kramer, A. C. T. van Duin, and W. A. Goddard III, *J. Chem. Phys.* **129**, 244506 (2008).
- [163] T. T. Järvi, A. Kuronen, M. Hakala, K. Nordlund, A. C. T. van Duin, W. A. Goddard III, and T. Jacob, *Eur. Phys. J. B* **66**, 75 (2008).
- [164] A. C. T. van Duin, J. M. A. Baas, and B. van de Graaf, *Journal of the Chemical Society, Faraday Transactions* **90**, 2881 (1994).
- [165] Y. Wang and J. P. Perdew, *Phys. Rev. B* **45**, 13244 (1992).
- [166] J. Giber, R. Drube, and V. Dose, *App. Phys. A: Mat. Sci. and Proc.* **52**, 167 (1991).
- [167] C. Kittel, *Introduction to Solid State Physics* (John Wiley and Sons Inc., New Jersey, 2004).
- [168] J. Gump, H. Xia, M. Chirita, R. Sooryakumar, M. A. Tomaz, and G. R. Harp, *Journal of Applied Physics* **86**, 6005 (1999).
- [169] J. Tersoff, *Phys. Rev. B* **37**, 6991 (1988).
- [170] H. J. C. Berendsen, J. P. M. Postma, W. F. van Gunsteren, A. DiNola, and J. R. Haak, *J. Chem. Phys.* **81**, 3684 (1984).
- [171] F. Murnaghan, *Proc. of the Nat. Acad. of Sci.* **30**, 244 (1944).

- [172] M. J. Mehl, B. M. Klein, and D. A. Papaconstantopoulos, in *Intermetallic Compounds: Principles and Practice*, edited by J. H. Westbrook and R. L. Fleischer (John Wiley and Sons, London, 1995), pp. 195–210.
- [173] M. R. LaBrosse, L. Chen, and J. K. Johnson, *Mod. Sim. Mater. Sci. Eng.* (2009), submitted.
- [174] Y. Yin, R. M. Rioux, C. K. Erdonmez, S. Hughes, G. A. Somorjai, and A. P. Alivisatos, *Science* **304**, 711 (2004).
- [175] U. Bardi, P. Tiscione, and G. Rovida, *App. Surf. Sci.* **27**, 299 (1986).
- [176] S. Pick, *Surf. Sci.* **601**, 5571 (2007).
- [177] R. Pasianot and E. J. Savino, *Phys. Rev. B* **45**, 12704 (1992).
- [178] S. J. Plimpton, *J. Comp. Phys.* **117**, 1 (1995).
- [179] S. N. Luo, A. Strachan, and D. C. Swift, *J. Chem. Phys.* **120**, 11640 (2004).
- [180] L. Zheng, S. N. Luo, and D. L. Thompson, *J. Chem. Phys.* **124**, 154504 (2006).
- [181] I. Yokoyama, *Physica B* **271**, 230 (1999).
- [182] I. Yokoyama and T. Arai, *J. Non-Cryst. Sol.* **293**, 806 (2001).
- [183] X. J. Han, N. Wang, and B. Wei, *Philosophical Magazine Letters* **82**, 451 (2002).
- [184] D. L. Tönsing, P. M. Stoop, and J. H. van der Merwe, *Surf. Sci.* **277**, 193 (1992).
- [185] F. Soisson, A. Barbu, and G. Martin, *Acta Mater.* **44**, 3789 (1996).
- [186] K. Chenoweth, A. C. T. van Duin, P. Persson, M.-J. C. J. Oxgaard, and W. A. Goddard III, *J. Phys. Chem. C* **112**, 14645 (2008).
- [187] D. Raymond, A. C. T. van Duin, M. Baudin, and K. Hermansson, *Surf. Sci.* **602**, 1020 (2008).
- [188] D. W. Brenner, *Phys. Rev. B* **42**, 9458 (1990).
- [189] F. Cleri and V. Rosato, *Phys. Rev. B* **48**, 22 (1993).
- [190] M. R. LaBrosse, J. K. Johnson, and A. C. T. van Duin, *J. Chem. Theo. Comp.* (2009), submitted.
- [191] J. Clarke and K. H. Jack, *Chem. and Ind.* **46**, 1004 (1951).
- [192] S. Nagakura, *Soc. Japan* **16**, 1213 (1961).

- [193] N. Greenwood and A. Earnshaw, *Chemistry of the Elements (2nd ed.)* (Butterworth-Heinemann, Oxford, 1997).
- [194] A. M. Parshin and N. B. Kirillov, *Metal Sci. Heat Treat.* **29**, 889 (1987).
- [195] D. S. Sholl, A. Asthagiri, and T. D. Power, *J. Phys. Chem. B* **105**, 4771 (2001).